Wind and wave-induced currents over sloping bottom topography, with application to the Caspian Sea

Thesis for the degree of Philosophiae Doctor

Peygham Ghaffari
Faculty of Mathematics and Natural Sciences
University of Oslo
Norway

March 11, 2014

Series of dissertations submitted to the
Faculty of Mathematics and Natural Sciences, University of Oslo
No. 1470

ISSN 1501-7710

Cover: Inger Sandved Anfinsen.
Printed in Norway: AIT Oslo AS.

Produced in co-operation with Akademika Publishing.
The thesis is produced by Akademika Publishing merely in connection with the thesis defence. Kindly direct all inquiries regarding the thesis to the copyright holder or the unit which grants the doctorate.

Acknowledgement

Firstly, I am very grateful to my principal supervisor, Prof. Jan Erik H. Weber. Jan has always provided support, guidance and enthusiasm for this PhD. I appreciate his patience discussing, proof-reading and (most of all) for always looking for theoretical explanations. Thanks for being always helpful and supportive not only about scientific issues, but also with personal matters. Secondly, I would like to thank my second supervisor Prof. Joseph H. LaCasce, as well as Dr. Pål Erik Isachsen, for their valuable contributions. Many thanks to all friends and colleagues at the MetOs section for a great working environment. I wish to thank the Norwegian Quota Scheme for partial financial support during these years.

And last but not least, I would like to thank my family Mahnaz and Marina for their patience and being always supportive.

January, 2014

List of publications

The present thesis is entitled "Wind and wave-induced currents over sloping bottom topography, with application to the Caspian Sea", and is based on the following papers:

I- Ghaffari, P., Isachsen, P. E., and LaCasce, J. H.: 2013, Topographic effects on current variability in the Caspian Sea, *J. Geophys. Res.,* 118, pp 1-10.

II- Weber, J. E. H. and Ghaffari, P.: 2009, Mass transport in the Stokes edge wave, *J. Mar. Res.,* 67, 213-224.

II- Ghaffari, P. and Weber, J. E. H.: 2014, Mass transport in the Stokes edge wave for constant arbitrary bottom slope in a rotating ocean, *J. Phys. Oceanogr.,* doi:10.1175/JPO-D-13-0171.1, in press.

IV- Weber, J. E. H. and Ghaffari, P.: 2014, Mass transport in internal coastal Kelvin waves, *Europ. J. Mech. B/Fluids*, in press.

Contents

Chapter 1

Introduction

In the ocean basins topography and coasts may act to trap mechanical energy. This energy may be in the form of wind-driven currents along bottom contours or gravity waves along coasts or sloping beaches. Since waves do posses mean momentum when averaged over the wave cycle, i.e. the Stokes drift (*Stokes*, 1847), they induce a net transport of water particles in the same way as the more traditional wind-driven currents. Since these currents are trapped in regions close to the coast, or over bottom slopes in the coastal region, they may directly affect human activity and the coastal population through their ability to transport biological material, pollutants and sediments in suspension along the shore.

1.1 Thesis objectives

The first objective of the work presented in this thesis is to provide better understanding of the topographic effect on current variability. This is done by exploring specific topics where the effect of topography may alter the currents. In wind-induced current case, the dynamics of flows with closed potential vorticity (PV) contours is examined. Topography generally distorts the geostrophic currents. If the topography is steep enough, it dominates the stationary part of the potential vorticity, even causing closed PV contours. Therefore, mean flow can be excited and exist on the closed contours (without encountering with boundaries) by wind-forcing. At ocean depths that are intersected by topography, currents steer around major topographic features. In addition, particularly at high latitudes, where the ocean is weakly stratified (*Isachsen et al.*, 2003), geophysical flows tend to be vertically coherent (or barotropic) due to the rotation of the Earth. As a result currents near the ocean surface align in roughly the same direction as deep ocean currents, and consequently often follow contours of constant depth, e.g. see (*Gille et al.*, 2004). Most major currents respond to sea floor topography. In the present study, we investigated to what degree this mechanism works for the Caspian Sea which is a low latitude water body.

The second objective is to estimate the mean currents induced by trapped gravity waves. For that purpose, we investigated the Lagrangian mass transport in two different types of the gravity waves; the Stokes edge waves over sloping topography in a non-rotating and rotating ocean, and the internal coastal Kelvin wave. In practice, these waves are trapped due to a sloping bottom and the earth's rotation. In particular, the Lagrangian mass transport is obtained from the ver-

tically integrated equation of momentum and mass, correct to second order in wave steepness. The Lagrangian current is composed of a non-linear Stokes drift (inherent in the waves) and a mean vertically-averaged Eulerian current. When waves propagate along topography (along the coast), the effect of viscosity leads to a wave attenuation, and hence a radiation stress component. The Eulerian current arises as a balance between the radiation stress, bottom friction, and the Coriolis force in a rotating ocean. The associated Stokes drift and Eulerian currents are investigated for the aforementioned waves. Additionally, their contributions to the mean Lagrangian drift are examined. We wish to explore how the contributions of the Stokes drift and Eulerian current varies with factors such as slope angle, wave amplitude, wave length and the earth's rotation.

In order to address these objectives four papers are included in this thesis. Objective number 1 is treated in paper I (*Ghaffari et al.*, 2013), objective number 2 in papers II (*Weber and Ghaffari*, 2009), III (*Ghaffari and Weber*, 2014), and IV (*Weber and Ghaffari*, 2014).

The remaining part of this thesis is organized as follows: chapter 2 presents a brief theory, and chapter 3 provides a description of the study area. Results are presented and discussed in chapter 4. This is then followed by prints of the papers.

Chapter 2

Theory

This section provides a short theoretical background of the wind-induced current variability on closed PV contours. Additionally, some theory and explanation of the concept of wave-induced currents, i.e. Stokes drift and Eulerian current are given. The section also presents a brief overview of the Stokes edge wave, the internal coastal Kelvin wave, and the associated wave-induced drifts.

2.1 On current variability over closed PV contours

2.1.1 Barotropic model

Most major currents respond to sea floor topography. For instance, topography seems to steer the Antarctic Circumpolar Current (ACC) on certain part of its path (*Gordon et al.*, 1978). Also Gulf Stream and the Kuroshio Extension all steer around ridges and seamounts. It is the conservation of potential vorticity which confines a water parcel to the PV contours. Hence, the conservation equation for PV provides an equally powerful and simple tool for discussion of the mean oceanic circulation on climatic scales (time scale of several months, length scale of about 500 km (*Hasselmann*, 1982)). In fact, strong topography may dominate the stationary part of the PV, even causing closed PV contours. The dynamics of the closed PV contours is different from those with blocked contours. With closed contours it is possible to obtain steady flows parallel to the PV contours. Such mean flow, which is not present with blocked contours, can be excited by wind forcing (*Hasselmann*, 1982; *Kamenkovich*, 1962; *Greenspan*, 1990). The mass transport, the depth integrated horizontal velocity, can be modeled using an integral equation derived from shallow water equation. In the linear limit, the model assumes a balance between divergence in the surface Ekman layer and convergence in the bottom Ekman layer; the latter is achieved via a flow parallel to the PV contours (Fig. 2.1). The flow strength can be predicted, if one knows the wind stress and topography.

The theory is described by *Isachsen et al.* (2003). Consider a homogeneous ocean with a rigid lid and varying topography. Ignoring non-linearity and exploiting the Boussinesq approximation, the depth-integrated, horizontal momentum equation takes the form

$$\frac{\partial \vec{u}}{\partial t} + fk \times \vec{u} = -g\nabla\eta + \frac{1}{H}\left(\frac{\vec{\tau}_s}{\rho_0} - \vec{\tau}_b\right), \tag{2.1}$$

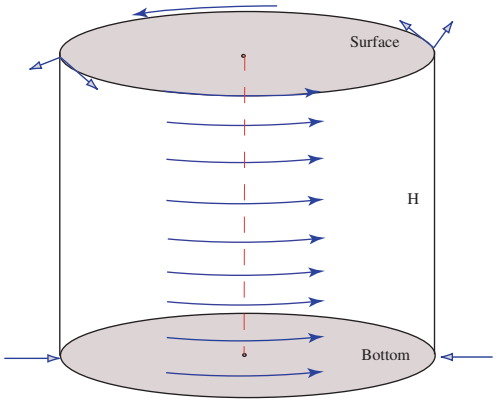

Figure 2.1: Schematic of barotropic model spin-up.

where u is horizontal velocity vector, f is the Coriolis parameter, η is the sea surface displacement, τ_s is the wind stress and τ_b is the bottom stress. Note that horizontal (eddy) diffusion of momentum is excluded. Taking the curl yields

$$\frac{\partial}{\partial t}\nabla \times \vec{u} + J(\psi, \frac{f}{H}) = k \cdot \nabla \times \left(\frac{\vec{\tau}_s}{\rho_0 H} - \frac{\vec{\tau}_b}{H} \right), \tag{2.2}$$

where J is the Jacobian operator and ψ is the transport stream function

$$\int_{-H}^{0} (u, v)\, dz = (-\psi_x, \psi_y)\,. \tag{2.3}$$

The dominant term in (2.2) is the second one and that the temporal variability, wind forcing and bottom drag are comparably small. This implies that the first-order flow is parallel to the f/H contours. Therefore, to the extent that oceanographic flows are barotropic, they should be steered along f/H contours. Assuming a linear bottom drag in line with Ekman damping, so that $\tau_b = R\vec{u}$ (R is the bottom friction coefficient), and integrating (2.2) over an area bounded by an f/H contour yields

$$\frac{\partial}{\partial t} \oint_{f/H} \vec{u} \cdot dl = \frac{1}{\rho_0 H} \oint_{f/H} \tau_s \cdot dl - \frac{R}{H} \oint_{f/H} \vec{u} \cdot dl, \tag{2.4}$$

after applying Stokes' theorem. The fist term on the right hand side is the net Ekman transport in or out of the surface layer and the last term is the net transport in the bottom layer. An imbalance between them determines a circulation pattern around the closed contour. In order to get better impression about the response of the flow to forcing, it is convenient to take a Fourier transform in time, which gives

$$\vec{U}_0 = \left(\frac{k}{H} \times \nabla \frac{f}{H} \right) \mathrm{Re} \left[\frac{\oint_{f/H} \rho_0^{-1} H^{-1} \vec{\tau}_s \cdot dl}{\oint_{f/H} H^{-1} (r + i\omega) \left(\nabla \frac{f}{H} \cdot \vec{n} \right) dl} \right], \tag{2.5}$$

where $r = R/H$ is an inverse frictional damping time scale and n is the surface normal unit vector. Therefore, the surface circulation depends on the bottom friction and the forcing frequency. Additionally, the model can be used to study Sea Surface Hight (SSH) variabilities by determining the difference in Sea Level Anomalies (SLA) between different f/H contours

$$\frac{\partial \eta_0}{\partial (f/H)} = \left(\frac{f}{g}\right) \mathrm{Re}\left[\frac{\oint_{f/H} \rho_0^{-1} H^{-1} \vec{\tau}_s \cdot dl}{\oint_{f/H} H^{-1} (r + i\omega) \left(\nabla \frac{f}{H} \cdot \vec{n}\right) dl}\right]. \tag{2.6}$$

The velocities resulting from the barotropic model are parallel to the PV contours, and SSH displacements and the geostrophic velocities are inversely proportional to the bottom friction coefficient. For example, assume the wind stress has a single frequency, $\vec{\tau} = \vec{\tau}_0 \cos(\omega t)$. The velocity is then

$$\oint_{f/H} \vec{u} \cdot dl = \frac{\vec{\tau}_0}{r^2 + \omega^2} \left[r \cos(\omega t) + \omega \sin(\omega t)\right] \tag{2.7}$$

From this it is evident that

$$\oint_{f/H} \vec{u} \cdot dl \sim \frac{\vec{\tau}_0}{\omega} \sin(\omega t), \quad r \leq \omega, \qquad \oint_{f/H} \vec{u} \cdot dl \sim \frac{\vec{\tau}_0}{r} \cos(\omega t), \quad r \geq \omega.$$

At frequency much lower than r, the response is in phase with the wind and inversely proportional to r. At high frequencies, the amplitude is independent of r and the response lags the wind by $\pi/2$. Barotropic theory is often supported by observations. For example, floats in the Atlantic and Pacific Oceans preferentially spread along f/H contours rather than across them, indicating that flow responds to topography (LaCasce, 2000).

2.1.2 Equivalent Barotropic model

In practice, since the ocean is stratified, and velocities tend to be faster near the ocean surface than at mid-depth (Fig. 2.2), flow does not literally follow contours of f/H. *Gille et al.* (2004) used float data to examine whether Southern Ocean velocities could be assumed to be equivalent barotropic (EB), meaning that velocities attenuate with depth, with a fixed e-folding scale (*Killworth*, 1992). In such a flow field the mean velocity is close to self-similar in the vertical direction, i.e., velocity at one depth is parallel and also proportional to the velocity at adjacent depth (*Krupitsky et al.*, 1996). An EB model considers the velocity structure as EB. The conventional barotropic model is a particular case of the EB model. Such models widely known in atmospheric sciences since the application to the numerical weather forecasting by *Charney and Eliassen* (1949). Primarily similar approach was used to estimate the density distribution in the ocean. Later on, such models have been studied in the context of the Southern Ocean (*Ivchenko et al.*, 1999; *Krupitsky et al.*, 1996; *LaCasce and Isachsen*, 2010).

As it mentioned before, in an EB flow, the variables (e.g. velocity and pressure) vary with depth, but the direction of flow does not. Thus, horizontal velocity vector and pressure can be define in terms of surface velocity and pressure and a vertical structure function as

$$(p, \vec{u})(x, y, z, t) = (p_s, \vec{u}_s)(x, y, t) P(z), \tag{2.8}$$

where $\vec{u}$, $\vec{u}_s$ and p, p_s are velocity and pressure and their corresponding surface values, respec-

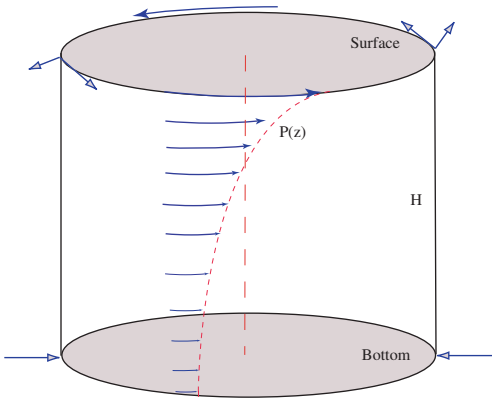

Figure 2.2: Schematic of equivalent barotropic model spin-up.

tively. $P(z) = \exp(z/h_0)$ is a vertical structure function, where h_0 is e-folding scale.

Assuming a linear bottom drag in line with *Isachsen et al.* (2003), yields $\vec{\tau}_b = R\vec{u}(-H) = r_e\vec{u}_s$, where R is the bottom friction coefficient, and r_e is modified drag coefficient. Noting that the surface pressure is proportional to the sea surface height, η, and substituting these into linear depth-integrated horizontal momentum equation and taking curl yields the equivalent barotropic potential vorticity equation

$$\frac{\partial}{\partial t}\nabla \times \vec{u}_s + J\left(\psi, \frac{f}{F}\right) = \nabla \times \frac{\vec{\tau}_s}{\rho_0 F} - \nabla \times \frac{r_e\vec{u}_s}{F}, \tag{2.9}$$

where ψ is transport streamfunction and Jacobian term $J(\psi, f/F) = F\vec{u}_s \cdot \nabla(f/F)$ is the advection of PV by flow. Under this assumption, (2.9) is dominated by the advection term, i.e. $J(\psi, f/F) = 0$. Therefore, flow is predicted to follow contours of f/F, i.e. the geostrophic contours in the EB model, where $F = h_0\left[1 - exp(-H/h_0)\right]$ (e.g. (*Marshall*, 1995; *Krupitsky et al.*, 1996; *LaCasce and Isachsen*, 2010)). Baroclinicity of the velocity structure determines e-folding scale. For small e-folding scales, i.e. for $h_0 \leq H$, F is approximately constant and the PV gradient is dominated by planetary β. In the limit where the e-folding scale, h_0, is infinite, this is equivalent to assuming that flow follows f/H contours, and the barotropic model is recovered.

The flow response to forcing can be better understood by invoking the continuity equation and eliminating the advection term by integrating (2.9) over a closed f/F contour.Taking a Fourier transform in time yields

$$\oint_{f/F}\left(i\omega + \frac{r_e}{F}\right)\vec{\tilde{u}}_s \cdot dl = \oint_{f/F}\frac{\vec{\tilde{\tau}}_s}{\rho_0 F} \cdot dl, \tag{2.10}$$

where $\left[\vec{\tau}_s,\ \vec{u}_s\right](x, y, t) = \sum_\omega \left[\vec{\tilde{\tau}}_s,\ \vec{\tilde{u}}_s\right](x, y, \omega)\exp(i\omega t)$. An inbalance between the net diverging or converging Ekman transport, i.e. RHS term in (2.10), and the net transport in the bottom layer, i.e. the second term on the LHS in (2.10), results in a change in the circulation around closed PV contour. Here the surface circulation depends on the modified bottom friction co-

efficient, the forcing frequency, and modified depth, F. At low frequencies ($\omega \ll r_e/F$), the circulation is in phase with the forcing. At very high frequencies, the circulation lags the wind by $\pi/2$, and is independent of the friction. The EB model flow senses less topographic control than a barotropic one. The lowest-order velocity at everywhere on the closed PV contour and SLA can be determined from (2.10).

2.2 Wave-induced flow

A net particle drift may occur for all cases of progressive wave motion (e.g. water waves, tides and atmospheric waves). *Stokes* (1846) derived expressions for water wave drift in an inviscid fluid. This nonlinear phenomenon extended to viscous fluids by *Longuet-Higgins* (1953). When we consider linear waves, the particles move in closed circles in deep water. But, without linearization, the individual fluid particles have a net drift in the direction of wave propagation. In reality, the path of the fluid particles under progressive waves has a nearly closed shape. But, the velocity of the fluid particles is slightly larger near the surface, than deeper down. Hence, averaging the particles trajectory over a predefined amount of time, i.e. one wave period, yields a small displacement of the particle in the direction of the wave propagation, i.e. the Stokes drift (Fig. 2.3).

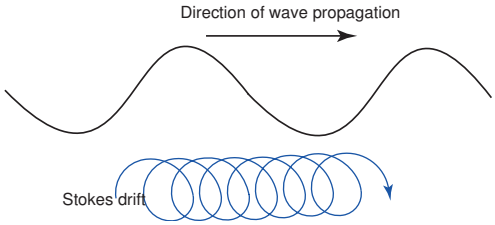

Figure 2.3: Sketch of nonlinear motion of a fluid particle due to propagating wave.

The Stokes drift is important for understanding the fundamentals in surface ocean dynamics and mixing. In particular, it plays an essential role in the oceanic Langmuir circulation (*McWilliams et al.*, 1997). Concerning its applications, adding an accurate assessment of the Stokes drift in ocean model systems is of utmost importance in mapping out surface dynamics, and increases the predictability of surface currents (*Röhrs et al.*, 2012). Furthermore, Stokes drift should be considered as an important factor in coastal process studies, especially in the area of sediment transport, see e.g. (*Longuet-Higgins*, 1953; *Nielsen*, 1992; *Vittori and Blondeaux*, 1996; *Blondeaux et al.*, 2002, 2012).

Consider a fluid particle initially located at $\vec{r}_o = (x_0, y_0, z_0)$ at time $t = t_0$, shifting to $\vec{r}_L = \vec{r}_0 + D\vec{r}$ at a later time t. The expression $D\vec{r} = \int_{t_0}^{t} \vec{v}_L(\vec{r}_0, t')dt'$ determines the fluid particle displacement in the time interval $t - t_0$, where $\vec{v}_L$ is Lagrangian velocity. The net displacement of the particles under wave influence can be obtained from the Lagrangian velocity. With regard to Eulerian specification, the relation between Lagrangian and Eulerian velocities is

$$\vec{v}_L(\vec{r}_0, t) = \vec{v}_E(\vec{r}_L, t) = \vec{v}_E(\vec{r}_0 + D\vec{r}, t). \tag{2.11}$$

Hence, from a Taylor series expansion we obtain

$$\vec{v}_L(\vec{r}_0, t) = \vec{v}_E(\vec{r}_0, t) + D\vec{r} \cdot \nabla_L \vec{v}_E + (\mathcal{H}.\mathcal{O}.). \tag{2.12}$$

The first term on the RHS is traditional Eulerian velocity, while the second term is the Stokes drift ($\vec{v}_S$). The ratio of the second term of (2.12) to the first term is of the order of the wave steepness ($\epsilon = kA$). Under the hypothesis of small wave steepness, the difference between $\vec{v}_L$ and $\vec{v}_E$ is negligible in the second term. Thus, the mean Lagrangian velocity correct to the second order wave steepness is given by

$$\bar{\vec{v}}_L = \bar{\vec{v}}_E + \bar{\vec{v}}_S, \tag{2.13}$$

where $D\vec{r} = \int_{t_0}^{t} \vec{v}_E(\vec{r}_0, t')dt'$, and the balance to the second order is obtained by averaging (2.12) over a wave period, denoted by an over-bar. Hence, the Lagrangian mean current is composed of Stokes drift plus a mean Eulerian current. While the former is inherent in the wave itself, the later depends on friction. Since the Stokes drift arises from the average of the wave motion along a Lagrangian trajectory, it is relevant for all floating and suspended particles present in the water column, and not only for fluid particles considered in the original derivation. This drift is basically related to the net particle motion in inviscid waves, and there is no Stokes drift in the cross-wave direction.

2.3 On the Stokes edge wave

Before we commence on this task, it would be appropriate to indicate why an understanding of this phenomenon, and the mechanisms that can bring it about, are important. Although, from Stokes' time to at least the later editions of Lamb's text on hydrodynamics it was generally thought that the edge waves were a mathematical curiosity, this is no longer the case. Apparently, many near-shore processes are controlled (or significantly affected) by the presence of edge waves (*LeBlond and Mysak*, 1978). Thus, edge waves play an important role in the dynamics of the coastal zone, beach erosion processes, and energy and momentum transfer (*Ghaffari and Weber*, 2014; *Weber and Ghaffari*, 2009; *Weber and Støylen*, 2011). Standing edge waves, in particular, is likely to have an observable effect on beach erosion and, perhaps, on the formation of sand bars close inshore. Edge waves are often considered as the major factor of the long-term evolution of the irregular coastal line, forming rhythmic crecentic bars (*Bowen and Inman*, 1971; *Kurkin and Pelinovsky*, 2003). These, and other more practical aspects, are described in *Howd et al.* (1992) and in the many papers cited therein. Our main concern in this study is the Stokes edge wave (*Stokes*, 1846) and the associated mass transport, which is the first mode in the spectrum of the shelf mode that contains both discrete and continuous parts, e.g. see (*Eckart*, 1951; *Ursell*, 1952; *Reid*, 1958). The essential features of this solution are described in *Lamb* (1932), although it was *Ursell* (1952) which gave the first complete description of the linear problem (being a mixture of continuous and discrete spectra). Several mechanisms for edge wave generation are possible in nature; Direct wind stress, passing atmospheric fronts, and tsunamis can generate large-scale; nonlinear interaction of wave groups and subharmonic resonance may trigger medium and small-scale edge waves, e.g. see (*Ghaffari and Weber*, 2014;

Weber and Ghaffari, 2009). Other mechanisms for the generation of edge waves are described by *Evans* (1989).

2.3.1 Mass transport in the Stokes edge wave in a rotating ocean

In earlier studies mass transport associated to edge waves has been investigated in the viscous laminar bottom boundary layer (*Dore*, 1975; *Mok and Yeh*, 1999). In practice, bottom boundary layers are turbulent and an additional mean interior Eulerian current is generated by frictional effect at the bottom. In this section we focus on the mass transport induced by the Stokes edge waves in a turbulent ocean.

We consider trapped surface gravity waves in a homogeneous rotating ocean ($f > 0$), with a linearly sloping bottom. The motion is described in Cartesian coordinate system, where x-axis is situated at undisturbed surface and directed into the semi-infinite ocean, y-axis is directed along coastline. The bottom is given by $z = -h = -x\tan\beta$, where $\beta\,(\leq \pi/2)$ is the slope angle, and free surface by $z = \eta$. Mean horizontal volume fluxes are defined as depth integrated

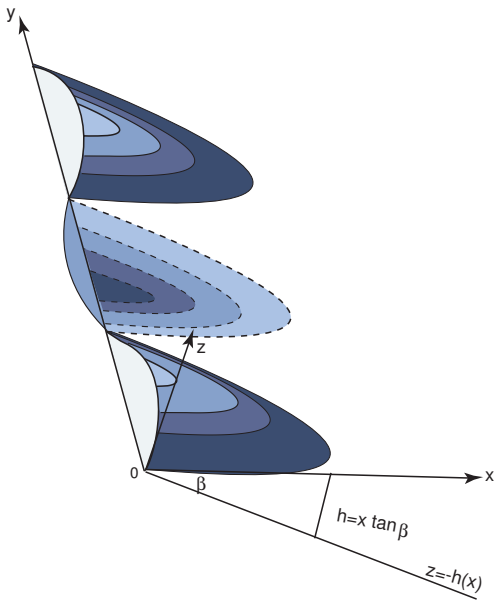

Figure 2.4: Sketch depicting the coordinate system, with the surface and sloping bottom included; y-axis is the along-shore coordinate and the seawards direction is $x \to \infty$.

velocities

$$\bar{U} = \overline{\int_{-h}^{\eta} u dz}, \qquad \bar{V} = \overline{\int_{-h}^{\eta} v dz}. \tag{2.14}$$

Since the velocities are integrated between material surfaces, they are actually the Lagrangian fluxes (*Phillips*, 1966; *Weber et al.*, 2006). Integrating the governing equations in the vertical between material surfaces, and utilizing full nonlinear boundary conditions, we obtain the mean

wave induced drift correct to second order in wave steepness (*Phillips*, 1966)

$$\frac{\partial \bar{U}}{\partial t} - f\bar{V} + gh\frac{\partial \bar{\eta}}{\partial x} = -\frac{\partial}{\partial x}\int_{-h}^{0}\frac{\bar{p}_d}{\rho}\,dz - \frac{g}{2}\frac{\partial}{\partial x}\overline{\tilde{\eta}^2} +$$

$$\frac{\bar{p}_d(-h)}{\rho}\tan\beta - \frac{\partial}{\partial x}\int_{-h}^{0}\overline{\tilde{u}\tilde{u}}\,dz - \frac{\partial}{\partial y}\int_{-h}^{0}\overline{\tilde{u}\tilde{v}}\,dz - \tau_1$$

$$\frac{\partial \bar{V}}{\partial t} + f\bar{U} + gh\frac{\partial \bar{\eta}}{\partial y} = -\frac{\partial}{\partial y}\int_{-h}^{0}\frac{\bar{p}_d}{\rho}\,dz \tag{2.15}$$

$$-\frac{g}{2}\frac{\partial}{\partial y}\overline{\tilde{\eta}^2} - \frac{\partial}{\partial x}\int_{-h}^{0}\overline{\tilde{u}\tilde{v}}\,dz - \frac{\partial}{\partial y}\int_{-h}^{0}\overline{\tilde{v}\tilde{v}}\,dz - \tau_2,$$

$$\frac{\partial \bar{\eta}}{\partial t} = -\frac{\partial \bar{U}}{\partial x} - \frac{\partial \bar{V}}{\partial y},$$

where, g is the gravitational acceleration, tilde represents wave quantities, and $\bar{p}_d$ is the non-hydrostatic (dynamic) pressure. Here, τ_1 and τ_2 are the mean turbulent bottom stress components per unit density in x and y-axis direction, respectively. The mean bottom pressure term in the x-momentum, i.e. $\bar{p}_d(-h)\tan\beta/\rho$, was missing from Phillips' derivation; see *Mei* (1973); *Ghaffari and Weber* (2014); *Weber and Ghaffari* (2009). Above equations set contains non-linear wave forcing terms. The wave-induced mass transport which is calculated indeed is Lagrangian transport; Stokes drift plus Eulerian mean current arise by friction. We separate the effect of friction on the wave motion and the mean flow. In this problem the oscillatory wave motion is influenced by viscosity acting in thin surface and bottom boundary layers. Within the top and bottom boundary layers the wave velocity varies rapidly with height, while in the interior part the variation is that of inviscid waves.

In this analysis we assume that the boundary layers thickness (δ) are quite thin, i.e. $\delta < h$, hence, its contribution in wave velocity is negligible. Therefore, for the linear wave we impose a no-slip, no surface stress condition and only the inviscid part of the solution with a damped amplitude is used. The damping rate is determined by bottom boundary layer in shallow-water with a no-slip bottom. While, in deep water the corresponding damping rate is proportional to the square of the wave number. Hence, for a given wavelength, the Stokes edge wave at certain distance from the coast may be characterized as a shallow-water or a deep-water wave for small and large slope angles, respectively. We have resorted an averaging procedure for determining the damping rate using the total mean energy and mean dissipation in the trapped zone, for all admissible slope angles.

The linearized equations for the damped interior wave motion by adopting the aforementioned approach become

$$\vec{\tilde{u}} = -f\hat{k}\times\vec{\tilde{u}} - \frac{1}{\rho}\nabla p - g\hat{k} - r\vec{\tilde{u}}, \qquad \nabla\cdot\vec{\tilde{u}} = 0, \tag{2.16}$$

where $\hat{k}$ is unit vector in z-direction. The resulting linearized surface wave, which is trapped

and may travel in both direction along the coast, is

$$\tilde{\eta} = \eta_0 \exp(q) \cos(\theta), \tag{2.17}$$

where η_0 is arbitrary constant, $q = -a_r x - \alpha y + b_r z$ is the exponential decay, and $\theta = -a_i x + k y + b_i z - \omega t$ is the phase function. Additionally, $a = a_r + i a_i$ and $b = b_r + i b_i$ are complex parameters. In that connection, it can be readily seen that trapping at the coast requires $a_r > 0$. In this calculation a_r has two roots, i.e. a_{r+} and a_{r-}. In order to have trapped wave propagating in positive and negative along-shore directions, we must exclude the a_{r-} solution. In this analysis we take that the frequency ω is real, while the wave number is complex, i.e. we consider spatial damping waves. Hence,

$$\kappa = k + i\alpha, \tag{2.18}$$

where α is the spatial damping rate in along-shore direction. The effect of the friction is attenuating the real part of the wave velocity components show that the wave motion in the Stokes edge wave occurs in planes parallel to the sloping bottom.

Following *Longuet-Higgins* (1953), the along-shore Stokes flux to the second order in wave steepness can be easily obtained from linear wave solution by integrating Stokes drift in vertical between material surfaces. However, in vertical limit ($\beta = \pi/2$) the problem should be treated with some care. In this case, trapping requires $\omega < 0$, and the resulting motion is coastal Kelvin wave propagating with the coast, i.e. the vertical wall, to the right ($f > 0$). In this limit the Stokes flux must be obtained by integrating the Stokes drift in vertical from minus infinity to zero. As discussed in section 2.2, the Stokes drift is related to the net particle motion in inviscid waves. Therefore, there is no Stokes drift in cross-wave direction. However, the presence of friction in the fluid introduce a small drift in the cross wave propagating direction, which is inseparable from Eulerian current. Hence, we take the Stokes flux in x-direction is zero, and only the along-shore Stokes flux contributes in total wave momentum (M_w), in the trapped zone. By comparing with total energy density in the trapped zone, we note that $E = M_w c^*$, where $c^* = \omega/k - (f \cos\beta)/(2k)$.

The mean wave-induced Lagrangian fluxes are obtained by integrating the momentum equation in vertical between material surfaces (2.15). The mean motion in cross-shore direction is quite small, and we neglect the effect of friction in this direction. But, the friction term in the along-shore direction must be modeled. It is almost common to use a bottom stress proportional to the square of the mean velocity (*Weber and Ghaffari*, 2009; *Weber and Støylen*, 2011). Defining and using a friction coefficient that is proportional to characteristic velocity; see *Nøst* (1994), not only provides identical effect, but also makes bottom friction linear in terms of the mean velocity. The present approach separates the decay of wave momentum from the frictional influence on the mean flow (*Jenkins*, 1989; *Weber and Melsom*, 1993; *Ardhuin and Jenkins*, 2006). As the cross-shore Stokes flux is zero in this problem, following *Phillips* (1966) the mean Eulerian volume flux in this problem can be written

$$\bar{U}_E = \bar{U}_L, \qquad \bar{V}_E = \bar{V}_L - \bar{V}_S, \tag{2.19}$$

where subscripts L, E, and S denote the Lagrangian, the Eulerian and the Stokes fluxes, re-

spectively. Utilizing 2.19, the steady state governing momentum equations 2.15 then reduce to

$$x\frac{\partial^2 \tau_2}{\partial x^2} - 2\alpha f \bar{V}_E = 2\alpha \left(f\bar{V}_S - \frac{\partial S}{\partial x} \right), \tag{2.20}$$

where S is the total wave-forcing stress component (*Ghaffari and Weber*, 2014). We introduce a non-dimensional Eulerian velocity Q_E and the non-dimensional Stokes drift velocity Q_S. Eventually, the vertically-averaged non-dimensional Lagrangian drift velocity Q_L becomes

$$Q_L = Q_E + Q_S \tag{2.21}$$

The non-dimensional form of 2.20 indicates that for the damped Stokes edge wave that propagate in with the coast to the left in the northern hemisphere, both induced Stokes drift and fractionally induced Eulerian current are trapped over the slope. On the other hand, for the damped Stokes edge wave propagating with the coast to the right, the induced Stokes drift is trapped over the slope, but the Eulerian current is not trapped. Solutions of the non-dimensional form of (2.20) attained using exponential integrals and numerical evaluation.

2.3.2 Mass transport in the Stokes edge wave in a non-rotating ocean

In this study we look at the Stokes edge waves in a non-rotating ocean. Therefore, the terms corresponded to the Coriolis force are disregarded from the momentum equation. We apply an analysis similar to that of rotating ocean. We consider trapped surface gravity waves in a homogeneous incompressible fluid with linearly sloping bottom. The motion is described in a Cartesian system, with similar configuration as section 2.3.1. We investigate the nonlinear mass transport by applying an Eulerian description of motion, and expanding the solution in series after wave steepness as small parameter. An analytical expression for the vertically-averaged Lagrangian drift velocity is derived by integrating the governing equations in the vertical between material surfaces. Utilizing the full nonlinear boundary conditions at the free surface and the sloping bottom, we obtain the mean quantities correct to second order in wave steepness. This drift is composed of Stokes drift plus Eulerian drift arises from the effect of friction. Here, the effect of friction on the wave motion and the mean flow should be separated. In general; for deep water waves, viscosity will affect the motion in the bulk of fluid, while for shallow water the viscous boundary layer at the bottom will dominate. In both cases the potential part of the wave field will attenuate exponentially in time. We can obtain the potential part of the wave field by using a friction that is linear in the wave velocity, e.i. $-r\vec{\tilde{u}}$, where constant friction coefficient r depends on viscosity. We can apply the potential theory of *Stokes* (1846), since this friction does not introduce vorticity into the fluid. Therefore, we can write the linearized complex velocity potential for the spatially damped Stokes edge wave in non-rotating ocean as

$$\tilde{\phi} = -\frac{i\eta_0\omega}{k\sin\beta} \exp\left(-kx\cos\beta - kz\sin\beta - \alpha y + i\left(ky - \alpha x\cos\beta + \alpha z\sin\beta - \omega t\right)\right), \tag{2.22}$$

where η_0 is wave amplitude, ω is wave frequency. Due to friction, the wave number κ in y-direction is complex, i.e. $\kappa = k + i\alpha$, where α is the small spatial attenuation coefficient. Introducing the velocity potential makes the problem quite easy to obtain analytical expressions.

Following *Longuet-Higgins* (1953), the Stokes drift to second order in wave steepness for this problem is easily obtained from the linear wave solution.

In order to evaluate the steady mass transport, the turbulent bottom stresses are modeled as to be proportional to the square of the mean Eulerian flux $\bar{V}_E$. The bottom friction is neglected in the direction normal to the wave propagating direction, as the velocities are small. Therefore, turbulent bottom stress in along-shore direction can be written as

$$\frac{\bar{\tau}}{\rho} = \frac{c_D|\bar{V}_E|\bar{V}_E}{h^2}, \tag{2.23}$$

where c_D is a bottom drag coefficient, ρ is density, and h is local depth. The friction induced along-shore mean Eulerian volume flux becomes

$$\bar{V}_E = \bar{V}_L - \bar{V}_S, \tag{2.24}$$

where the mean Lagrangian flux, $\bar{V}_L$, is derived by integrating the governing equations in the vertical between material surfaces, and the Stokes flux is readily obtained from linear wave field. Furthermore, it is easy to show that $|\bar{U}_E/\bar{V}_E| = \mathcal{O}(\alpha/k)$, which justifies the neglect of the cross-shore velocity in the bottom drag. We realize that this problem is the special case of the Stokes edge waves in the rotating ocean. By excluding the Coriolis parameter $(f = 0)$, from the expressions, all quantities in the rotating case simply recover the non-rotating case quantities; see *Ghaffari and Weber* (2014).

2.4 On internal waves

In general, gravity waves can form at the interface between fluids of different densities or in fluids with a continuous (stable) stratification. Most bodies of water at mid and lower latitudes have a pronounced vertical stratification. Internal waves can be triggered in a variety of ways, e.g. by the action of moving weather fronts, tides, wind stress, boats, currents moving over topography. Since the density difference between different layers in a stratified fluid is quite small, internal waves appear with longer periods, and larger amplitudes when compared to surface gravity waves. Internal waves are ubiquitous in the interior of the oceans and have been the focus of much attention in recent years due to their role in oceanic mixing and mass transport. Nonlinear effects associated with internal waves include the transport of water along with suspended mass such as sediment, nutrients, larvae, as well as contaminants. The details of such effects are crucial to the understanding of a wide array of physical situations where transport by internal waves is inherent. *Leichter et al.* (1996) showed that internal tides play an important role in relocating of larvae and other organisms to the near shore, and have remarkable influence in the development of the benthic communities. Additionally, they showed that the spatial distribution of plankton and consequently nutrient dispersal in coastal regions are strongly influenced by high frequency internal waves. Internal waves can be of particular interest in terms of the transport of contaminants at beaches (*Boehm et al.*, 2002a,b).

2.4.1 Mass transport in internal coastal Kelvin waves

In small bodies of water with negligible tidal forcing, internal waves appear to be triggered by temporal/spatial variation of the wind field. A stable stratified configuration along with a straight coastline, makes that coastal region to act as a waveguide for internal Kelvin waves. It is common to use a reduced-gravity model, which consider two layers of constant density, e.i. the upper thin and active, and the lower deep and quiescent layer, in such configurations. We will not use the reduce gravity model, as it filters out the higher baroclinic modes, and provides an erroneous results for the Stokes drift. The main focus of the present study is the main drift induced by internal coastal Kelvin waves. That drift may have influence on relocating bio-materials, suspended loads, pollutants, and also may be contribute in general circulations of the water bodies in question. We consider a stratified ocean of constant depth H, and Cartesian coordinate system, where the x-axis is directed in along-shore, and y-axis directed cross-shore. By using an Eulerian description of motion, and exploiting the hydrostatic approximation and

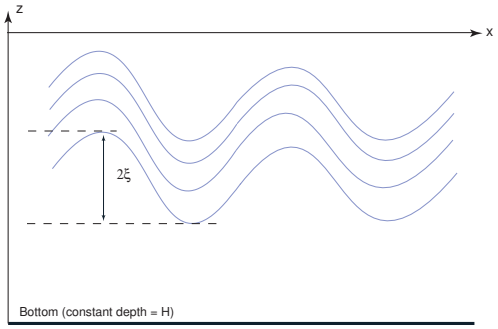

Figure 2.5: Sketch depicting the coordinate system, with constant bottom included; x-axis is the along-shore coordinate and the seawards direction is $y \to \infty$.

Boussinesq approximation of density ρ, the governing equations become

$$\frac{\partial \vec{v}_h}{\partial t} + \vec{v} \cdot \nabla \vec{v}_h = -f\vec{k} \times \vec{v}_h - \frac{1}{\rho_r}\nabla_h p + \frac{\partial}{\partial z}\left[\frac{\vec{\tau}_h}{\rho_r}\right],$$

$$\begin{aligned} \frac{\partial p}{\partial z} &= -\rho g, \\ \frac{\partial \rho}{\partial t} + \vec{v} \cdot \nabla \rho &= 0, \\ \nabla \cdot \vec{v} &= 0, \end{aligned} \tag{2.25}$$

where, $\vec{u}$ is the velocity vector, p is pressure, $f > 0$ is the Coriolis parameter, $\vec{\tau}_h$ is the horizontal turbulent stress, and ρ_r is a constant density. We take there is no friction from atmosphere. The mean horizontal Lagrangian transport $(\bar{U}_L, \bar{V}_L)$, correct to second order in wave steepness, is obtained by integrating the governing equation in vertical between the bottom and the moving surface. Mean horizontal volume fluxes are defined as (2.14). As discussed in previous sections, the mean horizontal Lagrangian flux is Stokes flux plus mean Eulerian flux (*Phillips*, 1966). We consider trapped internal Kelvin waves, which is generated by small perturbations

of stratification from its state of rest, traveling in along-shore direction. Introducing the vertical displacement of the isopycnals from their original position and Brunt-Väisälä frequency $N^2 = -gd\rho_0(z)/(\rho_r dz)$, the linearized equations for internal Kevin waves is obtained from (2.25). The variables may be separated into normal modes (*Lighthill*, 1969; *Gill and Clarke*, 1974). By inserting pressure normal modes into linearized momentum equation in z-direction, it is easy to show that the eigenfunctions ϕ_n are solutions of

$$\phi_n^{''}(z) + \frac{N^2}{c_n^2}\phi_n(z) = 0, \tag{2.26}$$

where, c_n is the constant eigenvalue. Assuming a rigid lid at the surface, i.e. $\phi_n = 0$, at $z = -H, 0$, that eigenfunctions $\phi_n^{'}$, constitute an orthogonal set for arbitrary Brunt-Väisälä frequencies. Utilizing the orthogonality condition and modeling the friction by a turbulent coefficient of momentum ν_T (*Williams and Gibson*, 1974), we find the governing equations for mode n, where the along-shore linear wave velocities and wave amplitudes must be vanished as $y \to \infty$. The resulting linear internal coastal Kelvin wave motion for mode n becomes

$$\bar{\xi} = \sum_{n=1}^{\infty} \xi_n(x, y, t)\phi_n(z). \tag{2.27}$$

Here

$$\xi_n = \xi_{0n} \exp(-\alpha_n x - a_n^{-1} y) \cos(k_n x + l_n y - \omega t), \tag{2.28}$$

where, α_n and k_n are spatial decay rate and wave number in along-shore direction, respectively. Furthermore, a_n and l_n are the internal Rossby radius and the friction-induced wave number in the y-direction, respectively. We note that the co-phase lines are slanted backwards for spatially damped coastal Kelvin waves. It is shown that the associated Stokes volume flux for internal coastal Kelvin waves is zero. Therefore, in this problem, the mean Eulerian volume flux is determined entirely by mean Lagrangian flux:

$$\bar{U}_L = \bar{U}_E, \qquad \bar{V}_L = \bar{V}_E. \tag{2.29}$$

Hence, the mean Eulerian velocities can be determined to second order in wave steepness from (2.25).

Chapter 3

Observations

3.1 The Caspian Sea

The Caspian Sea (CS) is the largest inland water body of the world with a surface area of 379000 km^2, a drainage area of approximately 3.5 million km^2, and a volume of $78000\,$km^2 (*Ghaffari and Chegini*, 2010; *Zaker et al.*, 2007, 2011). This lake is located at northern hemisphere between latitudes of 36° and 45°. Conventionally southern, central and northern basins are distinguished. The Southern and the central basins of the CS have maximum water depths of 1025 and $788\,$m, respectively. These basins are separated by a sill with a maximum depth of about $170\,$m and the northern basin with maximum depth about $20\,$m is a very thin extension of the central basin. The f/H contours in the Caspian Sea are indeed closed in both the central and southern basins (Fig. 3.1).

The vertical structure and evolution of the density field is a function of both salinity and temperature. Salinity in the CS is relatively constant with depth, and the density gradient can be to a first approximation considered proportional only to the temperature gradient. In the southern basin, the surface densities are significantly weaker, producing larger near-surface gradients (*Ghaffari et al.*, 2010, 2013). The process of hydrological fields transformation, redistribution of biogenic and pollutant substances depends significantly on horizontal circulation of the CS, which for different reasons have not been studied enough (*Ghaffari and Chegini*, 2010). Main circulations in the CS consist of cyclonic eddies (*Terziev et al.*, 1992) and meso-scale eddy features which have seasonal evolution (*Trukhchev et al.*, 1995). Due to lake of tide, the CS currents are considered to be mainly wind-generated. Wind and traveling weather fronts transfer momentum directly as wind driven currents and indirectly by triggering different sort of surface and internal waves. For instance, the periodic occurrence of rip currents and formation of cusp-type beach, which are indications of edge waves on natural shorelines (*Bowen and Inman*, 1969, 1971), were stated by *Sonu et al.* (1969) in the CS . Furthermore, pronounced vertical stratification in the southern basin (*Ghaffari et al.*, 2010) along with straight coast, make that coastal region favorable for internal wave generation and propagation. Other types of currents, e.g. baroclinic currents and seiches also play important roles in local circulation patterns (*Sur et al.*, 2000). Over the central and southern basins of the CS, the main features of circulation are a cyclonic (*Ghaffari and Chegini*, 2010). Although various field measurements were carried out in the northern and the central basins of the CS (*Bondarenko*, 1993, 1994; *Kosarev*, 1975),

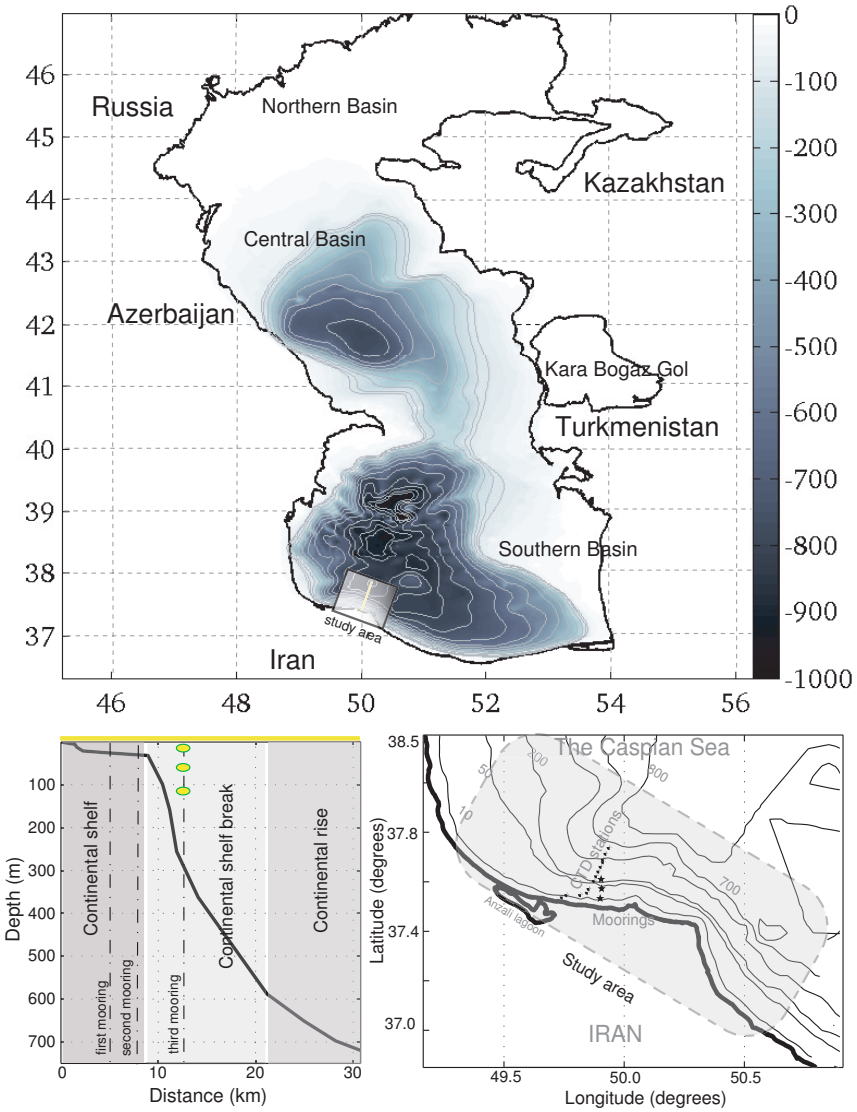

Figure 3.1: The Caspian Sea; upper panel: the bathymetric field (shown as gray shading), and potential vorticity field (contours); lower panel: shelf profile and location of field observations.

but only a few number of measurements in order to investigate the coastal flow field have been accomplished in the southern basin direct (*Ghaffari and Chegini*, 2010; *Ghaffari et al.*, 2010, 2013; *Zaker et al.*, 2007, 2011).

3.2 Field measurements

3.2.1 Study area

The study area is located in the southwestern part of the CS (Fig. 3.1). The depth decreases gently from the coast to approximately -50 m near the shelf break in almost 10 km, after that it sharply decreases to ~ 800 m in 25 km. According to the bathymetric features, the continental shelf spreads from the coast up to about 10 km seaward with mild declination, which ensues by a drastic depression (the continental shelf break) extends to 20 km seaward and hits its lowest point at 600 m (Fig. 3.1). The continental rise commences from this point and goes down with a relatively mild slope with respect to the continental shelf break toward the abyssal plain . The continental shelf in the southern coastal areas is fairly narrow and topographic contours are parallel to the coastline (*Ghaffari et al.*, 2010; *Ghaffari and Chegini*, 2010; *Zaker et al.*, 2007).

3.2.2 Satellite observations

Satellite observations (from January 1992 to December 2011, available at www.aviso.com) are utilized to study the basin-scale spatial and temporal variations of Sea Level Anomaly (SLA) in the CS. We use empirical orthogonal function (EOF) analysis to extract coherent variations that are dominant, i.e. possible spatial modes of variability and how they change with time. Utilizing that procedure, the spatial-temporal anomalies of the dataset is decomposed into its leading patterns. In fact, by computing the eigenvalues and eigenvectors of a spatially weighted anomaly covariance matrix of a field, the leading patterns in both time (Principal Component, PC) and space (EOF) are determined.

The leading orthogonal function (EOF1) is remarkably similar to the f/H field in the central basin. However, in the southern basin the the response is less clear. The first principal component (PC1), the time series associated with EOF1, accounting for 92% of the total variance in the SLA field. The remaining higher EOFs account for only 8% of the variance, which are less likely to be effective in dynamical posses of the basins (Fig. 3.2). As may one can expect, the northern shallow extension of the CS display entirely separate pattern mostly under the influence of the Volga River runoff.

3.2.3 Current meter observations

Three moorings were deployed in a line perpendicular to the coastline from November 2004 to early May 2005, in order to record the flow field over the south-western shelf of the CS . The moorings were located over the 20 m, 50 m and 230 m isobaths at [$37.505\,^{\circ}$N; 49.865°E], [37.531°N; 49.866°E], [37.553°N; 49.864°E], respectively. Recording Current Meters (RCM 9) were installed near the surface, mid-depth (for the 230 m mooring), and near the bottom, aiming to provide current profiles throughout the water column. In order to capture fine details of the

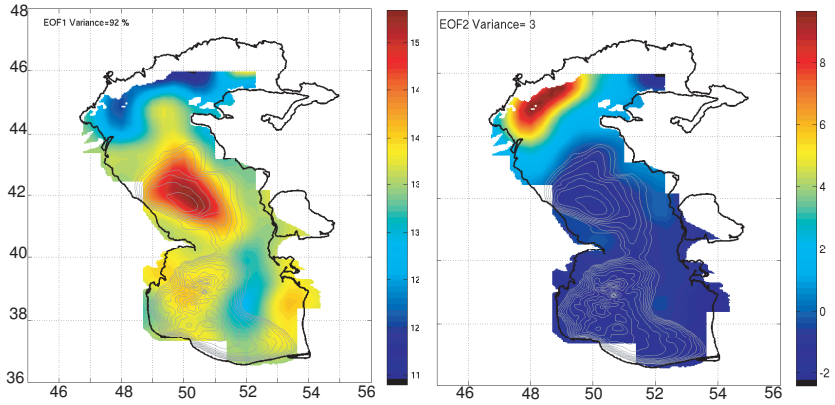

Figure 3.2: EOF analysis of SLA for the CS over f/H contours. Leading (right) and second (left) EOFs, which accounts for 92% and 3% of total variance in the field, respectively.

flow field, the sampling frequency was originally set to 3 cph. However, the analysis presented here is based on daily averaged time series. Furthermore, the currents were decomposed into along-shore and cross-shore components based on their principal axes. Figure 3.3 shows the along-shore daily averaged current time series for the three moorings. The first two moorings, located on the continental shelf, demonstrate barotropic behavior of the flow field. In the third mooring, strong temporal variations in the flow field corresponding to low frequency motions were captured by all the current meters. However, relatively high frequency signals are not well captured by the lower current meter. The latter instrument was located far below the seasonal thermocline layer. But, estimates of the squared coherences among the current time series of this mooring at various timescales, show high correspondence at periods longer than several days. Therefore, the low frequency fluctuations have appreciable vertical coherence. We use this mooring for further analysis, as it provides a better perspective of the velocity structure in the basin interior.

Our analysis show that the depth averaged velocity accounts for $\sim 85\%$ of the total velocity variance in the study area. Additionally, variance ellipses are formed in order to study the topographic influence on the velocity field. The current ellipses at all depths are anisotropic, and the principal axes of the variabilities are closely aligned with ambient topographic contours in all three moorings. This implies the tendency of the flow to be steered along the topographic contours in the study area. This results are consistent with previous studies which showed the alignment of current ellipses with topographic contours, and almost barotropic (equivalent barotropic) behavior of the flow field in the eastern part of the southern CS (*Ghaffari and Chegini*, 2010; *Zaker et al.*, 2011).

3.2.4 Hydrographic observations

A total of 13 CTD-profiles along a transect extending from the coast towards the offshore region, as shown in Fig. 3.1, were carried out in the early winter and summer of 2008. The stations

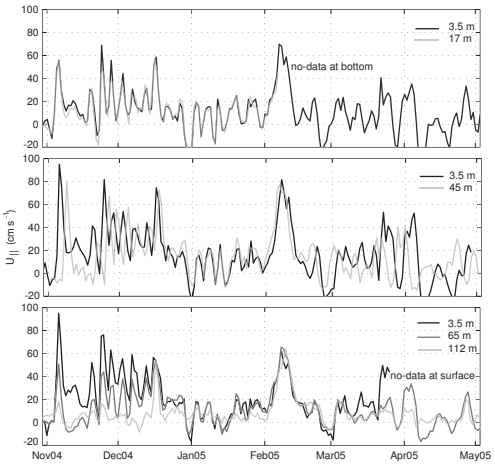

Figure 3.3: Along-shelf currents; first–third mooring from top to bottom respectively for 6 months (November 2004–May 2005). The light gray and black lines show daily averaged velocities for top and bottom current meters, respectively. The dark gray line in the lower panel represents mid-depth observation. Note how nearly barotropic the currents are in the all three stations.

were selected based on the bathymetric contours in approximately 3 km intervals to cover some specific depths along the study area. The first station located at [$37°29.185'$ N; $49°27.959'$ E] and the last one located at [$37°44.121'$ N; $49°40.470'$ E], which hits its lowest point at ~ 750 m depth. According to the bathymetric features, the profiled stations well covered the deepest parts of the south-western waters and could be representative for deep water characteristics in this region. Figure 3.4 shows potential density and temperature structures in the study area based on snapshot hydrographic observation. It reveals strong seasonal thermocline located at ~ 30 m depth, which is typical seasonal thermocline depth in summer for almost whole basin (*Ghaffari et al.*, 2013). Contrary to the strong summer thermocline in southern part of the CS, the water body in the cold phase over the continental shelf break is partially ventilated. Owing to the cold phase erosion, the seasonal thermocline inevitably sinks down to the deeper layers and is located between 80 to 100 m depth, where the water mass is still stratified. As it mentioned before, due to insignificant vertical salinity variation in the CS, temperature structure largely determines the density stratification. Therefore, density stratification is weaker but does not vanish in winter (*Terziev et al.*, 1992; *Kosarev*, 1975; *Ghaffari et al.*, 2010). These observation suggest that the vertical stratification may be important in the study area. Therefore, an equivalent barotropic description of currents seems appropriate. Taking into account the near barotropic structure of the velocity field and presence of a permanent stratification in the southern basin, one can expect that a simplified EB model of wind-driven variability be applicable in this region.

The permanent and profound stratification along with a straight coastline, makes the southern coastal region of the CS an ideal environment for internal Kelvin waves. In general, our understanding of wind-generated surface waves are considerably developed due to the exchange between proper argued theories and careful and extensive observation. However, internal waves studies are lacking in similar prolific interchange not because of the complexity of the problem,

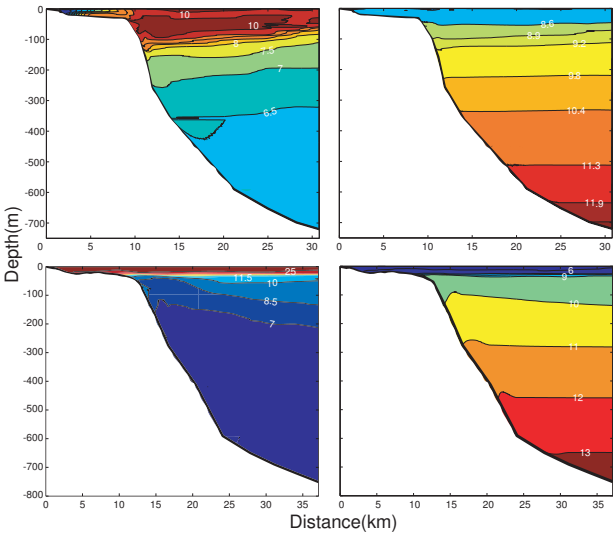

Figure 3.4: Temperature (left) and density (right) structures of the south-western part of the CS for cold (upper) and warm (lower) phases in 2008 (*Ghaffari et al.*, 2010).

but due to difficulty of making significant measurements. Variations in water temperature and salinity at a fixed point depth have often been attributed to internal waves (*Phillips*, 1966). In order to investigate internal waves in the study area, the third mooring was equipped by thermistor chains. Figure 3.5 shows vertical profile of temperature time series from surface to $120\,\mathrm{m}$

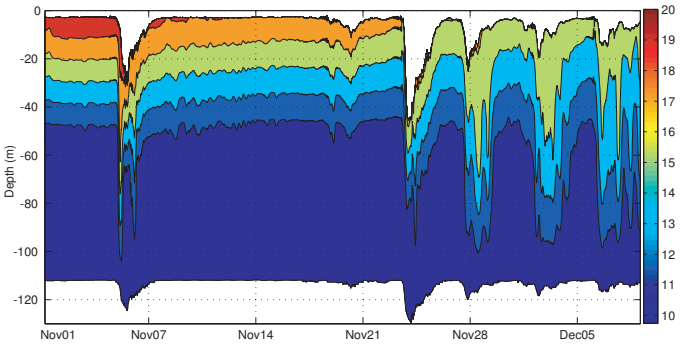

Figure 3.5: Time series of isotherm fluctuations in the south-western part of the CS.

depth. The fluctuation with a period of about 5 days can be considered as indication of internal Kelvin waves. Although little is known about the distribution of the energy among the different internal waves mode, in fairly sharp thermocline the gravest mode may dominate (*Phillips*, 1966). In view of the considerably sharp thermocline in the CS, one may attribute the vertical amplitude of the fluctuations $\sim 40\,\mathrm{m}$ to a first mode internal wave.

In summary, the CS with its bottom contours, sloping beaches and stratification appears to exhibit, or be capable of exhibiting the wind and wave-driven current phenomena discussed in this thesis.

Chapter 4

Results

In the previous chapters, we provided an explanation of why and how our research for each thesis objective was conducted. The results of the research will be addressed briefly in this chapter, and a short discussion of the results will follow. The detailed investigation of each objective and its results are mainly presented in the individual papers.

4.1 Topographic Effects on the Large-scale Flow Field in the Caspian Sea

The barotropic and EB models which are described in chapter 2 are relevant in regions where PV contours are closed. Such models have been used before to investigating wind-driven variability (*Isachsen et al.*, 2003; *Hasselmann*, 1982; *Killworth*, 1992; *Krupitsky et al.*, 1996; *Kamenkovich*, 1962). In this model, the primary component of the flow is parallel to the PV contours. The flow is forced by wind-driven Ekman divergence at the surface and balanced by frictional Ekman convergence at the bottom. As shown in the Fig. 3.1, the PV contours are indeed closed in both the central and southern basins of the CS, and some of them cover both basins. Satellite observation of SSH (Fig. 3.2) show that variability is localized in the basins; this is particularly true in the central basin. *Isachsen et al.* (2003) found that SSH variability was similarly localized in the gyres of the Nordic Seas, and there the f/H model successfully captured a large fraction of the observed variability. Furthermore, in-situ velocity field observations show that the principal axes of the variabilities are closely aligned with ambient PV contours in all three moorings. Therefore, the tendency of the flow to be steered along the topographic contours in the study area, is evident. Despite to the Ekman flux in the surface layer, the flow varies in correspond with the topographic variations, which supports the idea of investigating the role of the topography in controlling the barotropic flow in the CS. In the following, the barotropic linear model will be tested in these basins.

For the atmospheric forcing, we utilized almost 20 years (1992–2011) of wind stress data from the European Centre for Medium-Range Weather Forecasts (ECMWF) operational analysis (available online at http://www.ecmwf.int). The transfer of the atmospheric momentum to the sea can be altered by the sea surface ice coverage but the central and southern parts of the CS are ice-free basins. Bathymetry data for the CS were obtained from the ETOPO2 $(2' \times 2')$ topographic set (available online at http://www.ngdc.noaa.gov). For application in a linear model

of the large-scale flow this topographic data set needs some smoothing, at the same time, excessive smoothing of topographic gradients will lead to underestimated flow strength. However, it is not that straightforward to define the appropriate smoothing scale. In fact, the PV contours can be changed (broader or denser) or disappear with different smoothing bands (*Krupitsky et al.*, 1996). After some testing, we defined the large-scale component of the topography by smoothing the bathymetry to ~ 10 km in both latitudinal and longitudinal directions, at $40°$N.

We first compared the predicted velocity over the closed PV contours with in-situ current observations, i.e., with currents at the deepest mooring there. The other two moorings are in the vicinity of the third one and demonstrate very similar velocity field. The upper panel in Fig 4.1 shows the predicted along-PV currents at the mooring location. The model produces seasonal variation of the mean currents with maximum values in the winter times. Also shown here is the duration of the in-situ current observation in the study area. The lower panel, shows the observed depth-averaged currents against the barotropic model predictions for this period. It is evident that most of the high frequency signals are not captured by the model. Some of the observed low-frequency variations (> 1 month) are captured. But the model predictions are broad and systematically underestimate the observed currents. In fact the model appears to act like as low-pass filter. In order to achieve a proper agreement between the observation and prediction amplitude, we had to use bottom friction coefficient $R = 1 \times 10^{-4}\,\mathrm{m\,s^{-1}}$, a value five times lower than the drag coefficient was used by *Isachsen et al.* (2003). From 2.5, it is easy to see that smaller R values maintains higher amplitudes. On the other hand, small bottom drag coefficient makes $i\omega$ more dominant, which smooths out the predicted current and causes phase shift. Therefore, we expect the high frequency signals are filtered out in our predictions. We see

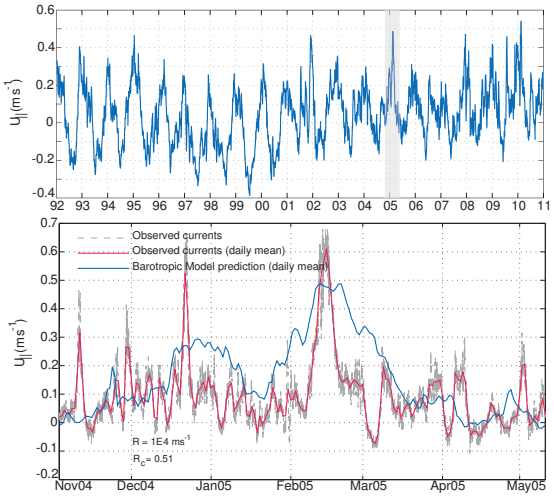

Figure 4.1: The upper panel; the along-PV predicted current (1992–2011). The gray shaded area shows the length of the in-situ current observation. In the lower panel, the gray dashed, red and blue solid lines show the depth-averaged along-PV current based on the recorded (6 cpd), daily mean time series, and the barotropic model prediction, respectively.

some skill and some problems of the model, but really need more observations to learn more. Considering the measurements durations, we do not have sufficient amount of supporting data,

and the comparison is inconclusive. Therefore, we look at altimetry observation. The spatial and temporal structure of the large-scale flow is well captured by satellite altimetry. We compare sea surface height anomalies among two transects over closed PV contours in the central and southern basins of the CS (see Fig. 4.2). The sea level variations between the inner and

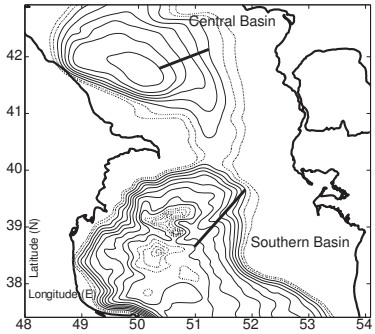

Figure 4.2: Shown in the current figure are the two gyres (in the central and the southern basins) for which the differences in sea level anomalies between satellite observations and model predictions, were compared. The thick lines indicate the integration paths, as well as the outer and inner PV contours. The latter is considered for determining the sea level anomalies for satellite observations.

outer contours are determined using weekly multi-satellite altimetry data from October 1992–December 2010. For model comparison, sea surface anomalies in the southern and the central basins over the sub-basin PV contours (the basin-wide contours were excluded) are predicted in the barotropic equation (2.6). The central region of the southern basin is too flat. In fact, small ups and downs in that region forms several closed cores, and PV contours are rather convoluted. Therefore, we limit our calculations to the continental slope. The barotropic model behaves quite different in the southern and central sub-basins. While the model predicts the sea surface height anomalies relatively well in the central basin, the model performance diminishes in the southern basin (Fig. 3.3). The satellite observations in the central basin reveals seasonal variation with lowest values in winters. This seasonal signal is captured very well by the barotropic model. However, in the southern basin neither the observation nor the model show any clear seasonal cycle. The linear correlation coefficients between the satellite measurements and the barotropic model prediction in the central and the southern transects, are 0.68; 0.51, respectively . The ratio of the RMS of the predicted SLA to the RMS of observed SLA for the central and the southern basins are 0.8 and 0.3, respectively. Ergo, despite the better performance of the model in the central basin, in both cases the predictions are underestimated.

In the barotropic model, the bottom topography is dominant. Weak stratification and equating the surface and bottom velocities to the depth-averaged velocity are bases for preeminent topography in the barotropic solution. In fact, the topographic steering depends on both the stratification and strength of the bottom currents. The topographic steering is attenuated by the stratification, since the velocity decreases from the surface to the bottom in a stratified water body. Additionally, the potential density distribution reveals that the southern basin is more stratified comparing to the central basin. A measure of the relative importance of stratification and rotation within a flow field is the Burger number. Estimations of the Burger number for

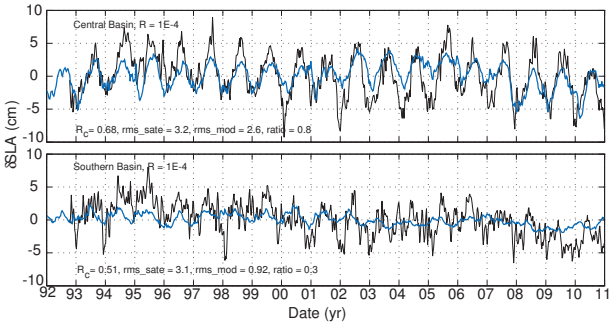

Figure 4.3: Time series of the relative sea level displacements between the rim and the inner PV contours in the two different transects over the central and the southern basins gyres of the CS. The black and blue lines indicate weekly time series of the sea level anomalies based on the satellite observation and the barotropic model prediction, respectively.

southern and central basins (considering a horizontal length scale as $50\,\mathrm{km}$), are $0.057;\ 0.027$, respectively. In both cases, the Burger number is less than 1, but the stratification is stronger in the southern basin. The observations show that the velocities in the lower layers are smaller than the velocities in upper layers, but in the same direction (see, Fig. 3.3). Therefore, the velocities are parallel, but decay with depth. This implies that, an equivalent barotropic (EB) model may be applicable in the southern basin.

We examined different e-folding scale (h_0) values in the central and the southern basins, to achieve the best agreement between satellite measurements and EB model. For the EB model, we used the same bottom drag coefficient as *Isachsen et al.* (2003) applied for the Nordic Seas and Arctic Ocean ($R = 5.0 \times 10^{-4}\,\mathrm{m\,s^{-1}}$). The best agreement between observation and EB model in the central basin occurs at $h_0 = 800\,\mathrm{m}$. Although, the correlation coefficient is same as the barotropic model, the amplitude remarkably is improved. Additionally, the ratio of the RMS of predicted SLA to the RMS of observed SLA for the central basin is increased from 0.8 to 1.1. In the southern basin, the EB model shows high accordance with observation at $h_0 = 500\,\mathrm{m}$. The correlation coefficient between observation and prediction is modified from 0.51 (barotropic model) to 0.58, also the amplitude is considerably improved. The RMS ratio enhancement from 0.3 to 0.7 shows that, despite the barotropic model, the EB model predictions are not extremely underestimate in the southern basin. Note, we used five times stronger drag coefficient in the equivalent model than the pure barotropic one. Although, the stronger drag coefficient decreases the amplitude, but $P(-H)$ is small when $H \gg h_0$, which reduces the drag coefficient and, maintains the amplitude. In some studies an augmentative constant has been introduced, to obviate the reducing effect of $P(-H)$ (see, *Krupitsky et al.* (1996); *Ivchenko et al.* (1999)). In line with *LaCasce and Isachsen* (2010), we did not apply that constant, and apparently, the performance of the model in terms of the amplitude is acceptable. In fact, the drag could be too weak, if the depth largely exceeds h_0. In such a configuration, the wind forcing is essentially unbalanced. Taking into account the best e-folding scale and maximum depth, the large depth condition ($H \gg h_0$) never fulfills in the CS. Therefore, the drag is not that weak in this problem. Additionally, the stronger drag coefficient makes the $i\omega$ less dominant and reduces its filtering effect. As one might expect, the EB model renders relatively better

performance in capturing of the high frequency signals. For more detailed discussions about the application of the EB model in the CS, see paper I.

4.2 Mass transport in the Stokes edge wave for constant arbitrary bottom slope

In this study we investigate the nonlinear mass transport in the Stokes surface edge wave in an unbounded ocean. This is done by applying an Eulerian description of motion, and expanding the solution in series after wave steepness as a small parameter. We derive analytical expressions for the vertically-averaged Lagrangian drift velocity induced by Stokes edge wave in a rotating and non-rotating ocean. This drift is composed of Stokes drift plus Eulerian velocity.

We derive analytical expressions for the total mean energy (E), and total dissipation rate (D), from linear wave solution. Following *Gaster* (1962) and transition from temporal damping to spatial damping, an expression for the spatial attenuation coefficient is obtained. It is shown that the non-rotating case can be recovered by setting $f = 0$, in the rotating expression. It was demonstrated by *Longuet-Higgins and Stewart* (1960) that the radiation stress (S) forcing would be $\frac{1}{2}(-\partial E/\partial y)$ for deep water waves and $\frac{3}{2}(-\partial E/\partial y)$ for shallow water waves in a non-rotating ocean for constant depth. For Stokes edge waves, the time rate of change of the total Lagrangian momentum flux in the wave direction is forced by the divergence of the total energy density $-\partial E/\partial y$, in both rotating and non-rotating cases.This value is mid-way between the deep and shallow water values. Since the particles move in planes parallel to the sloping bottom, there is a cross-wave velocity component. This transverse velocity contributes in wave energy, but does not appear in the radiation stress term. Hence, one would expect a relation that differs from that of *Longuet-Higgins and Stewart* (1960). Therefore, the wave energy in the entire trapped zone yields $\int_0^\infty S dx = E/\rho$. This is exactly same for the rotating and the non-rotating Stokes edge wave, demonstrating that it is not the rotation, but the sloping bottom that yields a value which is in between the deep and shallow water values of *Longuet-Higgins and Stewart* (1960).

For a reasonable value of wavelength ($\lambda = 1\,\mathrm{km}$), for wave traveling with the coast to the left ($\omega > 0$), the critical slope angle becomes $\beta^* = 89.9°$, which is very close to the vertical wall limit. Hence, in practice, our calculations are valid in the interval $0 < \beta < \pi/2$ for the chosen wavelength. In Fig. 4.4 we have displayed non-dimensional Eulerian velocity and non-dimensional Stokes drift for various values of the bottom slope for ($\lambda = 1\,\mathrm{km}$). The results show that for larger slope angles, the trapped zone is wider for non-dimensional Eulerian drift. The calculations show that the Stokes drift and the Eulerian current have their maximum values at the shore line. The spatial variation over the shelf for non-dimensional Stokes drift and Eulerian current is almost similar for small and moderate slope angles. But, at the shore line it mainly depends on the slope angle. The ratio between the mean Eulerian current and the Stokes drift at the the shore is

$$\frac{v_{E0}}{v_{S0}} = Rk\sin\beta\left[1+\frac{1}{2}\left(\frac{f\omega}{gk}\right)^2\right], \tag{4.1}$$

where, R is friction. Therefore, for wave motion in which the earth's rotation becomes important, we see that increasing values of the Coriolis parameter, increase the Eulerian currents for

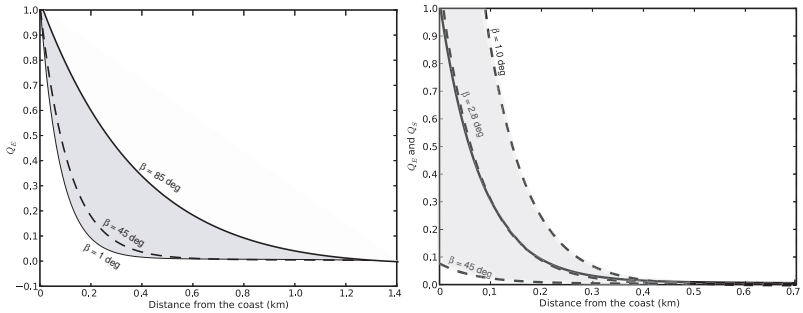

Figure 4.4: Non-dimensional Eulerian mean current Q_E (left) and non-dimensional Stokes drift current Q_S (right) for $\lambda = 1\,\mathrm{km}$.

a given bottom slope. For the wavelength considered here ($\lambda = 1\,\mathrm{km}$), the last term in the in the parenthesis is negligible. Therefore, the relative strength of the Eulerian current and the Stokes drift depends on friction and bottom slope. As the frictional influence should be of order unity, the slope angle plays vital role here. Hence, the relative importance of the mean Eulerian current to the Stokes drift can be expressed as $v_{E0}/v_{S0} \propto \sin\beta$. This demonstrate that for given wavelength, the Stokes drift tends to dominate the Eulerian current for small and moderate slope angles (see Fig. 4.4).

The theory developed here is valid for steeply sloping bottoms and our calculations for $\omega > 0$ are valid for all $\beta < \beta^*$. Such solutions may be convenient for comparison with experiments in wave tanks, where a steep slope may be advantageous. But, in natural environments beach slopes are mostly quite gentle. In order to relate our theoretical results to the natural environments, we consider the CS as a case study. In the southern basin of the CS the depth increases slowly from the coast over the continental shelf (see Fig. 3.1). As noted before, in such case the Stokes drift exceeds the mean Eulerian velocity. In this example, we take that the wave amplitude η_0 is $0.1\,\mathrm{m}$, the wavelength λ is $1\,\mathrm{km}$ and $f = 8.86 \times 10^{-5}\,\mathrm{s}^{-1}$. Furthermore, $\beta = 0.25^\circ$ is typical slope angle for the southern CS beach. By taking typical values for the linear friction coefficient ($K = 10^{-5}\,\mathrm{m\,s}^{-1}$), and eddy viscosity ($\nu = 10^{-3}\,\mathrm{m}^2\,\mathrm{s}^{-1}$), we obtain that $R = 10^2\,\mathrm{m}$ in this problem. For this est of parameters, we find $v_{E0} = 0.6\,\mathrm{cm\,s}^{-1}$ and $v_{S0} = 5.5\,\mathrm{cm\,s}^{-1}$ for the CS. We note that the Stokes drift is dominating component of transport and is comparable to traditional wind surge velocities. In the present study, the basis of the derivation of the fluxes is expressing the solutions as expansions in power series after the wave steepness as a small parameter. Hence, we must require that the second order Stokes drift must be considerably smaller than the linear velocity field. Consequently, the Stokes drift must be smaller than phase speed of the wave, which leads to $\eta_0 k < \sin\beta$. Here, we have $\eta_0 k = 6.28 \times 10^{-4}$, and $\sin\beta = 4.36 \times 10^{-3}$, which fulfills the condition quite well. Figure 4.5 shows phase speed ($c_p = \omega/k$) and Stokes drift velocity for the CS example. As it shown, for the chosen parameters, the Stokes drift is remarkably smaller than the phase speed, which indicates that the nonlinear theory is valid. For same configuration the Stokes drift velocity exceeds phase speed for waves with wave numbers larger than $k > 0.043\,\mathrm{m}^{-1}$, where the nonlinear theory is not valid. We note that different values of slope angle and wave amplitude can alter the Stokes drift. E.g. for larger bottom angles the Stokes drift velocity becomes smaller. Hence, for

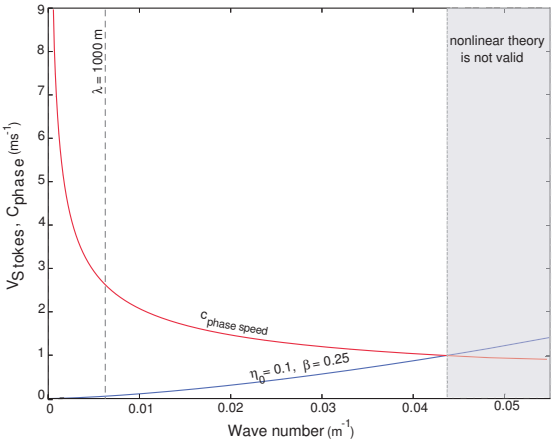

Figure 4.5: Dimensional Stokes velocity v_{S0} (blue line) and phase velocity c_p (red line) for Stokes edge waves for the southern Caspian beach; $\eta_0 = 0.1\,\mathrm{m}$, $\lambda = 1\,\mathrm{km}$, $f = 8.68 \times 10^{-5}\,\mathrm{s}^{-1}$ and $\beta = 0.25°$.

steeper bottom, the nonlinear theory is valid for even larger wave numbers. Conversely, wave amplitude plays significant role in increasing the Stokes drift velocity, which decreases wave number threshold for validity of the nonlinear theory.

Moreover, we consider two more locations; Slapton Beach (*Huntley and Bowen*, 1973), and Lake Michigan (*Donn and Ewing*, 1956), where we find short and long waves, respectively. In both cases the depth increases slowly. As we noted before, in such cases the Stokes drift is comparable to or exceeds the mean Eulerian velocity. For more detailed discussions about the Stokes edge wave-induced mass transport in aforementioned areas, see papers II and III.

4.3 Mass transport in internal coastal Kelvin waves

In the present study we have investigated the drift due to internal coastal Kelvin waves. We find the Stokes drift trapped to the coast within the Rossby radius of deformation. However, by integration in vertical, and application of proper boundary conditions, it is demonstrated that the associated Stokes volume flux for internal coastal Kelvin waves is zero. In line with this important result, the total mean Lagrangian transport attributes to only mean Eulerian transport. The mean Eulerian current for each mode is trapped to the coast within the Rossby radius of deformation, and that current is always positive (directed along the wave). Additionally, in a balanced flow the ratio of forcing from the wave field (through the radiation stress) and the restraint of bottom friction on the mean flow should be of order unity. The present approach yields the Stokes drift as function of depth, while the mean Eulerian current is determined as a depth average by integration from the bottom to the surface. This procedure masks the vertical variation of the Eulerian drift current, and makes comparisons with the Stokes drift at a certain depth difficult.

As an example for the Stokes drift in the internal coastal Kelvin waves, we consider the continental shelf break of the CS (see Fig. 3.4). In order to obtain the eigenvalues c_1, c_2, c_3

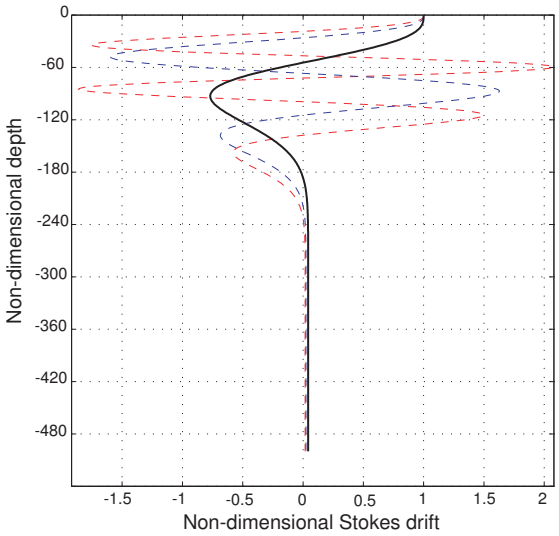

Figure 4.6: Non-dimensional Stokes drift for the first (dark line), second (blue dashed line), and third (red dashed line) baroclinic mode in the CS as function of non–dimensional depth.

etc., we must prescribe Brunt-Väisälä frequency in study area. Using measurements by *Ghaffari et al.* (2010) we find an expression for Brunt-Väisälä frequency, which is typical for winter condition in the south-western part. The eigenvalue problem is easily solved by a simple shooting procedure. We then obtain $c_1 = 1.21\,\mathrm{m\,s^{-1}}$. The next successive eigenvalues become $c_2 = 0.45\,\mathrm{m\,s^{-1}}$ and $c_3 = 0.28\,\mathrm{m\,s^{-1}}$ for the second and third baroclinic mode, respectively. The non-dimensional Stokes drift $\bar{u}_{Sn}/u_{0n}$ at the coast for first three successive baroclinic modes in the study area are shown in Fig. 4.6, where $u_{0n} \propto c_n \xi_{0n}^2$. Therefore, in dimensional form, wave amplitude and eigenvalue at each specific mode determine the Stokes drift value. We note that in the first baroclinic mode, the Stokes drift has its largest value at the coast, and reaches its largest negative value about $-80\,\mathrm{m}$, where the thermocline located and Brunt-Väisälä frequency has its maximum value (*Ghaffari et al.*, 2010). For fairly sharp thermocline, first mode mostly comprise a substantial portion of the total energy (*Phillips*, 1966). Hence, we particularly interested to the first mode, which we believe that contains majority of the energy fraction, considering almost sharp thermocline in the study area (Fig. 3.4). The isothermal contours fluctuation (Fig. 3.5) can be attributed to the first baroclinic mode of the internal Kelvin wave in the south-western part of the CS, since they both have almost the same period. Therefore, the measurements suggest a vertical amplitude of about $\xi_{01} = 40\,\mathrm{m}$ for the first baroclinic mode. This implies that the dimensional Stokes drift varies from $7\,\mathrm{cm\,s^{-1}}$ at surface to $-5\,\mathrm{cm\,s^{-1}}$ at the thermocline location. The negative and positive lobs of the Stokes drift depth profile fulfills the no-flux condition. However, the Eulerian flux is not zero, e.g. for first baroclinic mode, the Eulerian transport occurs within a narrow region of width $\sim 7\,\mathrm{km}$. Since the internal coastal Kelvin waves always propagate with the coast to the right (for $f > 0$), we conclude that there is a systematic contribution from such waves to the mean circulation in the CS. For more detailed discussions about the internal coastal Kelvin wave-induced mass transport in the study area, see

paper IV.

Chapter 5

Concluding remarks

This thesis discusses the topographic effect on wind-driven current variability as well as the mean currents due to topographically trapped waves. Through the individual papers, we investigate the wind-driven transport in regions with closed potential vorticity contours, and estimate the mean transport induced by trapped gravity waves such as the Stokes surface edge wave and the internal Kelvin wave. Such transports are interesting from a fluid dynamics point of view, but they also have practical implications. It is a fact that topographic changes in the ocean often are strongest close to the coasts or the shore line. Therefore topographically steered currents may advect effluents and pollution along coasts and beaches and thereby pose a threat to the coastal population. Furthermore, for small bottom sediments in suspension, this mean drift may contribute to beach erosion by relocating bottom material.

The mean drift velocity in progressive waves is not easy to observe using fixed point measurement. It is partly due to the nature of the Stokes drift, but also due to the small amplitudes which are easily masked by other dynamics, e.g. tidal and inertial currents. Lagrangian measurements, e.g. drifters, are needed to capture the mean wave-induced transport. On the other hand, a drifter also responds to the geophysical forcing by the wind, wind-waves, and the oceanic currents. It is therefore not straightforward to decompose the wave drift from the drifter motion. In this respect, the Caspian Sea as a tide-free, closed body of water seems a promising place for such experiments. This large lake can be regarded as prototype laboratory. During calm wind episodes, which are quite common in this region, the mean transport and drifter response may entirely be attributed to the remotely generated, transient waves. Here, a coupling of extensive numerical modeling with field observations would be quite profitable. Extracting the particle drift from the model output using a Lagrangian approach, and comparing it with Lagrangian observations would clearly improve our understanding of wave-driven currents.

Bibliography

Ardhuin, F., and A. D. Jenkins, On the interaction of surface waves and upper ocean turbulence, *J. Phys. Oceanogr.*, *36*, 551–557, 2006.

Blondeaux, P., M. Brocchini, and G. Vittori, Sea waves and mass transport on a sloping beach, *Proc. R. Soc. Lond.*, *458*, 2053–2082, 2002.

Blondeaux, P., G. Vittori, F. Bruschi, A.and Lalli, and V. Pesarino, Steady streaming and sediment transport at the bottom of sea waves, *J. Fluid Mech.*, *697*, 115–149, 2012.

Boehm, A. B., S. B. Grant, J. H. Kim, S. L. Mowbray, C. D. McGee, C. D. Clark, D. M. Foley, and D. E. Wellman, Decadal and shorter period variability of surf zone water quality at huntington beach, california, *Environ. Sci. Technol.*, *36*, 3885–3892, 2002a.

Boehm, A. B., B. F. Sanders, and C. D. Winant, Cross-shelf transport at huntington beach. implications for the fate of sewage discharged through an offshore ocean outfall, *Environ. Sci. Technol.*, *36*, 1899–1906, 2002b.

Bondarenko, A. L., *Currents of the Caspian Sea and formation of salinity of the waters of the north part of the Caspian Sea*, Nauka, Moscow, Russia, 1993, in Russian.

Bondarenko, A. L., Natural investigation of the Caspian Sea currents, *Russian Academy of Science, Water Problems Institute*, 1994.

Bowen, A. J., and D. L. Inman, Rip currents: 2. laboratory and field observations, *J. Geophys. Res.*, *74*, 5479–5490, 1969.

Bowen, A. J., and D. L. Inman, Edge waves and crescentic bars, *J. Geophys. Res.*, *76*, 8662–8671, 1971.

Charney, J. G., and A. Eliassen, A numerical method for predicting the perturbations of the middle latitude westerlies, *Tellus*, *1*, 38–54, 1949.

Donn, W. L., and M. Ewing, Stokes' edge waves in lake michigan, *Science*, *124*, 1238–1242, 1956.

Dore, B. D., Wave-induced vorticity in free-surface boundary layers: application to mass transport in edge waves, *J. Fluid Mech.*, *70*, 257–266, 1975.

Eckart, C., Surface waves in water of variable depth, *Wave Rept. 100, S.I.O. Ref. 51-12, 99 pp*, Scripps Institution of Oceanography, 1951.

Evans, D. V., Edge waves over a sloping beach, *Q. J. Mech. Appl. Maths.*, *42*, 131–142, 1989.

Gaster, M., A note on the relation between temporally-increasing and spatially-increasing disturbances in hydrodynamic stability, *J. Fluid Mech.*, *14*, 222–224, 1962.

Ghaffari, P., and V. Chegini, Acoustic doppler current profiler observations in the southern Caspian Sea: shelf currents and flow field off Feridoonkenar bay, iran, *Ocean Sci.*, *6*, 737–748, 2010.

Ghaffari, P., and J. E. H. Weber, Mass transport in the Stokes edge wave for constant arbitrary bottom slope in a rotating ocean, *J. Phys. Oceanogr.*, doi:10.1175/JPO-D-13-0171.1, in press, 2014.

Ghaffari, P., H. A. Lahijani, and J. Azizpour, Snapshot observation of the physical structure and stratification in deep-water of the south Caspian Sea (western part), *Ocean Sci.*, *6*, 877–885, 2010.

Ghaffari, P., P. E. Isachsen, and J. H. LaCasce, Topographic effects on current variability in the Caspian Sea, *J. Geophys. Res. Oceans*, pp. 1–10, 2013.

Gill, A. E., and A. J. Clarke, Wind-induced upwelling, coastal currents, and sea-level changes, *Deep-Sea Res.*, *21*, 325–345, 1974.

Gille, S. T., E. J. Metzger, and R. Tokmakian, Seafloor topography and ocean circulation, *Oceanography*, *17*, 47–54, 2004.

Gordon, A. L., E. Molinelli, and T. Baker, Large-scale relative dynamic topography of the Southern Ocean, *J. Geophys. Res.*, *83*, 3023–3032, 1978.

Greenspan, H. P., *The Theory of Rotating Fluids*, Breukelen Press, Brookline, MA, 1990.

Hasselmann, K., An ocean model for climate variability studies, *Prog. Oceanog.*, *11*, 69–92, 1982.

Howd, P. A., A. J. Bowen, and R. A. Holman, Edge waves in the presence of strong longshore currents, *J. Geophys. Res.*, *97*, 11,357–11,371, 1992.

Huntley, D. A., and A. J. Bowen, Field observations of edge waves, *Nature*, *243*, 160–162, 1973.

Isachsen, P. E., J. H. LaCasce, C. Mauritzen, and S. Häkkinen, Wind-driven variability of the large-scale recirculating flow in the Nordic Seas and Arctic Ocean, *J. Phys. Oceanog.*, *33*, 2534–2550, 2003.

Ivchenko, V., A. Krupitsky, V. Kamenkovich, and N. Wells, Modeling the Antarctic Circumpolar Current: A comparison of fram and equivalent barotropic model results, *J. Mar. Res.*, *57*, 29–45, 1999.

Jenkins, A. D., The use of a wave prediction model for driving a near-surface current model, *Deutsche Hydrografische Zeitschrift*, *42*, 133–149, 1989.

Kamenkovich, V. M., On the theory of the Antarctic Circumpolar Current, *Trudy Instituta Okeanologii*, *56*, 245–306, 1962.

Killworth, P. D., An equivatent-barotropic modein the fine resolution Antarctic model, *J. Phys. Oceanog.*, *22*, 1379–1387, 1992.

Kosarev, A. N., *Gidrologiya Kaspiiskogo I Aralskogo morey*, Moscow University Press, Moscow, USSR, 1975.

Krupitsky, A., V. M. Kamenkovich, N. Naik, and M. A. Cane, A linear equivalent barotropic model of the Antarctic Circumpolar Current with realistic coastlines and bottom topography, *J. Phys. Oceanogr.*, *26*, 1803–1824, 1996.

Kurkin, A., and E. Pelinovsky, Shallow-water edge waves above an inclined bottom slowly varied in along-shore direction, *Europ. J. Mech. B/Fluids*, *22*, 305–316, 2003.

LaCasce, J., and P. E. Isachsen, The linear models of the ACC, *Prog. Oceanog.*, *84*, 139–157, 2010.

Lamb, S. H., *Hydrodynamics*, sixth edition ed., Cambridge at the University Press, 1932.

LeBlond, P. H., and L. A. Mysak, *Waves in the ocean*, Elsevier Oceanog. Series, 20. Elsevier, Amsterdam, 1978.

Leichter, J. J., S. R. Wing, S. L. Miller, and M. W. Denny, Pulsed delivery of subthermocline water to Conch Reef (Florida keys) by internal tidal bores, *Limnolog. Oceanog.*, *41*, 1490–1501, 1996, n/a.

Lighthill, M. J., Dynamic response of the Indian Ocean to onset of the soutsouth monsoon, *Phil. Trans. R. Soc. London A*, *265*, 45–92, 1969.

Longuet-Higgins, M. S., Mass transport in water waves, *Phil. Trans. R. Soc. Lond.*, *A245*, 535–581, 1953.

Longuet-Higgins, M. S., and R. W. Stewart, Changes in the form of short gravity waves on long waves and tidal currents, *J. Fluid Mech.*, *8*, 565–583, 1960.

Marshall, D., Topographic steering of the Antarctic Circumpolar Current, *J. Phys. Oceanogr.*, *25*, 1636–1650, 1995.

McWilliams, J. C., P. P. Sullivan, and C. Moeng, Langmuir turbulence in the ocean, *J. Fluid Mech.*, *334*, 1–30 M3 – 10.1017/S0022112096004,375, 1997.

Mei, C. C., A note on the averaged momentum balance in two-dimensional water waves, *J. Mar. Res.*, *31*, 97–104, 1973.

Mok, K. M., and H. Yeh, On mass transport of progressive edge waves, *Phys. Fluids*, *11*, 2906–2924, 1999.

Nielsen, P., *Coastal Bottom Boundary Layers and Sediment Transport. Advanced Series on Ocean Engineering*, vol. 4, World Scientific, Singapore, 1992.

Nøst, E., Calculating tidal current profiles from vertically integrated models near the critical latitude in the Barents Sea, *J. Geophys. Res.*, *99*, 7885–7901, 1994.

Phillips, O. M., *The Dynamics of the Upper Ocean*, Cambridge University Press, New York, 1966.

Reid, R. O., Effects of coriolis force on edge waves. (i) investigation of the normal modes, *J. Mar. Res.*, *16*, 109–144., 1958.

Röhrs, J., K. H. Christensen, L. R. Hole, G. Broström, M. Drivdal, and S. Sundby, Observation-based evaluation of surface wave effects on currents and trajectory forecasts, *Ocean Dynamics*, *62*, 1519–1533, 2012.

Sonu, C., S. Murray, U. S. O. of Naval Research, L. S. University, Agricultural, and M. C. C. S. Institute, *Collective Movement of Sediment in Littoral Environment*, Coastal Studies Institute, Louisiana State University, 1969.

Stokes, G. G., Report on recent researches in hydrodynamics, *Rep. 16th Brit. Assoc. Adv. Sci.*, pp. 1–20. (See also Papers, vol. 1, pp. 157–187. Cambridge University Press, 1880), 1846.

Stokes, G. G., On the theory of oscillatory waves, *Trans. Cam. Phil. Soc.*, *8*, 441–455, 1847.

Sur, H. I., E. Özsoy, and R. Ibrayev, Chapter 16 satellite-derived flow characteristics of the Caspian Sea, in *Satellites, oceanograghy and society*, edited by D. Halpern, vol. 63 of *Elsevier Oceanography Series*, pp. 289–297, Elsevier, 2000.

Terziev, F. S., A. Kosarev, and A. A. Kerimov (Eds.), *The Seas of the USSR. Hydrometeorology and Hydrochemistry of the Seas, Vol. VI: The Caspian Sea, Issue 1: Hydrometeorological Conditions*, Gidrometeoizdat, St. Petersburg, Russia, 1992.

Trukhchev, D., A. Kosarev, D. Ivanova, and V. Tuzhilkin, Numerical analysis of the general circulation in the Caspian Sea, *Comptes Rendus de l'Academie Bulgare des Sciences, Sofia*, *48*, 35—38, 1995.

Ursell, F., Edge waves on a sloping beach, *Proc. R. Soc. London.*, *A214*, 79–97, 1952.

Vittori, G., and P. Blondeaux, Mass transport under sea waves propagating over a rippled bed, *J. Fluid Mech.*, *314*, 247–265, 1996.

Weber, J. E. H., and M. Drivdal, Radiation stress and mean drift in continental shelf waves, *Cont. Shelf Res.*, *35*, 108–116, 2012.

Weber, J. E. H., and P. Ghaffari, Mass transport in the Stokes edge wave, *J. Mar. Res.*, *67*, 213–224, 2009.

Weber, J. E. H., and P. Ghaffari, Mass transport in internal coastal Kelvin waves, *Europ. J. Mech. B/Fluids*, in press, 2014.

Weber, J. E. H., and A. Melsom, Transient ocean currents induced by wind and growing waves, *J. Phys. Oceanogr.*, *23*, 193–206, 1993.

Weber, J. E. H., and E. Støylen, Mean drift velocity in the Stokes interfacial edge wave, *J. Geophys. Res.*, *116*, C04,002, 2011.

Weber, J. E. H., G. Broström, and Ø. Saetra, Eulerian versus lagrangian approaches to the wave-induced transport in the upper ocean, *J. Phys. Oceanogr.*, *36*, 2106–2117, 2006.

Williams, R. B., and C. H. Gibson, Direct measurements of turbulence in the Pacific Equatorial Undercurrent, *J. Phys. Oceanogr.*, *4*, 104–108, 1974.

Zaker, N. H., P. Ghaffari, and S. Jamshidi, Physical study of the southern coastal waters of the Caspian Sea, off Babolsar, Mazandaran in Iran, *J . Coast. Res.*, *SI 50*, 564–569, 2007.

Zaker, N. H., P. Ghaffari, S. Jamshidi, and M. Nouranian, Currents on the southern continental shelf of the Caspian Sea off Babolsar, Mazandaran in Iran, *J. Coas. Res., SI 64*, pp. 1989–1997, 2011.

I

JOURNAL OF GEOPHYSICAL RESEARCH: OCEANS, VOL. 118, 1–10, doi:10.1002/2013JC009128, 2013

Topographic effects on current variability in the Caspian Sea

P. Ghaffari,[1] P. E. Isachsen,[2] and J. H. LaCasce[1]

Received 22 May 2013; revised 22 October 2013; accepted 28 November 2013.

[1] Satellite-derived surface height fields reveal that variability in the central and southern basins of the Caspian Sea is correlated with topography. Consistently, empirical orthogonal functions from current meter data from the southern basin are aligned with the isobaths. In addition, the gravest mode, which accounts for over 80% of the variance, has an equivalent barotropic structure in the vertical. To what extent this variability can be modeled using a linear analytical model is examined. The latter assumes equivalent barotropic flow aligned with the geostrophic contours, which in turn are dominated by the topography. With ECMWF winds and ETOPO2 topography, the model yields surface height deviations which are significantly correlated with satellite-derived estimates on seasonal and longer time scales in the central basin. The model is somewhat less successful in the southern basin, where the stratification is stronger. Nevertheless, the results are encouraging, given the extreme simplicity of the model.

Citation: Ghaffari, P., P. E. Isachsen, and J. H. LaCasce (2013), Topographic effects on current variability in the Caspian Sea, *J. Geophys. Res. Oceans*, *118*, doi:10.1002/2013JC009128.

1. Introduction

[2] The Caspian Sea (CS) is the largest inland water body of the world in both area (379,000 km^2) and volume (78,000 km^3). The CS is located between 36°N and 47°N in a region with complex bathymetric features [*Ismailova*, 2004]. There are three distinguished basins: the northern, central, and southern basins. The southern and the central basins have maximum depths of 1025 and 788 m, respectively, and a sill with a maximum depth of approximately 170 m separates two [*Peeters et al*., 2000]. The northern basin is a shallow extension with maximum depth of 20 m. The CS is classified as a deep inland sea, due to its thermohaline structure and water circulation [*Lebedev and Kostianoy*, 2006].

[3] The CS is enclosed and tides are fairly weak. Density-driven and wave-driven flows do occur [*Bondarenko*, 1993; *Ghaffari and Chegini*, 2010; *Ibrayev et al*., 2010; *Terziev et al*., 1992], but the currents are primarily forced by the winds. Due to the strongly variable topography, the resulting flows are often spatially and temporally variable, with an active mesoscale eddy field [*Terziev et al*., 1992; *Trukhchev et al*., 1995].

[4] Diverse observations with floats and hydrography, and the results of numerical models simple hydrodynamic interpretations [*Bondarenko*, 1993; *Terziev et al*., 1992], suggest that the circulation in all three basins is predominantly cyclonic. The circulation is thus associated with a predominantly southward flow along the western coast and northward flow along the eastern coast. Recent observations in the shallow coastal area (~100 m depth or less) likewise indicate cyclonic flow, but also reveal exceptions. In particular, the flow near the eastern coast has been observed to reverse episodically [*Ibrayev et al*., 2010], as has the flow near the southern boundary [*Ghaffari and Chegini*, 2010]. Further information about the hydrographic structure and general circulation of the CS is given by *Kostianoy* [2005].

[5] Although the region has been studied extensively, a comprehensive picture of the circulation is lacking. In particular, we do not have a first-order model explaining the response to wind forcing and, more generally, an explanation for the predominantly cyclonic flow. The goal of the present study is to propose such a model.

[6] Our model is relevant in regions where the ambient potential vorticity contours (PV), or geostrophic contours, are closed. For unstratified regions these are the f/H contours, where f is the Coriolis parameter and H is the water depth. Such models have been used before to investigate wind-driven variability [see *Kamenkovich*, 1962; *Hasselmann*, 1982; *Isachsen et al*., 2003]. The main assumption of such models is that the primary component of the flow is parallel to the f/H contours. The flow is then forced by convergence or divergence in the surface Ekman layer and balanced by divergence or convergence in the frictional Ekman layer at the bottom (details are given below).

[7] As shown in Figure 1, the f/H contours in the Caspian Sea are indeed closed in both the central and southern basins. We will, therefore, investigate the use of such a model here. However, as there is significant stratification in the CS, it is not certain that a barotropic model is sufficient.

[1]Department of Geosciences, University of Oslo, Oslo, Norway.
[2]Research and Development Department, Norwegian Meteorological Institute, Oslo, Norway.

Corresponding author: P. Ghaffari, Department of Geosciences, University of Oslo, Oslo 0315, Norway. (peygham.ghaffari@geo.uio.no)

2169-9275/13/10.1002/2013JC009128

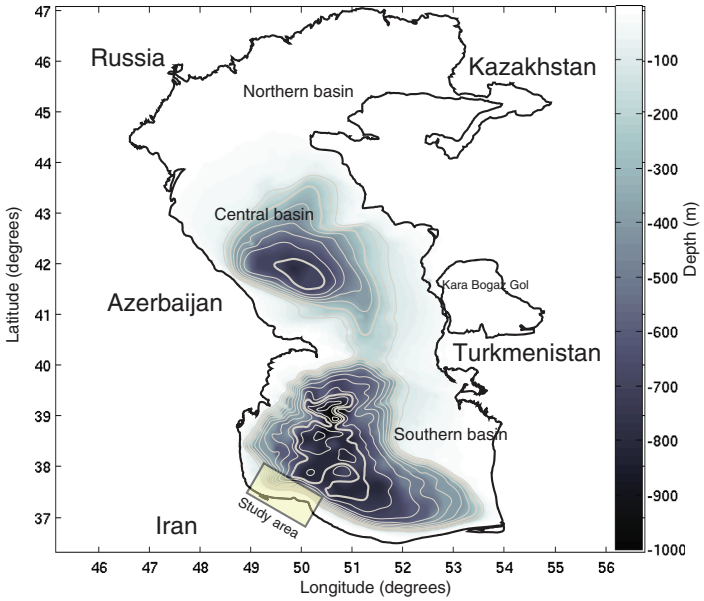

Figure 1. The bathymetric field of the CS (shown as gray shading), and potential vorticity field (contours) in the Caspian Sea. While the *f*/*H* contours have semicircular shapes in the central basin, the southern basin encompass relatively complicated feature.

So we extend the existing model to allow for vertical shear. As seen below, observations from the southern basin show that current fluctuations are approximately equivalent barotropic, and taking that into account is straightforward.

[8] The manuscript is organized as follows: relevant observations are described in section 2. In section 3, the equivalent barotropic model is derived. In section 4, the model solutions are presented and discussed and concluding remarks are given in section 5.

2. Observations

2.1. Satellite Observations

[9] Satellite observations provide the most comprehensive information about basin-scale variability in the sea. Weekly updated gridded maps of sea level anomalies (SLA) for the region and covering the period January 1992 to December 2011 are available (online at http://www.aviso.oceanobs.com). We used these fields to conduct an EOF analysis of the variability.

[10] The leading EOF, which accounts for 92% of the total variance, is remarkably similar to the *f*/*H* field in the central basin (Figure 2). This implies the sea surface is oscillating coherently across the basin. A similar result was found in the Norwegian, Lofoten, and Greenland basins by *Isachsen et al*. [2003].

[11] The response in the southern basin is less clear. The first mode does have a positive lobe that approximately traces out the *f*/*H* contours in the western portion of the basin, but the other lobes do not bear an obvious relation to

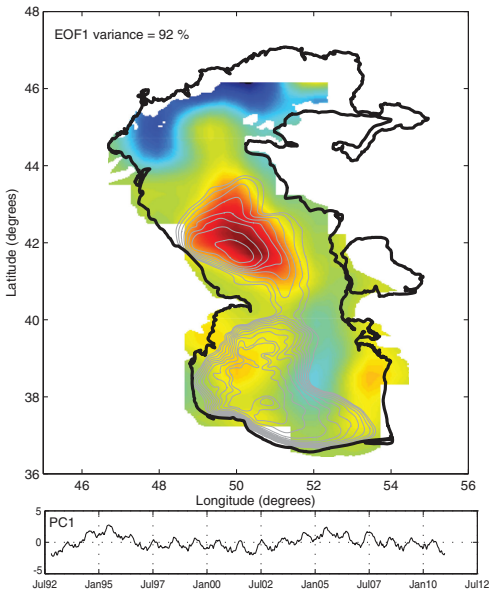

Figure 2. Principal component analysis of sea level anomalies (SLA) for the CS. (top) Leading EOF mode and *f*/*H* contours, and (bottom) associated PC time series, which accounts for 92% of the total variance in the field.

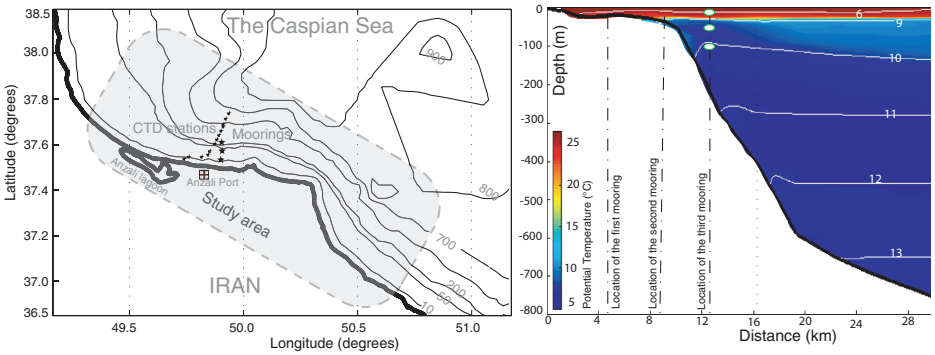

Figure 3. (left) The study area and the location of three moorings along the Iranian coast in the southwestern part of the southern basin (shown with stars). (right) Summer structures of the potential temperature, and the potential density isolines across the water column in the study area. The first two moorings are located over the continental shelf, and the third mooring is located on the continental slope.

the contours. EOF1 also exhibits distinct variability in the north-west region. Here the depth is 5–6 m and the flow moreover is heavily influenced by the Volga River.

[12] The remaining EOFs account for only 8% of the variance. These structures (not shown) are dominated by higher-wave number features that give little dynamical insight. So we will focus on the first EOF hereafter.

2.2. Current Meter Observations

[13] Three current meter moorings were deployed in a line perpendicular to the coastline off the south-western shelf of the CS, from November 2004 to early May 2005 (Figure 3). The moorings were located over the 20, 50, and 230 m isobaths at (37.505°N; 49.865°E), (37.531°N; 49.866°E), (37.553°N; 49.864°E), respectively.

[14] Recording Current Meters (RCM 9) were deployed near the surface, at middepths (for the 230 m mooring), and near the bottom, to provide measurements throughout the water column. The sampling frequency was 3 cph, but the analysis presented here is based on daily averaged velocities.

[15] Figure 4 shows the variance ellipses for the daily averaged currents for the three moorings. These have high eccentricities and the principal axes of the variability are closely aligned with the f/H contours, at all three moorings.

[16] The alignment and magnitude of the ellipses suggests the currents are fairly barotropic. To quantify this, we calculated the fraction of energy in the barotropic mode:

$$R = H\langle\overline{u}^2\rangle \Big/ \left[H\langle\overline{u}^2\rangle + \left\langle \sum_{n=1}^{N} (u')^2 dz \right\rangle\right], \qquad (1)$$

where N is the total number of the depth layers, $\overline{u}$ and u' are depth-averaged and depth-varying velocities, respectively. The angle brackets in (1) are time averages and H is the depth at the mooring. The depth-averaged velocity accounts for 92%, 79%, and 83% of the total variance in the moorings from the south to the north, respectively. This is consistent with previous results which suggested the flow field in the eastern part of the southern basin is nearly barotropic [*Ghaffari and Chegini*, 2010; *Zaker et al*., 2011].

[17] The deepest mooring has current meters at 3.5, 65, and 112 m. Thus, the upper two are in the seasonal thermocline (which spans the upper ~30 m in summer) and the lower one is well below it (Figure 3, right). The very high frequency fluctuations are not well correlated between the upper two and the lower one. But the squared coherences between the three time series are 0.6–0.8 at periods longer than 3 days. So the low frequency fluctuations have a reasonably large vertical coherence. As this mooring yields the best information about the flow in the basin interior, we use its currents for the subsequent analysis.

[18] The velocity ellipses suggest that the velocities at the deepest current meter at the third mooring are weaker than at the surface instruments, but also aligned (or counter-aligned) with them (Figure 4). To examine the vertical

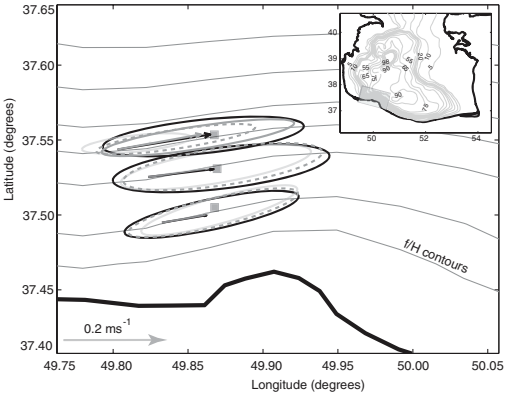

Figure 4. The current ellipses for surface (black line), bottom (light gray line) currents, and depth-averaged currents (dashed line). The dark gray ellipse in the third mooring represents middepth observation.

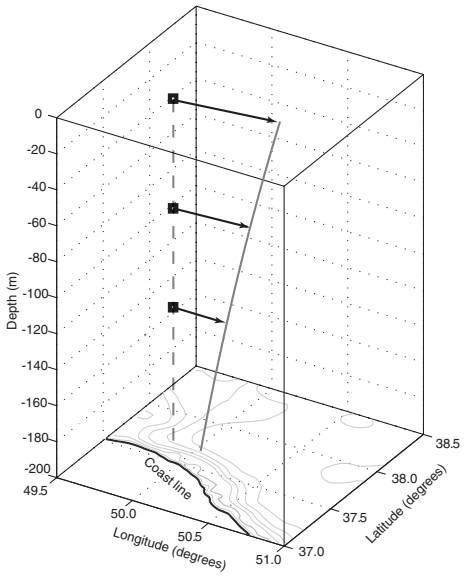

Figure 5. EOF1 for the currents at the deepest mooring in the southern basin. The arrows are from the EOF, at the depths corresponding to the current records. The topographic contours are indicated at the bottom, and an exponential function with an e-folding scale of 350 m is shown for comparison.

structure, we calculated complex EOFs for the three instruments [*Kaihatu et al*., 1998]. The first mode, which accounts for over 80% of the variance, is shown in Figure 5. This mode has the largest velocities at the surface and decays with depth, but the velocities are approximately parallel throughout the water column. So the velocities are approximately equivalent barotropic (EB). The e-folding scale, determined by nonlinear least squares, is about 350 m. The velocities are also aligned with the topography, consistent with the conclusions from the satellite data that variability is so-aligned.

[19] Of course stratification can cause current fluctuations, as those observed here, to decay with depth. Figure 3 (right) shows the potential density and temperature structures in summer (2008), along a transect extending from the coast toward the offshore region, in the study area. It reveals a strong seasonal thermocline located at ∼30 m depth, which is a typical seasonal thermocline depth in summer for almost whole basin [see *Kostianoy*, 2005]. *Ghaffari et al*. [2010] using hydrographic data (the same transect) showed that during the unprecedented severe winter (2008), the seasonal thermocline reached almost 100 m, where the water mass was still stratified. In fact, the CS has low salinity and the density stratification largely determined by temperature [*Terziev et al*., 1992]. Therefore, the density stratification mimics the temperature structure, i.e., the stratification is weaker but does not vanish in winter [*Kosarev*, 1975]. Figure 6 provides a large-scale picture of the stratification in the CS. Basin-wide potential density profiles reveal that the southern basin is more stratified than the central basin. In the southern basin, the surface densities are significantly less, producing larger near-surface gradients. Correspondingly, estimates of the Burger number, $Bu=\left(\frac{L_d}{L}\right)^2$, where L_d is the internal deformation radius and L is the scale of motion, are 0.057 and 0.027 for the southern and central basins, respectively (assuming a length scale as 50 km).

[20] So both current meter observations and hydrography suggest that the vertical stratification may be important, at

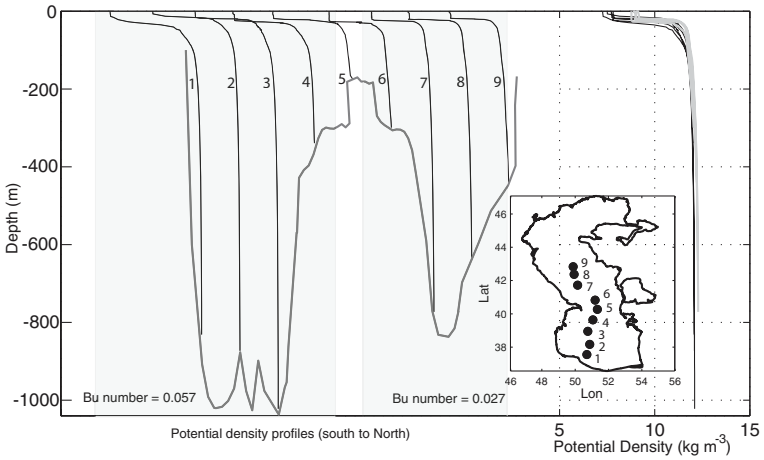

Figure 6. The potential density profiles in the central (gray lines) and southern (black lines) basins. The data were collected during the cruise on the CS (organized and conducted by the International Atomic Energy Agency) in September 1995 [*IAEA*, 1996]. (left) Vertical distributions of the potential density in the southern and central basins. (right) Overlay of the potential density profiles.

least in the southern basin. An equivalent barotropic description of currents seems appropriate, and a simplified model of wind-driven variability should thus assume EB currents. Having such depth-decaying currents is significant because topography will then exert a weaker influence than in a purely barotropic flow. EB models have been studied previously in the context of the Southern Ocean [*Ivchenko et al*., 1999; *Krupitsky et al*., 1996; *LaCasce and Isachsen*, 2010]. Below, we develop such a model in the context of closed-PV contours.

3. Theoretical Model

[21] The dynamics of flows with closed-PV contours differ from those with blocked contours. With blocked contours, forcing is required to support a steady circulation, as with the Sverdrup circulation. With closed contours, steady flows parallel to the PV contours can exist in the absence of forcing and dissipation [*Kamenkovich*, 1962; *Killworth,* 1992; *Hasselmann*, 1982; *Greenspan*, 1990; *Young*, 1981]. Such flows can be very strong and can be excited by wind forcing.

[22] *Isachsen et al*. [2003] derived a linear, barotropic model to study such flows. In the model (described below), an imbalance between the net transport in the surface and bottom Ekman layers results in a change in the geostrophic circulation within the closed contour region. The model was used to study wind-driven fluctuations in the Nordic Seas and was reasonably successful at reproducing variability observed from satellite and in a GCM. The success of such a model at high latitudes is aided by having relatively weak stratification. Whether such a model could work at lower latitudes, as in the Caspian Sea, remains to be seen.

[23] As the current fluctuations in the Caspian have an approximately EB structure, we recast the barotropic solution of *Isachsen et al*. [2003] for an EB flow. This involves mostly slight modifications, and the barotropic solution is recovered as a limiting case.

[24] As noted, the variables (e.g., pressure and velocity) vary with depth, but the direction of flow does not. So we can write

$$\boldsymbol{u}(x,y,z,t)=\boldsymbol{u}_s(x,y,t)P(z), \tag{2}$$

and

$$p(x,y,z,t)=p_s(x,y,t)P(z), \tag{3}$$

where $\boldsymbol{u}$ and p are the horizontal velocity vector and pressure, $\boldsymbol{u}_s$ and p_s are the corresponding surface values, and $P(z)$ is a vertical structure function. Following *Isachsen et al*. [2003], we assume a linear bottom drag, so that the bottom stress is:

$$\boldsymbol{\tau}_b=R\boldsymbol{u}(-H)=r_e\boldsymbol{u}_s, \tag{4}$$

where R is the bottom friction coefficient, $H(x,y)$ is depth, and $r_e=RP(-H)$ is a modified drag coefficient. Similar equations were derived previously by *Krupitsky et al*. [1996] and *LaCasce and Isachsen* [2010]. Substituting these into the linear horizontal momentum equation and integrating over the fluid depth yields:

$$\frac{\partial \boldsymbol{u}_s}{\partial t}+f\boldsymbol{k}\times\boldsymbol{u}_s=-g\nabla\eta+\left(\frac{\boldsymbol{\tau}_s}{\rho_0 F}-\frac{r_e\boldsymbol{u}_s}{F}\right). \tag{5}$$

where ρ_0 is a constant density, g the acceleration due to gravity, and $\boldsymbol{k}$ is the unit vector in the vertical direction. Furthermore, $\boldsymbol{\tau}_s$ is the surface stress vector, η is the sea surface height, and $F(x,y)$ is the vertical integral of the profile function:

$$F\equiv\int_{-H}^{0}P(z)dz. \tag{6}$$

[25] Substituting (2) into the continuity equation and integrating vertically yields:

$$\frac{\partial}{\partial x}(Fu_s)+\frac{\partial}{\partial y}(Fv_s)=0, \tag{7}$$

where u_s and v_s are eastward and northward velocity components. Thus, we may define a transport stream function as:

$$Fu_s=-\psi_y,\quad Fv_s=\psi_x. \tag{8}$$

[26] Taking the curl of (5) and using (8), we obtain the equivalent barotropic potential vorticity equation:

$$\frac{\partial}{\partial t}\nabla\times\boldsymbol{u}_s+J\left(\psi,\frac{f}{F}\right)=\nabla\times\frac{\boldsymbol{\tau}_s}{\rho_0 F}-\nabla\times\frac{r_e\boldsymbol{u}_s}{F}, \tag{9}$$

where the Jacobian term $J(\psi,f/F)=F\boldsymbol{u}_s\cdot\nabla f/F$ is the advection of PV by the flow. According to (9), a steady flow must be parallel to the f/F contours in the absence of forcing. These are the geostrophic contours in the EB model.

[27] As in *Krupitsky et al*. [1996], *Ivchenko et al*. [1999], and *LaCasce and Isachsen* [2010], we take $P(z)$ to be an exponential function

$$P(z)=\exp\left(\frac{z}{h_0}\right), \tag{10}$$

so that:

$$F=h_0\left[1-\exp\left(-\frac{H}{h_0}\right)\right]. \tag{11}$$

[28] We see that F, and hence the PV contours, are affected by vertical shear. For strongly sheared flows, i.e., for $h_0 \ll H$, F is approximately constant and the PV gradient is dominated by planetary beta. For deeper currents, i.e., for $h_0 \gg H$, $F \to H$ and the barotropic model is recovered. So the PV contours are intermediate between latitude lines and f/H contours, depending on the e-folding scale. Note too that the shear affects the effective bottom drag, as the latter is proportional to the bottom velocity. In deeper waters, where the depth is much greater than the e-folding scale, the drag is weak.

[29] The solution then follows that of *Isachsen et al*. [2003]. Assuming the forcing and friction are weak, and that the variations occur on long times scales, the dominant balance in (9) is:

$$J\left(\psi,\frac{f}{F}\right)=0. \tag{12}$$

[30] This implies that the first-order flow follows the f/F contours (which we assume are closed). The model thus filters out, for example, topographic waves, which entail cross-contour motion. So:

$$\psi=G\left(\frac{f}{F}\right), \tag{13}$$

where G is some function. The surface velocity is then given by:

$$\boldsymbol{u}_s=\frac{1}{F}\boldsymbol{k}\times\nabla G=\frac{1}{F}G'\boldsymbol{k}\times\nabla\left(\frac{f}{F}\right), \tag{14}$$

where G' is the derivative of G with respect to its argument, f/F.

[31] To determines G, we integrate equation (9) over a region bounded by an f/F contour. This eliminates the Jacobian term, after invoking the continuity equation, and yields:

$$\frac{\partial}{\partial t}\oint\boldsymbol{u}_s\cdot d\boldsymbol{l}=\oint\frac{\boldsymbol{\tau}_s}{\rho_0 F}\cdot d\boldsymbol{l}-\oint\frac{r_e\boldsymbol{u}_s}{F}\cdot d\boldsymbol{l}, \tag{15}$$

after applying Stokes' theorem. The first term on the RHS is the net transport into the surface Ekman layer and the last is the net transport in the bottom layer. An imbalance between these two results in a change in the circulation around the contour.

[32] We solve (15) by Fourier transforming the variables in time:

$$\boldsymbol{\tau}_s(x,y,t)=\sum_\omega\tilde{\boldsymbol{\tau}}_s(x,y,\omega)e^{i\omega t},\quad \boldsymbol{u}_s(x,y,t)=\sum_\omega\tilde{\boldsymbol{u}}_s(x,y,\omega)e^{i\omega t}.$$

[33] With this, (15) is:

$$\oint\left(i\omega+\frac{r_e}{F}\right)\tilde{\boldsymbol{u}}_s\cdot d\boldsymbol{l}=\oint\frac{\tilde{\boldsymbol{\tau}}_s}{\rho_0 F}\cdot d\boldsymbol{l}. \tag{16}$$

[34] The surface circulation depends on the bottom friction and the forcing frequency. At low frequencies ($\omega \ll r_e/F$), the circulation is in phase with the winds and has an amplitude which is inversely proportional to the modified bottom friction coefficient. At high frequencies, the circulation lags the wind by 90° and is independent of friction.

[35] Finally, inserting (14) into (16) gives:

$$G'=\frac{\oint\tilde{\boldsymbol{\tau}}_s/(\rho_0 F)\cdot d\boldsymbol{l}}{\oint(i\omega/F+r_e/F^2)\nabla(f/F)\cdot\hat{\boldsymbol{n}}dl}, \tag{17}$$

which is the EB equivalent to equation (8) in *Isachsen et al*. [2003]. They also discussed the equivalent barotropic model, but neglected that baroclinicity alters the PV contours. Assuming the flow is zero outside the region of closed contours, (14) can be integrated sequentially inward, yielding G and hence the stream function (applying the inverse Fourier transform). Furthermore, since the stream function is proportional to the surface pressure, i.e., $G=F(g/f)\eta$ the result can also be used to find sea surface height deviations between the inner and outer contours.

4. Results

[36] First, we compare the model prediction against sea level anomaly (SLA) measurements from the satellite. To do this, we estimated time series of SLA differences across both the central and southern basins, between an "inner" f/F contour in the deep basin and an "outer" contour near land. This SLA difference is proportional to the geostrophic transport between the two contours. The satellite-based estimate was calculated as the difference between SLA averaged over the two contours while the model estimate was calculated by integrating $\eta'=f/(gF)G'$ over a set of closely spaced contours between the inner and outer ones.

[37] The 0.125° × 0.125°-resolution European Centre for Medium-Range Weather Forecasts (ECMWF) operational analysis (available online at http://www.ecmwf.int) was used as wind forcing for the model. Topographic data were obtained from the ETOPO2 0°2′ × 0°2′ data set (available at http://www.ngdc.noaa.gov). The raw topographic data were smoothed to ∼10 km, a scale which is comparable to the internal deformation radius here [see also *Isachsen et al*., 2003; *LaCasce*, 2000; *Krupitsky et al*., 1996].

[38] The model's free parameters are the bottom friction coefficient R and the e-folding scale of the vertical shear, h_0. We set the bottom friction coefficient, $R=5.0\times10^{-4}$ m s^{-1}, following *Gill* [1982] and *Isachsen et al*. [2003]. We tested a range of values for h_0 for both basins.

4.1. Central Basin

[39] To do this, we calculated the correlation between the observed and modeled sea level differences, between an inner and an outer f/F contour, as a function of h_0; the result for the central basin is shown in Figure 7. The correlations are low at small values, confirming that topography is important for the response (recall that with small values of h_0, the PV contours are essentially latitude lines). As h_0 is increased, the correlations grow and they are constant above $h_0=800$. The correlation coefficients are 0.68, implying reasonably good agreement.

[40] The latter is confirmed by comparing the two time series (Figure 8). Both are dominated by the seasonal signal, with negative values (SLA lower on inner contour than on outer contour) during winter months, indicating anomalous cyclonic circulation. The ratio of the model's RMS value to the observed value is 1.1, so the model captures both the variability and the amplitude of the signal.

[41] The fact that the correlations do not decrease as h_0 gets large suggests that a model based on f/H would do equally well as the equivalent barotropic model here. We confirmed this. This in turn implies topography exerts a controlling effect in the central basin, regardless of the stratification.

4.2. Southern Basin

[42] Figures 9 and 10 show the corresponding results for the southern basin. As in the central basin, the model-data

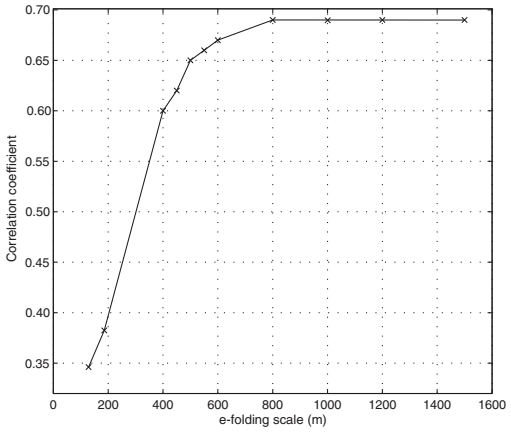

Figure 7. The correlation coefficient (R_c) between the satellite observations and the EB model as a function of e-folding scale (H_0) for the central basin.

correlations are lowest with small values of h_0 and they are larger and approximately constant for large values. But they are also slightly higher at an intermediate decay scale, around $h_0 = 500$. So it would seem the EB model is slightly better than a barotropic f/H model here. The correlations nevertheless are somewhat lower than in the central basin, reaching a maximum value of about 0.58.

[43] The time series from the satellite and the model, with $h_0 = 500$, are shown in Figure 10. The seasonal cycle is less pronounced than in the central basin, in both time series. But the two series are less similar than in the central basin. Moreover, the ratio of the RMS amplitudes is 0.7; so the model somewhat under-predicts the amplitude of the response.

[44] The preceding results suggest perhaps that the agreement is superior in the central basin because the seasonal signal is more pronounced there. This is partly true. Shown in Figure 11 are the coherences as functions of frequency. Results are shown both for the EB model and the barotropic (large h_0) version of the model. The coherences are insignificant on time scales less than about 5 months, in both basins. In the central basin, the coherence peaks at around 10 months, or roughly one year; this is consistent with the model capturing the seasonal cycle. It decays at longer time scales. And the barotropic model performs equally well as the EB model, as noted before. In the southern basin the response is similar, but the coherences are also lower. They are largest at around 1 year too, but the difference is less marked from the lower frequencies. Furthermore, the barotropic model produces consistently lower coherences than the EB model.

[45] The fact that the coherences are low on the short time scales is to be expected from the model. With $H \sim 1000$ m and $R = 5\times10^{-4}$ m, the barotropic decay time scale, $T_d \equiv H/R$, is on the order of a month. The time scale in the EB model is longer because the velocity shear reduces the bottom velocities; with $h_0 = 500$ m, it is roughly five times longer. The model assumes that time variations in the circulation are equally long (otherwise the first-order flow would not be along f/F contours). So it is not surprising we capture only time scales exceeding a few months.

[46] That the coherences also decrease for the long time scales is consistent with the results found by *Isachsen et al.* [2003]. At these scales, baroclinic effects presumably come into play, effects which cannot be captured in an equivalent barotropic model. So the model is most effective on the intermediate time scales, particularly at the seasonal frequency.

4.3. Comparison With Current Meter Observations

[47] Lastly we revisit the mooring data from the southern basin and compare the along- f/F velocities at the deepest mooring with the model predictions. The model velocities were calculated from (14) and (17). As before, we use a drag coefficient of $R = 5.0\times10^{-4}$ m s^{-1} and an e-folding scale of $h_0 = 500$ m.

[48] The observed and modeled velocity time series (Figure 12) show some similarities. The correlation coefficient, 0.48, is slightly lower than that obtained with the SLA data in the southern basin. This is to be expected, as the entire current meter record is just over six months long. From the preceding discussion, the model is better at capturing the month-to-month variations than those on shorter time scales. The ratio of the RMS velocities is ~0.8, so the predicted amplitude is also reasonable.

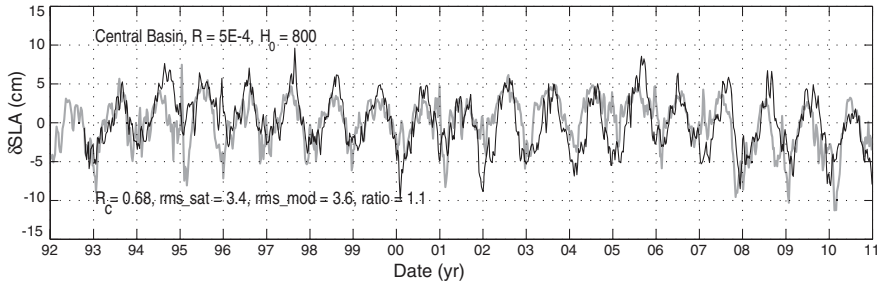

Figure 8. Time series of the relative sea level displacements between the rim and inner q_e contours in the central basin where $H_0 = 800$. The thin and thick lines indicate weekly time series of the sea level anomalies based on the satellite observations and the EB model predictions, respectively.

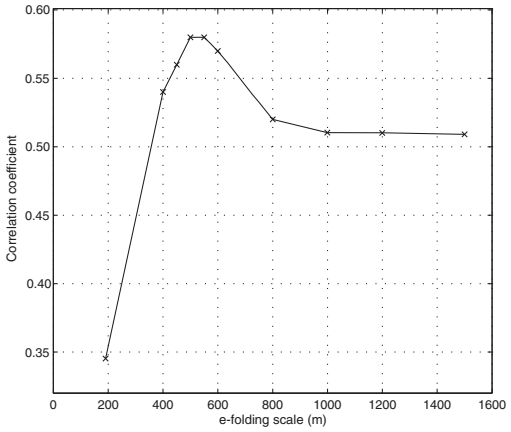

Figure 9. The correlation coefficient (R_c) between the satellite observations and the EB model as a function of e-folding scale (H_0) for the southern basin.

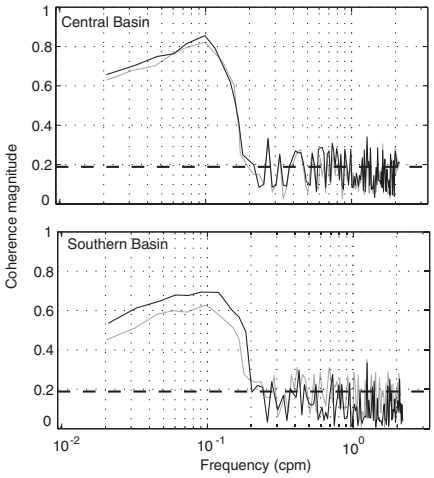

Figure 11. Coherence estimates between the models and the satellite measurements as functions of the frequency for (top) the central and (bottom) the southern basins. The dark and light lines represent the coherence between the EB model and observation and the barotropic model and observation, respectively. The dashed line shows 95% confidence level.

[49] Note that the assumed e-folding scale of 500 m is somewhat larger than the e-folding scale deduced from the first EOF from the current meter, which was 350 m. Using $h_0 = 350$ m yields a slightly lower correlation $\sim$0.4 and also a lower amplitude ratio $\sim$0.6. Nevertheless, this is fairly inconclusive, given the short record length.

[50] Interestingly, the observed fluctuations lag the EB model prediction, by roughly 1 week. Accordingly, adding a 5 day lag to the model time series raises the correlation coefficient from 0.48 to 0.64, and most of the increase is due to a better match at shorter time scales. But it is clear that such comparisons should be done with a longer time series before any speculation is made.

5. Summary and Conclusions

[51] We have used a linear analytic model to study current fluctuations in the central and southern portions of the Caspian Sea. The model assumes the flow is wind driven and that dissipation is entirely by bottom drag. Motivated by current meter satellite altimeter observations, the velocities are assumed to be equivalent barotropic (EB) and aligned with EB PV contours, the f/F contours (where F is a modified function of depth which takes the vertical decay of the velocities into account). These contours close on themselves in both the central and southern basins of the Caspian Sea and allow us to estimate the flow variability from a simplified expression. A barotropic version of the model was used previously to study the response in the Nordic Seas and Arctic Ocean [*Isachsen et al*., 2003]. The modification to EB flow and the application to the midlatitude Caspian Sea is new.

[52] The model was reasonably successful at simulating current variability on time scales exceeding a few months.

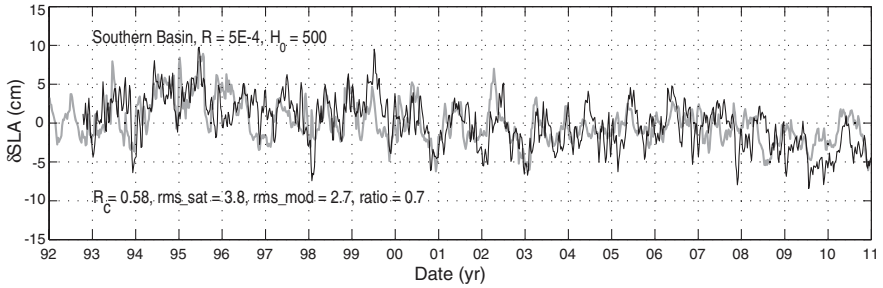

Figure 10. Time series of the relative sea level displacements between the rim and inner q_e contours in the southern basin where $H_0 = 500$. The thin and thick lines indicate weekly time series of the sea level anomalies based on the satellite observations and the EB model predictions, respectively.

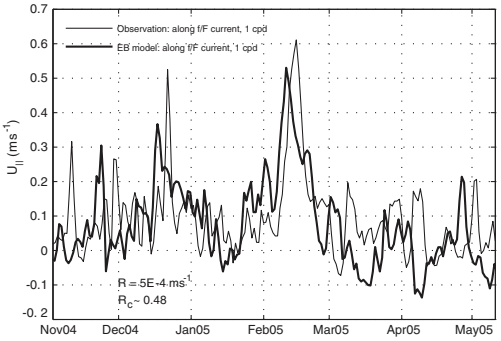

Figure 12. The depth-averaged along-*f*/*F* currents. The thin solid line; the weighted depth-averaged recorded velocities from the third mooring. The thick line; the EB model prediction.

In the central basin, where the stratification is weaker, the *f*/*F* model and the barotropic *f*/*H* limit yield comparable results. Both agree with the satellite observations of low frequency (seasonal to annual time scales) sea surface height variability. In the southern basin, the stratification is stronger. As such, the EB model is more successful than the barotropic model. We find reasonable correlations with both the satellite data and with the current meter data, again primarily on time scales of seasons to a few years.

[53] The coherences here are also somewhat less than those obtained in the Nordic Seas. In some cases there, the correlation coefficients exceeded 0.8. This is likely due to having weaker stratification at those latitudes. Nevertheless, the dependence of the coherences on frequency was similar. The (barotropic) model was most successful at intermediate frequencies, capturing primarily seasonal variations.

[54] It should be emphasized what the analytical model leaves out. The assumption that the flow is dominated by a component which is purely along the PV contours removes all dynamics with cross-contour flow. This includes topographic and internal Kelvin waves. The associated time scales are on the order of several days in the Caspian Sea (J. E. H. Weber and P. Ghaffari, Mass transport in internal coastal Kelvin waves, submitted to *European Journal of Mechanics B*, 2013.) The assumption of barotropic or quasi-barotropic motion neglects baroclinic effects, and this evidently decreases coherences on interannual time scales. To take such effects into account will require additional assumptions about the density field. As suggested by the findings of *Nöst and Isachsen* [2003] and *Aaboe and Nöst* [2008], a time-mean solution may then be found in which the connection between the top and bottom Ekman layers is modified by the divergence of the meridional thermal wind transport.

[55] Nevertheless, the model is appealing for its extreme simplicity. A first-order assessment of intermonthly variability can be estimated using a single equation and a simple Matlab routine. The model moreover should be applicable in other regions, and possibly in large inland lakes.

[56] Further assessments in the Caspian Sea would clearly benefit from more observations, particularly from longer-term current measurements in both basins. Studies using primitive equation models would also help unravel the possible role of nonlinearities and eddy momentum transport, processes that have been ignored here.

[57] **Acknowledgments.** We thank Andrey Trebler and Paula Pérez Brunius for helpful comments.

References

Aaboe, S., and O. A. Nöst (2008), A diagnostic model of the Nordic Seas and Arctic Ocean circulation: Quantifying the effects of a variable bottom density along a sloping topography, *J. Phys. Oceanogr.*, *38*, 2685–2703.

Bondarenko, A. L. (1993), *Currents of the Caspian Sea and Formation of Salinity of the Waters of the North Part of the Caspian Sea* [in Russian], 122 pp., Nauka, Moscow, Russia.

Ghaffari, P., and V. Chegini (2010), Acoustic Doppler current profiler observations in the southern Caspian Sea: Shelf currents and flow field off feridoonkenar bay, Iran, *Ocean Sci.*, *6*(3), 737–748, doi:10.5194/os-6–737-2010.

Ghaffari, P., H. A. Lahijani, and J. Azizpour (2010), Snapshot observation of the physical structure and stratification in deep-water of the south Caspian Sea (western part), *Ocean Sci.*, *6*(4), 877–885, doi:10.5194/os-6-877-2010.

Gill, A. E. (1982), *Atmosphere-Ocean Dynamics*, vol. 30, edited by W. L. Donn, 662 pp., Academic, San Francisco, Calif.

Greenspan, H. P. (1990), *The Theory of Rotating Fluids*, 352 pp., Breukelen Press, Brookline, Mass.

Hasselmann, K. (1982), An ocean model for climate variability studies, *Prog. Oceanogr.*, *11*(2), 69–92, doi:10.1016/0079-6611(82)90004-0.

IAEA (1996), Research/training on the Caspian Sea, *Data Rep*. 1995, p. *95*, Int. At. Energy Agency, Wien.

Ibrayev, R. A., E. Özsoy, C. Schrum, and H. İ. Sur (2010), Seasonal variability of the Caspian Sea three-dimensional circulation, sea level and air-sea interaction, *Ocean Sci.*, *6*(1), 311–329, doi:10.5194/os-6-311-2010.

Isachsen, P. E., J. H. LaCasce, C. Mauritzen, and S. Häkkinen (2003), Wind-driven variability of the large-scale recirculating flow in the Nordic Seas and arctic ocean, *J. Phys. Oceanogr.*, *33*(12), 2534–2550, doi:10.1175/1520-0485(2003)033<2534:WVOTLR>2.0.CO;2.

Ismailova, B. (2004), Geoinformation modeling of wind-induced surges on the northern-eastern Caspian Sea, *Math. Comput. Simul.*, *67*(4–5), 371–377, doi:10.1016/j.matcom.2004.06.021.

Ivchenko, V., A. Krupitsky, V. Kamenkovich, and N. Wells (1999), Modeling the Antarctic circumpolar current: A comparison of FRAM and equivalent barotropic model results, *J. Mar. Res.*, *57*(1), 29–45, doi:10.1357/002224099765038553.

Kaihatu, J. M., R. A. Handler, G. O. Marmorino, and L. K. Shay (1998), Empirical orthogonal function analysis of ocean surface currents using complex and real-vector methods, *J. Atmos. Oceanic Technol.*, *15*(4), 927–941.

Kamenkovich, V. M. (1962), On the theory of the Antarctic circumpolar current, *Trudy Inst. Okeanol.*, *56*, 245–306.

Killworth, P. D. (1992), An equivalent-barotropic mode in the fine resolution Antarctic model, *J. Phys. Oceanogr.*, *22*, 1379–1387.

Kosarev, A. N. (1975), *Gidrologiya Kaspiiskogo I Aralskogo morey*, 270 pp., Moscow Univ. Press, Moscow.

Kostianoy, A. (2005), Handbook of environmental chemistry, in *The Caspian Sea Environment*, vol. *5/P*, edited by A. N. Kosarev and A. G. Kostianoy, 271 pp., Springer, Berlin, Germany.

Krupitsky, A., V. M. Kamenkovich, N. Naik, and M. A. Cane (1996), A linear equivalent barotropic model of the Antarctic circumpolar current with realistic coastlines and bottom topography, *J. Phys. Oceanogr.*, *26*(9), 1803–1824.

LaCasce, J. (2000), Floats and f/h, *J. Mar. Res.*, *58*(1), 61–95.

LaCasce, J., and P. E. Isachsen (2010), The linear models of the acc, *Prog. Oceanogr.*, *84*, 139–157.

Lebedev, S. A., and A. G. Kostianoy (2006), Satellite altimetry of the Caspian Sea, *Eur. Space Agency Spec. Publ. ESA SP 614, 6*, 113–120.

Nöst, O. A., and P. E. Isachsen (2003), The large-scale time-mean ocean circulation in the Nordic Seas and Arctic Ocean estimated from simplified dynamics, *J. Mar. Res.*, *61*(2), 175–210.

Peeters, F., R. Kipfer, D. Achermann, M. Hofer, W. Aeschbachhertig, U. Beyerle, D. M. Imboden, K. Rozanski, and K. Fröhlich (2000), Analysis of deep-water exchange in the Caspian Sea based on environmental tracers, *Deep Sea Res., Part I*, *47*, 621–654, doi:10.1016/S0967-0637(99)00066-7.

Terziev, F. S., A. Kosarev, and A. A. Kerimov (Eds.) (1992), *The Seas of the USSR. Hydrometeorology and Hydrochemistry of the Seas*, vol. VI, *The Caspian Sea, Issue 1: Hydrometeorological Conditions, Gidrometeoizdat*, St. Petersburg, Russia.

Trukhchev, D., A. Kosarev, D. Ivanova, and V. Tuzhilkin (1995), Numerical analysis of the general circulation in the Caspian Sea, *C. R. Acad. Bulgare Sci.*, *48*(10), 35–38.

Young, W. R. (1981), A theory of the wind-driven circulation, PhD thesis, MIT-WHOI Joint Prog. in Oceanogr., 215 pp.

Zaker, N. H., P. Ghaffari, S. Jamshidi, and M. Nouranian (2011), Currents on the southern continental shelf of the Caspian Sea off Babolsar, Mazandaran in Iran, *J. Coastal Res.*, *64*, 1989–1997.

II

Journal of Marine Research, 67, 213–224, 2009

Mass transport in the Stokes edge wave

by Jan Erik H. Weber[1,2] and Peygham Ghaffari[1]

ABSTRACT

The Lagrangian mass transport in the Stokes progressive edge wave is obtained from the vertically integrated equations of momentum and mass, correct to second order in wave steepness. The cross-shore momentum balance is between the mean pressure at the sloping bottom, the radiation stress, and the pressure gradient due to the mean surface slope. In the alongshore direction, the effect of viscosity leads to a wave attenuation, and hence a radiation stress component. The frictional effect on the mean Eulerian motion is modeled through a turbulent bottom drag. The alongshore momentum balance is between the mean pressure gradient due to the surface slope, the radiation stress, and the turbulent drag on the mean Eulerian flow. It is shown that $-\partial E/\partial y$, where E is the total mean energy density for waves along the y-axis, is the wave-forcing term for the total mean Lagrangian momentum in the trapping region. This result is independent of the bottom slope angle. Vertically-averaged drift velocity components are obtained from the fluxes, divided by the local depth. Utilizing physical parameters relevant for field conditions, it appears the traditional Stokes drift in the Stokes edge wave is negligible compared to the mean Eulerian velocity component. The importance of this drift for the near-shore transport of effluents and suspended light sediments is discussed.

1. Introduction

After being regarded as a mere curiosity for many years, e.g. Lamb (1932), edge waves have fairly recently received renewed interest. This is because such waves apparently play an important role in the dynamics of coastal zone and beach erosion processes (LeBlond and Mysak, 1978). Edge waves are often considered as the major factor of the long-term evolution of the irregular coastal line, forming rhythmic crescentic bars (Bowen and Inman, 1971; Kurkin and Pelinovsky, 2003; Quevedo *et al.,* 2008). Holman and Bowen (1982) showed that the steady drift, generated by the nonlinear self-interaction of edge waves inside the bottom boundary layer, can cause a net displacement of the sediment and give rise to bottom patterns similar to those detected in the field.

We here concentrate on the Stokes edge wave (Stokes, 1846), which is the first mode in the spectrum of shelf modes that contains both discrete and continuous parts (Eckhart, 1951; Ursell, 1952; Reid, 1958). Several mechanisms for generating edge waves are possible in nature. Large-scale edge waves can be generated by direct wind stress above the

1. Department of Geosciences, University of Oslo, Norway.
2. Corresponding author. ***email: j.e.weber@geo.uio.no***

water, by traveling air pressure, or by tsunamis (Munk *et al.,* 1956; Aida, 1967; Beardsley *et al.,* 1977; Fuller and Mysak, 1977; Golovachev *et al.,* 1992; Boss *et al.,* 1995; Kurkin and Pelinovsky, 2003; Galletta and Vittori, 2004; Monserrat *et al.,* 2006), while medium- and small-scale edge waves may occur through nonlinear interaction of wave groups or nonlinear subharmonic resonance mechanisms (Gallagher, 1971; Minzoni and Whitham, 1977; Bowen and Guza, 1978; Chapman, 1984). The occurrence of edge waves has also been demonstrated in wave tank experiments (Yeh, 1985; Mok and Yeh, 1999).

In the present study we focus on the mass transport induced by the Stokes edge wave. Earlier papers, (e.g. Kenyon (1969)) have considered the pure Stokes drift (Stokes, 1847) in inviscid edge waves applying the hydrostatic approximation, while Dore (1975) and Mok and Yeh (1999) have calculated the mass transport velocity in the viscous laminar bottom boundary layer associated with edge wave motion. But obviously, real field bottom boundary layers are turbulent. Furthermore, the frictional effect at the bottom will generate a mean interior Eulerian flow, in addition to the Stokes drift (Longuet-Higgins, 1953). It is the aim of the present paper to quantify the mean Eulerian mass transport generated by the Stokes edge wave in a turbulent ocean. When we add the Stokes flux, we obtain the total mean Lagrangian mass transport in the system. It is this transport that advects neutral tracers and bottom sediment in suspension in the region of wave trapping. In order to obtain a robust formulation, we consider the vertically integrated equations of momentum and mass, e.g. Phillips (1977), and derive the mean Lagrangian mass transport to second order in wave steepness. The vertically-averaged drift velocity is obtained by dividing the volume flux by the local depth. In this way we do not resolve the motion in the bottom boundary layer, so this method is not directed at sediment transport very close to the sea bed. However, for finer sediment that is mixed in the entire water column, and the drift of biological material, the present approach yields new and interesting results.

2. Mathematical formulation

We consider trapped surface gravity waves in a homogeneous incompressible fluid with a linearly sloping bottom. The motion is described in a Cartesian system, where the x-axis is situated at the undisturbed surface and directed into the semi-infinite sea, the y-axis is directed along the shore line, and the vertical z-axis is positive upwards; see the sketch in Figure 1. The corresponding velocity components are (u, v, w). Furthermore, the pressure is p and the constant density is ρ. The bottom is given by $z = -h = -x \tan \beta$, where β ($\leq \pi/2$) is the sloping angle, and the free surface by $z = \eta$. At the free surface the pressure is constant. In this study we disregard the effect of the earth's rotation.

We denote periodic wave variables by a tilde, and the mean flow (averaged over the wave period) by an over-bar. Mean horizontal volume fluxes $(\bar{U}, \bar{V})$ are defined by

$$\bar{U} = \overline{\int_{-h}^{\eta} u dz}, \quad \bar{V} = \overline{\int_{-h}^{\eta} v dz}. \tag{1}$$

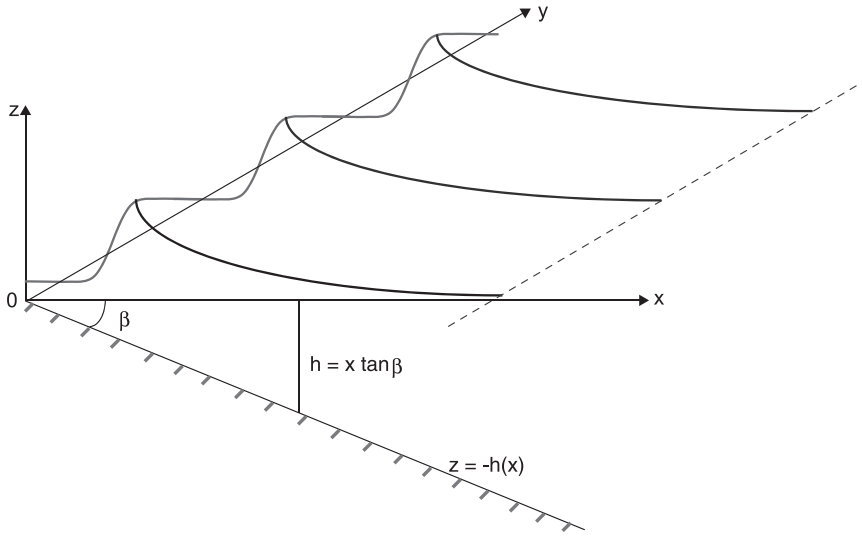

Figure 1. Sketch depicting the coordinate system, with the surface and sloping bottom included; y is the alongshore coordinate and the seawards direction is $x \to \infty$.

These are actually the Lagrangian fluxes, since we integrate between material boundaries (Phillips, 1977; Weber *et al.,* 2006). Integrating the governing equations in the vertical, and utilizing the full nonlinear boundary conditions at the free surface and the sloping bottom, we obtain for the mean quantities, correct to second order in wave steepness (Phillips, 1977):

$$\begin{aligned}
\frac{\partial \bar{U}}{\partial t} &= -\frac{1}{\rho}\frac{\partial}{\partial x}\int_{-h}^{0} \bar{p}dz - \frac{1}{2\rho}\frac{\partial}{\partial x}\,\overline{\tilde{p}(0)\tilde{\eta}} + \frac{1}{\rho}\tan\beta \bar{p}(-h) \\
&\qquad - \frac{\partial}{\partial x}\int_{-h}^{0} \overline{\tilde{u}\tilde{u}}dz - \frac{\partial}{\partial y}\int_{-h}^{0} \overline{\tilde{u}\tilde{v}}dz - \frac{\bar{\tau}_{-h}^{(x)}}{\rho}, \\
\frac{\partial \bar{V}}{\partial t} &= -\frac{1}{\rho}\frac{\partial}{\partial y}\int_{-h}^{0} \bar{p}dz - \frac{1}{2\rho}\frac{\partial}{\partial y}\,\overline{\tilde{p}(0)\tilde{\eta}} - \frac{\partial}{\partial x}\int_{-h}^{0} \overline{\tilde{u}\tilde{v}}dz - \frac{\partial}{\partial y}\int_{-h}^{0} \overline{\tilde{v}\tilde{v}}dz - \frac{\bar{\tau}_{-h}^{(y)}}{\rho}, \\
\frac{\partial \bar{\eta}}{\partial t} &= -\frac{\partial \bar{U}}{\partial x} - \frac{\partial \bar{V}}{\partial y}.
\end{aligned} \tag{2}$$

By neglecting the effect of friction in the vertical component of the momentum equation, Phillips found for the mean pressure to this order:

$$\frac{\bar{p}}{\rho} = g(\bar{\eta} - z) - \overline{\tilde{w}^2} + \frac{\partial}{\partial x}\int_{z}^{0} \overline{\tilde{u}\tilde{w}}d\xi + \frac{\partial}{\partial y}\int_{z}^{0} \overline{\tilde{v}\tilde{w}}d\xi, \tag{3}$$

where g is the acceleration due to gravity. As shown by Mei (1973) for the Stokes standing edge wave, the dynamic mean bottom pressure term in the x-momentum, $\tan\beta\bar{p}(-h)/\rho$ which is missing from Phillips' derivation, must be present here. Furthermore, $(\bar{\tau}^{(x)}_{-h}, \bar{\tau}^{(y)}_{-h})$ in (2) are the mean turbulent bottom stress components.

In this problem the oscillatory edge wave motion is influenced by viscosity. In general; for deep water waves, viscosity will affect the motion in the bulk of the fluid, while for shallow water the viscous boundary layer at the bottom will dominate. In both cases the potential part of the wave field, which is the relevant one in flux consideration, will attenuate exponentially in time. For deep water the damping coefficient will be proportional to the small viscosity coefficient, while in shallow water the damping coefficient will be larger (no slip at the bottom). In this case it is proportional to the square of the viscosity coefficient, e.g. Phillips (1977). In any case, we can obtain the potential part of the wave field by using a friction that is linear in the wave velocity, yielding the small exponential decay in time. Accordingly, we write the frictional force per unit mass on the linear wave motion as $-r\vec{\tilde{u}}$, where the constant friction coefficient r depends on the viscosity. This kind of friction does not introduce vorticity into the fluid, so we can apply the potential theory of Stokes (1846). The linearized relation between the velocity potential $\tilde{\varphi}$ and the pressure then becomes

$$\tilde{p} = -\rho\left(\frac{\partial\tilde{\varphi}}{\partial t} + gz + r\tilde{\varphi}\right). \tag{4}$$

In the present problem we consider waves with given frequency ω. Then, due to friction, the wave number κ in the y-direction (along the coast) will be complex, i.e. $\kappa = k + i\alpha$, where $k > 0$, and α is the small spatial attenuation coefficient ($\alpha/k \ll 1$). In fact, for a general set of wave problems, the temporal attenuation coefficient is equal to the spatial one times the group velocity of the wave (Gaster, 1962).

For the spatially damped Stokes edge wave, we can write the complex velocity potential

$$\tilde{\varphi} = -\frac{ia\omega}{k\sin\beta}\exp(-kx\cos\beta + kz\sin\beta - \alpha y + i(ky - \alpha x\cos\beta + \alpha z\sin\beta - \omega t)), \tag{5}$$

where a is the wave amplitude. The potential part of the velocity is given by $\vec{\tilde{u}} = \nabla\tilde{\varphi}$, and it is easily seen that (5) satisfies the Laplace equation, and the tangential flow condition at the linearly sloping bottom. From the dynamic condition at the free surface, $\tilde{p}(z = \tilde{\eta}) = 0$, we find to lowest order for the wave frequency and the spatial damping coefficient:

$$\omega^2 = gk\sin\beta, \quad \alpha = \frac{kr}{\omega}. \tag{6}$$

Hence waves can propagate in both directions, becoming damped as they progress along the y-axis. We here consider propagation to the right, i.e. take $\omega > 0$.

To determine the damping rate, we need to quantify the friction coefficient r. If we neglect the effect of a viscous boundary layer along the sloping bottom, which is permissible for large depths (i.e. large x), we can determine the temporal wave attenuation coefficient γ from energy considerations (Phillips, 1977). Using real parts from potential theory, we find for the total mean energy density that

$$E = \int_0^\infty \left\{ \int_{-h}^0 \overline{\frac{\rho}{2}(\tilde{u}^2 + \tilde{v}^2 + \tilde{w}^2)}dz + \rho g \overline{\int_0^{\tilde{\eta}} z dz} \right\} dx = \frac{\rho g a^2}{4k \cos\beta} \exp(-2\gamma t), \tag{7}$$

while the total dissipation D in this problem is readily found to be

$$D = -\frac{\rho \nu g k a^2}{2 \cos\beta} \exp(-2\gamma t). \tag{8}$$

Assuming that $dE/dt = D$ (Phillips, 1977) we obtain

$$\gamma = k^2 \nu, \tag{9}$$

which is exactly half the value for ordinary deep-water surface waves. Utilizing Gaster (1962), we find the spatial attenuation coefficient for this case:

$$\alpha = \frac{\gamma}{d\omega/dk} = \frac{2k^3\nu}{\omega}. \tag{10}$$

For shallow water waves the temporal damping coefficient is related to the eddy viscosity coefficient ν by the relation $\gamma = \nu/(2H\delta)$, where H is the mean depth, and $\delta = (2\nu/\omega)^{1/2}$ is the viscous boundary-layer thickness (Phillips, 1977). A typical depth here will be that at the outer edge of the trapping region, i.e. we take $H = \tan\beta/k$. Then, applying Gaster's result, the spatial attenuation coefficient in this case becomes:

$$\alpha = \frac{k^2}{\tan\beta}\left(\frac{\nu}{2\omega}\right)^{1/2}. \tag{11}$$

It should be noted that (10) and (11) are the two extreme values for frictional damping in our problem. For realistic field conditions the water will be shallow. Therefore, the value given by (11) will in practice represent the magnitude of the spatial damping in our problem. In any case, the friction coefficient is obtained from (6), i.e. $r = \omega\alpha/k$.

Utilizing the real part of (5), it is trivial to calculate the right-hand side of (2). The x- and y-components of the Lagrangian fluxes to second order in wave steepness then becomes

$$\frac{\partial \bar{U}}{\partial t} + gh\frac{\partial \bar{\eta}}{\partial x} = \left(\frac{gka}{\omega}\right)^2 (kx \cos^2\beta \sin\beta) \exp(-2kx\cos\beta - 2\alpha y) - \bar{\tau}_{-h}^{(x)}/\rho. \tag{12}$$

$$\frac{\partial \bar{V}}{\partial t} + gh\frac{\partial \bar{\eta}}{\partial y} = \frac{\alpha}{2k}\left(\frac{gka}{\omega}\right)^2 (kx \sin 2\beta + \sin\beta) \exp(-2kx\cos\beta - 2\alpha y) - \bar{\tau}_{-h}^{(y)}/\rho. \tag{13}$$

In this calculation we have neglected all terms proportional to $(\alpha/k)^2$, and higher orders. As demonstrated by Mei (1973) for standing edge waves in the absence of friction, the first term on the right-hand side of (12) is the divergence of the radiation stress component by Longuet-Higgins and Stewart (1960) plus the contribution from the dynamic bottom pressure, i.e. $\{-\partial S_{11}/\partial x + \tan\beta\bar{p}(-h)\}/\rho$. It is easily verified that the first term on the right-hand side of (13) is just $\{-\partial S_{22}/\partial y\}/\rho$, where S_{22} is given by Mei (1973) in the case when $\alpha = 0$.

Following Longuet-Higgins (1953), the Stokes drift $(\bar{u}_S, \bar{v}_S)$ to second order in wave steepness for this problem is easily obtained from the linear wave solutions. By integrating in the vertical, we get the Stokes flux for this problem:

$$\bar{U}_S = \int_{-h}^{0} \bar{u}_S dz = 0,$$

$$\bar{V}_S = \int_{-h}^{0} \bar{v}_S dz = \frac{gka^2}{2\omega \sin^2\beta} (\exp(-2kx\cos\beta - \exp(-2kx\sec\beta)) \exp(-2\alpha y). \tag{14}$$

The total wave momentum in the trapped region thus becomes:

$$M = \rho \int_0^{\infty} \bar{V}_S dx = \frac{\rho g a^2}{4\omega\cos\beta} \exp(-2\alpha y). \tag{15}$$

For inviscid flow ($\alpha = 0$), and shallow water ($\cos\beta \approx 1$), this result conforms to that of Kenyon (1969). For the spatially damped Stokes edge wave, the energy density (7) becomes

$$E = \frac{\rho g a^2}{4k\cos\beta} \exp(-2\alpha y). \tag{16}$$

From (15) and (16) we note that $E = Mc$, where $c = \omega/k$ is the phase speed. This is in accordance with Starr's (1959) general result for waves.

For the total momentum balance in the trapping region, we integrate the alongshore component (13) in the x-direction from the shore to infinity. Defining

$$Q = \rho \int_0^{\infty} \bar{V} dx, \quad B = \rho g \int_0^{\infty} h\bar{\eta} dx, \quad T_B = \int_0^{\infty} \bar{\tau}^{(y)}_{-h} dx, \tag{17}$$

we find for the rate of change of the total mean Lagrangian momentum Q that

$$\frac{\partial Q}{\partial t} = -\frac{\partial B}{\partial y} - \frac{\partial E}{\partial y} - T_B. \tag{18}$$

We note the interesting difference between the Stokes edge wave and plane surface waves in the y-direction. In the latter case the radiation stress forcing on the right-hand side would be $-\partial(E/2)/\partial y$ for deep water waves and $-\partial(3E/2)/\partial y$ for shallow water waves (Longuet-Higgins and Stewart, 1960). For the Stokes edge wave the water appears shallow for small x, and deep for large x. Hence, the cross-shore integration yields the in-between value $-\partial E/\partial y$ for the forcing term, as seen from (18).

3. Steady mass transport

We consider the steady mass transport. The turbulent bottom stresses are modeled by the mean Eulerian velocities. In the direction normal to the coast the velocities are small. Here we can neglect the bottom friction, and the balance to lowest order in this direction is between the pressure gradient due to the mean surface slope, the radiation stress component, and the mean dynamic pressure at the sloping bottom (Mei, 1973). From (12) we then obtain for the mean surface slope

$$g\bar{\eta} = -\frac{1}{2}\left(\frac{gka\cos\beta}{\omega}\right)^2 \exp(-2kx\cos\beta - 2\alpha y). \tag{19}$$

Assuming that the alongshore mean velocity is much larger than the cross-shore one, we write the turbulent bottom stress in the y-direction:

$$\bar{\tau}^{(y)}_{-h}/\rho = c_D|\bar{V}_E|\bar{V}_E/h^2. \tag{20}$$

where c_D is a bottom drag coefficient. From Longuet-Higgins (1953) we have for the mean alongshore Eulerian volume flux induced by friction:

$$\bar{V}_E = \bar{V}_L - \bar{V}_S. \tag{21}$$

where the Lagrangian flux $\bar{V}_L$ is equal to $\bar{V}$ in (1), and $\bar{V}_S$ is given by (14). Inserting (19) and (20) into (13), we obtain for the steady mean Eulerian volume flux:

$$\bar{V}_E = \left(\frac{g\alpha a^2}{2c_D}\right)^{1/2} x\tan\beta\exp(-kx\cos\beta - \alpha y). \tag{22}$$

The present approach separates the decay of wave momentum from the frictional influence on the mean flow, which is physically sound (Jenkins, 1989; Weber and Melsom, 1993; Ardhuin and Jenkins 2006). We note from (22) that it is the divergence of the radiation stress through spatial wave decay that drives the mean Eulerian flow, while the magnitude depends on the turbulence (the roughness etc.) at the sloping bottom. A turbulent decay of wave energy ($\alpha > 0$) cannot exist without a turbulent bottom drag on the mean flow, so the limit: α small and finite, $c_D \to 0$ in (22), is unphysical.

From the continuity equation we obtain for the cross-shore flux in a steady state:

$$\frac{\partial \bar{U}_E}{\partial x} = -\frac{\partial(\bar{V}_S + \bar{V}_E)}{\partial y}. \tag{23}$$

We then find, assuming that $\bar{U}_E\,(x = 0) = 0$:

$$\begin{aligned}\bar{U}_E = \frac{g\alpha a^2}{2\omega \sin^2\beta \cos\beta}\,&(\sin^2\beta - \exp(-2kx\cos\beta)\\ &+ \cos^2\beta \exp(-2kx\sec\beta))\exp(-2\alpha y)\\ &+ \left(\frac{g\alpha^3 a^2}{2c_D k^4}\right)^{1/2}\frac{\sin\beta}{\cos^3\beta}(1 - (1 + kx\cos\beta)\exp(-kx\cos\beta))\exp(-\alpha y).\end{aligned} \tag{24}$$

We realize that from this that $|\bar{U}_E/\bar{V}_E| = O(\alpha/k)$, which justifies the neglect of the cross-shore velocity in the bottom drag (20).

We now define the along-shore vertically-averaged Stokes drift $\langle v_S\rangle$, the and Eulerian mean current $\langle v_E\rangle$ by

$$\langle v_S\rangle = \bar{V}_S/h, \quad \langle v_E\rangle = \bar{V}_E/h, \tag{25}$$

where $h = x\tan\beta$. The vertically-averaged Lagrangian drift thus becomes

$$\langle v_L\rangle = \langle v_S\rangle + \langle v_E\rangle. \tag{26}$$

It easily seen that these average velocities have a maximum at the coast ($x = 0$).

In order to relate our theoretical results to the natural environment, we consider shallow water, and take $\beta = 0.1$ as a typical beach slope angle. High-frequency edge waves yield the largest drift velocities, while low-frequency waves related to the motion of atmospheric low-pressure systems have higher total mass fluxes (Kenyon, 1969). We here focus on drift velocities, and use the classic observation by Munk (1949) in the surf-beat range, giving a wave period $T = 60$ s, and a wave amplitude $a = 0.1$ m. For the modeling of tidal currents in the Barents Sea typical values of the eddy viscosity and bottom drag coefficients are $\nu = 10^{-3}$ m^2 s^{-1} (Nøst, 1994), and $c_D = 3 \times 10^{-3}$ (Gjevik *et al.,* 1994; Nøst, 1994), respectively. At a sloping beach, eddy viscosity estimates are higher by a factor of 10 to 50 (Apotsos *et al.,* 2007), mainly due to turbulence induced by breaking waves. Reported drag coefficients seaward of the surf zone is comparable with those used for tidal current modeling. From Feddersen *et al.* (2003) we find that $c_D \approx 2 \times 10^{-3}$ outside the surf zone. Normally, we will expect a considerable amount of turbulence within the trapping region of edge waves. Without specifying the source of turbulence, which is outside the scope of this paper, it seems reasonable to take $\nu = 5 \times 10^{-3}$ m^2 s^{-1} and $c_D = 2.5 \times 10^{-3}$ in quantifying the drift induced by the Stokes edge wave. In Figure 2 we have plotted the vertically-averaged velocities (25) and (26) as function of seaward distance for the physical parameters given here. We note that the Eulerian mean velocity is the dominating component of the Lagrangian drift velocity. In the present example we find $\langle v_L\rangle\,(x = 0, y = 0) \approx 6$ cm s^{-1}. This is in fact a mean mass transport velocity which is

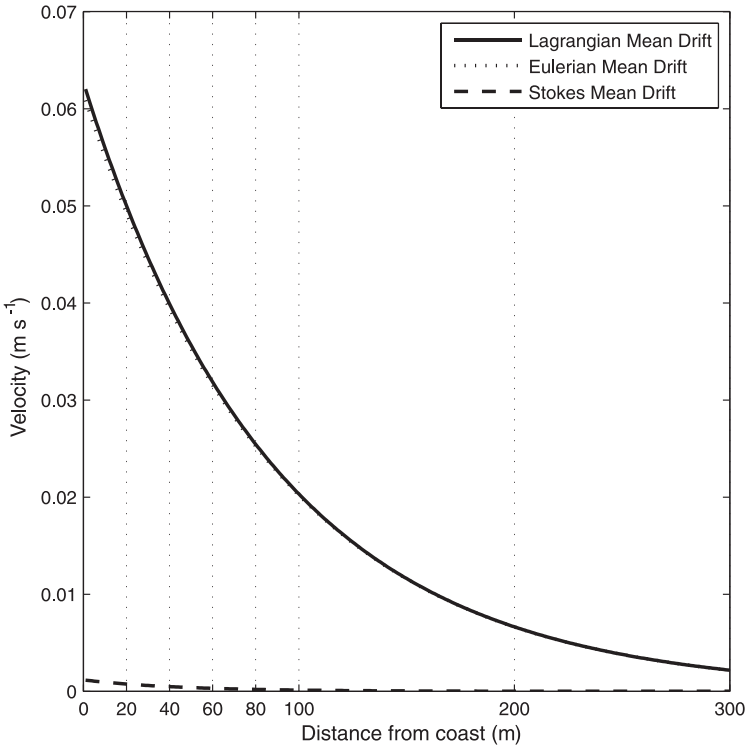

Figure 2. Mean drift velocity components (25) and (26) at $y = 0$, *vs.* distance from the coast x. Dashed line depicts $\langle v_S \rangle$, dotted and solid lines depict $\langle v_E \rangle$, and $\langle v_L \rangle$, respectively. The physical parameters are: $a = 0.1$ m, $T = 60$ s, $\nu = 5 \times 10^{-3}$ m^2 s^{-1}, and $c_D = 2.5 \times 10^{-3}$.

comparable to traditional wind surge velocities. The drift velocity components decay exponentially in the seaward direction. The alongshore drift becomes negligible outside the wave trapping zone $x > L$, where $L = \pi/k \approx 280$ m in this example.

4. Discussion and concluding remarks

In this paper we have shown for the Stokes edge wave that the time rate of change of the total Lagrangian mean momentum is forced by the divergence of the total energy density $\partial E/\partial y$, independent of the bottom slope. This is exactly mid-way between the deep and shallow water values for ordinary surface waves (Longuet-Higgins and Stewart, 1960). This appears to be a novel result.

Furthermore, we have derived an analytical expression for the vertically-averaged Lagrangian drift velocity induced by the Stokes edge wave. This drift is composed of a Stokes drift component plus an Eulerian mean velocity, where the latter arises from the effect of bottom friction. Examples from moderately sloping beaches show that the mean Eulerian part of the velocity dominates, and are by far the largest contribution to the Lagrangian drift velocity, as seen from Figure 2. This has not been reported in the literature before.

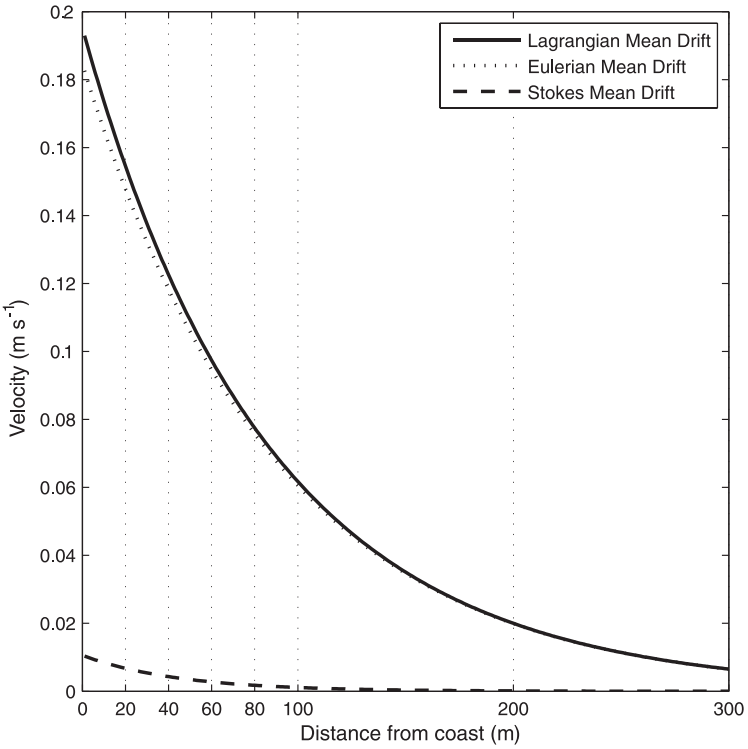

Figure 3. Same as in Figure 2, but with wave amplitude $a = 0.3$ m.

For given wave amplitude, the drift velocities increase with decreasing slope angle. In the example given by Kenyon (1969), the slope angle was 0.02 radians, yielding a Stokes drift at the shore of 15 cm s^{-1}. This is rather extreme. For a more reasonable slope like 0.1 radians, as in the present example, the Stokes drift at the shore becomes 0.1 cm s^{-1}, which is negligible, compared with the Eulerian mean component of about 6 cm s^{-1}, as seen from Figure 2. The contribution from the Stokes drift increases with increasing amplitude. This is obvious from Figure 3, where we have plotted the drift velocity components when the amplitude is 0.3 m, which is probably on the larger side for high-frequency edge waves. Still we must conclude that the Stokes drift contribution is negligibly small. The Stokes drift contribution also increases with decreasing value of the viscosity coefficient. However, even with a molecular viscosity coefficient ($\nu = 1.2 \times 10^{-6}$ m^2 s^{-1}) in this problem, which is highly unrealistic, the Stokes drift contribution would be smaller than the mean Eulerian flow.

The present approach does not resolve the viscous bottom boundary layer, so the results should not be used to assess the drift of heavy bottom sediments. However, it yields the vertically-averaged drift in the water column as function of the seaward distance. In practice, the maximum of this drift current occurs near the shore. We think that this drift may be of importance for the transport along the shore of biological material, pollutants, as well as light sediments in suspension. The Stokes edge wave and the associated drift

current can have either direction along a straight coast. This is important to keep in mind when we try to estimate the whereabouts of effluents released in the near-shore zone.

Acknowledgments. P. Ghaffari is indebted to the IOTWS Fellowship Program in Sea Level Science and Applications (UNESCO) for supporting a research visit to the Department of Geosciences, University of Oslo.

REFERENCES

Aida, I. 1967. Water level oscillations on the continental shelf in the vicinity of Miyagi-Enoshima. Bull. Earthquake Res. Inst., *45,* 61–78.

Apotsos, A., B. Raubenheimer, S. Elgar, R. T. Guza and J. Smith. 2007. Effect of wave rollers and bottom stress on wave setup. J. Geophys. Res., *112,* C02003, doi: 10.1029/2006JC003549.

Ardhuin, F. and A. D. Jenkins. 2006. On the interaction of surface waves and upper ocean turbulence. J. Phys. Oceanogr., *36,* 551–557.

Beardsley, R. C., H. Mofjeld, M. Wimbush, C. N. Flagg and J. A. Vermersch. 1977. Ocean tides and weather-induced bottom pressure fluctuations in the Middle Atlantic Bight. J. Geophys. Res., *82,* 3175–3182.

Boss, E., F. Gonzalez, K. Sakate and H. Mofjeld. 1995. Edge wave and non-trapped modes of the 25 April 1992 Cape Mendocino tsunami. Pure Appl. Geophys., *144,* 409–426.

Bowen, A. J. and R. T. Guza. 1978. Edge waves and surface beat. J. Geophys. Res., *83,* 1913–1920.

Bowen, A. J. and D. L. Inman. 1971. Edge waves and crescentic bars. J. Geophys. Res., *76,* 8662–8671.

Chapman, D. C. 1984. The generation of barotropic edge waves by deep-sea internal waves. J. Phys. Oceanogr., *14,* 1152–1158.

Dore, B. D. 1975. Wave-induced vorticity in free-surface boundary layers: application to mass transport in edge waves. J. Fluid Mech., *70,* 257–266.

Eckart, C. 1951. Surface waves on water of variable depth. Marine Physical Laboratory and Scripps Institute of Oceanography, Wave Rep. 100, Ref., 51–12, 99 pp.

Feddersen, F., E. L. Gallagher, R. T. Guza and S. Elgar. 2003. The drag coefficient, bottom roughness, and wave-breaking in the near shore. Coast. Eng., *48,* 189–195.

Fuller, J. D. and L. A. Mysalo. 1977. Edge waves in the presence of an irregular coastline. J. Phys. Oceanogr., *7,* 846–855.

Gallagher, B. 1971. Generation of surf beat by non-linear wave interactions. J. Fluid Mech., *49,* 1–20.

Galletta, V. And G. Vittori. 2004. Nonlinear effects on edge wave development. European J. Mechanics B/Fluids, *23,* 861–878.

Gaster, M. 1962. A note on the relation between temporally increasing and spatially increasing disturbances in hydrodynamic stability. J. Fluid Mech., *14,* 222–224.

Gjevik, B., E. Nøst and T. Straume. 1994. Model simulations of the tides in the Barents Sea. J. Geophysical Res., *99 (C2),* 3337–3350.

Golovachev, E. V., I. E. Kochergin and E. N. Pelinovsky. 1992. The effect of the Airy phase during the propagation of edge waves. J. Phys. Oceanogr., *3,* 1–7.

Holman, R. A. and A. J. Bowen. 1982. Bars, bumps, and holes: models for the generation of complex beach topography. J. Geophys. Res., *87 (C1),* 457–468.

Jenkins, A. D. 1989. The use of a wave prediction model for driving a near-surface current model. Deut. Hydrogr. Zeit., *43,* 133–149.

Kenyon, K. E. 1969. Note on Stokes' drift velocity for edge waves. J. Geophys. Res., *73,* 5533–5535.

Kurkin, A. and E. N. Pelinovsky. 2003. Shallow-water edge waves above an inclined bottom slowly varied in along-shore direction. European J. Mechanics B/Fluids, *22,* 305–316.

Lamb, Sir Horace. 1932. Hydrodynamics, Cambridge at the University Press, 738 pp.

LeBlond, P. H. and L. A. Mysak. 1978. Waves in the Ocean, Elsevier, 602 pp.

Longuet-Higgins, M. S. 1953. Mass transport in water waves. Phil. Trans. R. Soc. London, *A245,* 535–581.

Longuet-Higgins, M. S. and R. W. Stewart. 1960. Changes in the form of short gravity waves on long waves and tidal currents. J. Fluid Mech., *8,* 565–583.

Mei, C. C. 1973. A note on the averaged momentum balance in two-dimensional water waves. J. Mar. Res., *31,* 97–104.

Minzoni, A. A. and G. B. Whitham. 1977. On the excitation of edge waves on beaches. J. Fluid Mech., *79,* 273–281.

Mok, K. M. and H. Yeh. 1999. On mass transport of progressive edge waves. Phys. Fluids, *11,* 2906–2924.

Monserrat, S., I. Vilibic and A. B. Rabinovich. 2006. Meteotsunamis: atmospherically induced destructive ocean waves in the tsunami frequency band. Nat. Hazards Earth Syst. Sci., *6,* 1035–1051.

Munk, W. H. 1949. Surf beats. Trans. Amer. Geophys. Union, *30,* 849–854.

Munk, W. H., F. E. Snodegrass and G. Garrier. 1956. Edge waves on the continental shelf. Science, *123 (3187),* 127–132.

Nøst, E. 1994. Calculating tidal current profiles from vertically integrated models near the critical latitude in the Barents Sea. J. Geophys. Res., *99(C4),* 7885–7901.

Phillips, O. M. 1977. The Dynamics of the Upper Ocean, 2nd ed, Cambridge University Press, 336 pp.

Quevedo, E., A. Baquerizo, M. A. Losada and M. Ortega-Sanchez. 2008. Large-scale coastal features generated by atmospheric pulses and associated edge waves. Mar. Geol., *247,* 226–236.

Reid, R. O. 1958. Effect of Coriolis force on edge waves, 1. Investigation of the normal modes. J. Mar. Res., *16,* 109–144.

Starr, V. P. 1959. Hydrodynamical analogy to $E = mc^2$. Tellus, *11,* 135–138.

Stokes, G. G. 1846. Report on recent researches in hydrodynamics. Rep. 16th Brit. Assoc. Adv. Sci., 1–20. (See also Papers, *Vol. 1,* 157–187, Cambridge University Press, 1880)

—— On the theory of oscillatory waves. Trans. Cam. Phil. Soc., *8,* 441–455.

Ursell, F. 1952. Edge waves on a sloping beach. Proc. Roy. Soc. London, *A214,* 79–92.

Weber, J. E. H., G. Broström and Ø. Saetra. 2006. Eulerian versus Lagrangian approaches to the wave-induced transport in the upper ocean. J. Phys. Oceanogr., *36,* 2106–2117.

Weber, J. E. and A. Melsom. 1993. Transient ocean currents induced by wind and growing waves. J. Phys. Oceanogr., *23,* 193–206.

Yeh, H. 1985. Nonlinear progressive edge waves: their instability and evolution. J. Fluid Mech., *152,* 479–499.

Received: *15 September, 2008;* revised: *11 May, 2009.*

III

The DOI for this manuscript is doi: 10.1175/JPO-D-13-0171.1

Mass transport in the Stokes edge wave for constant arbitrary bottom slope in a rotating ocean

Peygham Ghaffari *
Department of Geosciences, University of Oslo, Oslo, Norway
Jan Erik H. Weber
Department of Geosciences, University of Oslo, Oslo, Norway

ABSTRACT

The Lagrangian mass transport in the Stokes surface edge wave is obtained from the vertically integrated equations of momentum and mass in a viscous rotating ocean, correct to second order in wave steepness. The analysis is valid for bottom slope angles β in the interval $0 < \beta \leq \pi/2$. Vertically-averaged drift currents are obtained by dividing the fluxes by the local depth. The Lagrangian mean current is composed of a Stokes drift (inherent in the waves) plus a mean Eulerian drift current. The latter arises as a balance between the radiation stresses, the Coriolis force, and bottom friction. Analytical solutions for the mean Eulerian current are obtained in the form of exponential integrals. The relative importance of the Stokes drift to the Eulerian current in their contribution to the Lagrangian drift velocity is investigated in detail. For given wavelength, the Eulerian current dominates for medium and large values of β, while for moderate and small β, the Stokes drift yields the main contribution to the Lagrangian drift. Since most natural beaches are characterized by moderate or small slopes, one may only calculate the Stokes drift in order to assess the mean drift of pollution and suspended material in the Stokes edge wave. The main future application of the results for large β appears to be for comparison with laboratory experiments in rotating tanks.

1. Introduction

In recent years the interest in coastally trapped waves; e.g. the Stokes edge wave, has risen considerably. This is particularly so because they have been shown to be of fundamental importance in the dynamics and the sedimentology of the near-shore zone through their interaction with ocean swell and surf to produce rip current patterns, beach cusps and crescentic bars (LeBlond and Mysak 1978). The non-linear mean mass transport in such waves has also been investigated, e.g. Weber and Ghaffari (2009) for a non-rotating ocean, where a comprehensive list of references to earlier works in a homogeneous ocean can be found. The edge wave problem has also been carried on to a stratified ocean (Greenspan 1970). A thorough discussion of the linear edge wave problem in a rotating ocean with continuous stratification can be found in Llewellyn Smith (2004). Finally, the nonlinear wave drift in interfacial edge waves in a rotating viscous ocean has been investigated by Weber and Stöylen (2011), using a shallow-water approach.

For a rotating ocean, Johns (1965) discovered that trapped edge waves with frequency ω are restricted to slopes such that $\cos\beta > f/\omega$, where f is the constant Coriolis parameter. In Johns' case the waves travelled northward along a western boundary. For edge waves propagating with the coast to the right in the Northern hemisphere, there is no restriction on the slope (Weber 2012). In the limit where the sloping bottom becomes a vertical wall, the edge wave becomes a geostrophically balanced Kelvin wave.

In the present study we focus on the mean Lagrangian mass transport induced by the Stokes edge wave. It is this transport that advects neutral tracers and bottom sediment in suspension along the shore in the region of wave trapping. In order to obtain a robust formulation, we consider the vertically integrated equations of momentum and mass, e.g. Phillips (1977), and derive the mean Lagrangian mass transport to second order in wave steepness. The vertically-averaged drift current is obtained by dividing the volume flux by the local depth. The total Lagrangian drift current can be written as the sum of the Stokes drift (Stokes 1847) and a mean Eulerian current; see e.g. Longuet-Higgins (1953). In the present paper the Eulerian current arises as a balance between the radiation stresses, the Coriolis force, and bottom friction. Earlier, Kenyon (1969) has considered the pure Stokes drift in inviscid non-rotating edge waves by applying the hydrostatic approximation, which is valid for small slope angles. However, the Stokes drift and the Eulerian mean current de-

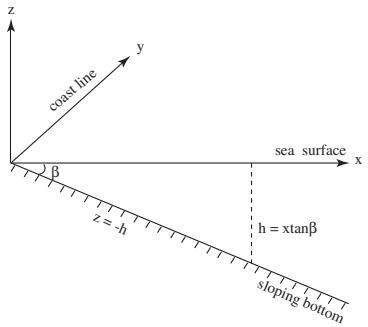

FIG. 1. Sketch depicting the coordinate system, with the surface and sloping bottom included.

pend on the slope angle in different ways, so we need a formulation that is valid for arbitrary slopes in order to determine their relative importance for given β to the Lagrangian drift current. This constitutes the main aim of the present paper.

2. Mathematical formulation

We consider trapped surface gravity waves in a homogeneous incompressible fluid with a linearly sloping bottom. The motion is described in a Cartesian system, where the x-axis is situated at the undisturbed surface and directed towards the semi-infinite sea, the y-axis is directed along the shore line, and the vertical z-axis is positive upwards; see the sketch in Fig. 1. The corresponding velocity components are (u, v, w). Furthermore, the pressure is p and the constant density is ρ. The bottom is given by $z = -h = -x\tan\beta$, where $\beta(\leq \pi/2)$ is the slope angle, and the free surface by $z = \eta$. At the free surface the pressure is constant. The system rotates about the z-axis with constant angular velocity $f/2$. We denote periodic wave variables by a tilde, and the mean flow (averaged over the wave period) by an over-bar. Mean horizontal volume fluxes $(\bar{U}, \bar{V})$ are defined by

$$\bar{U} = \overline{\int_{-h}^{\eta} u\, dz}, \qquad \bar{V} = \overline{\int_{-h}^{\eta} v\, dz}. \tag{1}$$

These are actually the Lagrangian fluxes, since we integrate between material boundaries (Phillips 1977; Weber et al. 2006). By neglecting the effect of friction in the vertical component of the momentum equation, Phillips (1977) found for the mean pressure, correct to second order in wave steepness, that

$$\frac{\bar{p}}{\rho} = g\,(\bar{\eta} - z) + \frac{\bar{p}_d}{\rho}. \tag{2}$$

Here $\bar{p}_d$ is the non-hydrostatic (dynamic) part given by

$$\frac{\bar{p}_d}{\rho} = -\overline{\tilde{w}^2} + \frac{\partial}{\partial x}\int_z^0 \overline{\tilde{u}\tilde{w}}\, d\xi + \frac{\partial}{\partial y}\int_z^0 \overline{\tilde{v}\tilde{w}}\, d\xi, \tag{3}$$

and g is the acceleration due to gravity. It is implicit here that the wave (tilde) quantities are represented by the real parts in a complex formulation. Integrating the governing equations in the vertical, and utilizing the full nonlinear boundary conditions at the free surface and the sloping bottom, we obtain for the mean quantities, correct to second order in wave steepness (Phillips 1977)

$$\begin{aligned}
&\frac{\partial \bar{U}}{\partial t} - f\bar{V} + gh\frac{\partial \bar{\eta}}{\partial x} = -\frac{\partial}{\partial x}\int_{-h}^{0} \frac{\bar{p}_d}{\rho}\, dz - \frac{g}{2}\frac{\partial}{\partial x}\overline{\tilde{\eta}^2} + \\
&\frac{\bar{p}_d(-h)}{\rho}\tan\beta - \frac{\partial}{\partial x}\int_{-h}^{0} \overline{\tilde{u}\tilde{u}}\, dz - \frac{\partial}{\partial y}\int_{-h}^{0} \overline{\tilde{u}\tilde{v}}\, dz - \tau_1, \\
&\frac{\partial \bar{V}}{\partial t} + f\bar{U} + gh\frac{\partial \bar{\eta}}{\partial y} = -\frac{\partial}{\partial y}\int_{-h}^{0} \frac{\bar{p}_d}{\rho}\, dz \\
&-\frac{g}{2}\frac{\partial}{\partial y}\overline{\tilde{\eta}^2} - \frac{\partial}{\partial x}\int_{-h}^{0} \overline{\tilde{u}\tilde{v}}\, dz - \frac{\partial}{\partial y}\int_{-h}^{0} \overline{\tilde{v}\tilde{v}}\, dz - \tau_2, \\
&\frac{\partial \bar{\eta}}{\partial t} = -\frac{\partial \bar{U}}{\partial x} - \frac{\partial \bar{V}}{\partial y}.
\end{aligned} \tag{4}$$

Here

$$\tau_1 \equiv \left.\frac{\bar{\tau}^{(x)}}{\rho}\right|_{-h}, \qquad \tau_2 \equiv \left.\frac{\bar{\tau}^{(y)}}{\rho}\right|_{-h}, \tag{5}$$

are the mean turbulent bottom stress components per unit density in the x and y-directions, respectively. Their explicit form will be specified later on.

As shown by Mei (1973) for the Stokes standing edge wave, the mean bottom pressure term in the x-momentum of (4), $\bar{p}_d(-h)\tan\beta/\rho$, which is missing from Phillips' derivation, must be present here; see also Weber and Ghaffari (2009).

3. Linear waves

In this problem the oscillatory wave motion is influenced by viscosity acting in thin boundary layers at the surface and at the bottom. Denoting the kinematic viscosity by ν, the boundary layer thickness δ in a non-rotating ocean becomes $\delta = (2\nu/|\omega|)^{1/2}$ (Longuet-Higgins 1953). In a turbulent ocean ν is the eddy viscosity, and may take different values in the top and bottom boundary layers. For shallow water waves of the tidal type, there are two bottom layers, $\delta = (2\nu/|\omega \pm f|)^{1/2}$, associated with the cyclonic and anticyclonic component of the solution (Sverdrup 1927). Within the top and bottom boundary layers

the wave velocity varies rapidly with height, while in the interior the variation is that of inviscid waves. The only effect of friction here is that the wave amplitude varies slowly in time or space due the boundary-condition coupling (no surface stress, no-slip bottom) with the boundary-layer solutions. In this analysis we assume that the boundary layers are thin, i.e. $\delta \ll h$. Hence, in the integrals of the wave forcing terms (with a tilde) in (4), the contributions from the boundary-layer parts of the wave velocity can be neglected, and we use the inviscid part of the solution (with a damped amplitude); see e.g. Weber et al. (2009). In shallow water with a no-slip bottom, the bottom boundary layer dominates in determining the damping rate. For a non-rotating ocean, this yields a temporal damping rate $(2\nu|\omega|)^{1/2}/(4h)$. In a deep ocean the corresponding damping rate becomes $2\nu k^2$, where k is the wave number. In both cases the correct attenuation of the interior motion is obtained by replacing the viscous term $\nu\nabla^2\tilde{\vec{u}}$ by $-r\tilde{\vec{u}}$ in the linearized momentum equation, where ∇ is the gradient operator and $\tilde{\vec{u}} = (\tilde{u}, \tilde{v}, \tilde{w})$ is the linear wave velocity in the interior. Here the friction coefficient r can be related to ν for the case in question. Classifications like deep-water or shallow-water depend on the value of λ/h, where λ is the wavelength. Hence, for a given wavelength, the Stokes edge wave at a certain distance offshore may be characterized as a shallow-water wave for small slope angles, while for large slopes the same wave may be a deep-water wave (here we investigate slope angles in the interval $0 < \beta \leq \pi/2$). We have therefore resorted to an averaging procedure for calculating the damping rate of such waves for all admissible β. A physically appealing and robust formulation is obtained through the calculation the total wave energy E and the total dissipation rate D in the trapped region. Then the damping rate is determined by $dE/dt = -D$; see e.g. Phillips (1977). We return to the detailed calculations in Section 4. By adopting the approach outlined above, the linearized equations for the damped interior wave motion become:

$$\begin{aligned} \tilde{u}_t - f\tilde{v} &= -\frac{1}{\rho}\tilde{p}_x - r\tilde{u}, \\ \tilde{v}_t + f\tilde{u} &= -\frac{1}{\rho}\tilde{p}_y - r\tilde{v}, \\ \tilde{w}_t &= -\frac{1}{\rho}\tilde{p}_z - g - r\tilde{w}, \end{aligned} \tag{6}$$

and

$$\tilde{u}_x + \tilde{v}_y + \tilde{w}_z = 0. \tag{7}$$

Here subscripts denote partial differentiation. The effect of friction on the wave motion is taken to be small. More precisely, we assume that

$$\frac{r}{|\omega|} \ll 1. \tag{8}$$

By applying the curl and the divergence on (6), utilizing (7), the velocity components are easily eliminated. We then find for $\tilde{p}$:

$$\left(\partial/\partial t + r\right)^2 \nabla^2\tilde{p} + f^2\tilde{p}_{zz} = 0. \tag{9}$$

We consider surface waves that are trapped at the coast, i.e.

$$\tilde{\eta} = \eta_0 \exp\left(-ax + i\left(\kappa y - \omega t\right)\right), \tag{10}$$

where $\Re\left(a\right) > 0$, and η_0 is an arbitrary constant. Furthermore, ω is the wave frequency and κ is the wave number in the y-direction (along the coast). The dynamic boundary condition in this problem becomes

$$\tilde{p} = p_0, \qquad z = \tilde{\eta}. \tag{11}$$

We then infer from (10) and (11) that the pressure in the linear case can be written (Johns 1965):

$$\tilde{p} = p_0 - \rho g z + \rho g \eta_0 \exp\left(-ax + bz + i\left(\kappa y - \omega t\right)\right), \tag{12}$$

where b is a complex parameter. Inserting (12) into (6), we obtain

$$\tilde{u} = \frac{g\eta_0\left(-ra + i\left(\omega a + f\kappa\right)\right)}{\omega^2 - f^2 + 2i\omega r} \exp\left(-ax + bz + i\left(\kappa y - \omega t\right)\right), \tag{13}$$

$$\tilde{v} = \frac{g\eta_0\left(\omega\kappa + fa + i\kappa r\right)}{\omega^2 - f^2 + 2i\omega r} \exp\left(-ax + bz + i\left(\kappa y - \omega t\right)\right), \tag{14}$$

$$\tilde{w} = -\frac{g\eta_0 b}{r - i\omega} \exp\left(-ax + bz + i\left(\kappa y - \omega t\right)\right). \tag{15}$$

The kinematic boundary conditions for the linear problem are

$$\tilde{w} = \tilde{\eta}_t, \qquad z = 0. \tag{16}$$

and

$$\tilde{w} = -\tilde{u}\tan\beta, \qquad z = -x\tan\beta \tag{17}$$

In this analysis we take that the frequency is ω real, while the wave number is complex, i.e. we consider spatially damped waves. Then we can write

$$\begin{aligned} \kappa &= k + i\alpha, \\ a &= a_r + ia_i, \\ b &= b_r + ib_i, \end{aligned} \tag{18}$$

where α is the spatial damping rate. Trapping at the coast requires $a_r > 0$. In this analysis the parameters α, a_i, b_i are related to the effect of friction. We show in Appendix A that they all are proportional to the small parameter r; see (8). Hence, in a non-dimensional formulation $k\alpha \ll 1$, $ka_i \ll 1$, $kb_i \ll 1$. In this problem we assume that the wave number k along the coast is given. The three complex equations (9), (16), and (17) are sufficient to determine the friction-independent parameters ω, a_r, b_r, and the small friction-related quantities α, a_i, b_i. In this calculation we neglect squares or products of the small quantities

r, α, a_i, b_i. The effects of rotation and friction will appear through the non-dimensional parameters Ω and R, defined by

$$\Omega = \frac{f}{\omega}, \qquad R = \frac{r}{\omega}, \tag{19}$$

where Ω is of order unity, and R is small, see (8). The calculations of ω, a_r, b_r and α, a_i, b_i are straightforward, but somewhat time consuming. Therefore, we defer the details to the Appendix A.

To calculate the mean quantities in (3) and (4), we need real values of our wave solutions. Defining the exponential decay q and the phase function θ by

$$\begin{aligned} q &= -a_r x - \alpha y + b_r z, \\ \theta &= -a_i x + k y + b_i z - \omega t, \end{aligned} \tag{20}$$

we can write the real part of the surface elevation

$$\tilde{\eta} = \eta_0 \exp q_0 \cos\theta_0, \tag{21}$$

where $q_0 = q|_{z=0}$, $\theta_0 = \theta|_{z=0}$. The real part of the pressure becomes

$$\tilde{p} = p_0 - \rho g z + \rho g \eta_0 \exp q \cos\theta. \tag{22}$$

The velocity components (13)–(15) can be simplified by using the expressions for α, a, b derived in the Appendix A. We obtain for the real parts after some algebra

$$\tilde{u} = -\frac{g k \eta_0 \cos\beta}{\omega\left(1 - \Omega\cos\beta\right)} \exp q \sin\theta, \tag{23}$$

$$\tilde{v} = \frac{g k \eta_0}{\omega\left(1 - \Omega\cos\beta\right)} \exp q \cos\theta, \tag{24}$$

$$\tilde{w} = \frac{g k \eta_0 \sin\beta}{\omega\left(1 - \Omega\cos\beta\right)} \exp q \sin\theta. \tag{25}$$

We note from (A16) that $1 - \Omega\cos\beta$ is always positive. It is easily seen from (23) and (25) that $\tilde{w} = -\tilde{u}\tan\beta$ for all q, θ, which shows that the wave motion in the Stokes edge wave occurs in planes parallel to the sloping bottom. This has been utilized by Weber (2012) to find exact solutions for the Stokes edge wave in a rotating inviscid ocean in Lagrangian coordinates.

4. The damping rate

As mentioned in Section 3, we use the formulation of Phillips (1977) to relate the friction coefficient r to the eddy viscosity ν. We find for the total mean energy density that

$$\begin{aligned} E &= \int_0^\infty \left\{ \int_{-h}^0 \overline{\frac{\rho}{2}\left(\tilde{u}^2 + \tilde{v}^2 + \tilde{w}^2\right)} dz + \rho g \overline{\int_0^{\tilde{\eta}} z\, dz} \right\} dx \\ &= \frac{\rho g \eta_0^2}{8k}\left[\frac{2 - \Omega\cos\beta}{\cos\beta - \Omega}\right] \exp\left(-2\alpha y\right). \end{aligned} \tag{26}$$

The total dissipation rate D in this problem is readily found to be

$$\begin{aligned} D &= \rho\nu \int_0^\infty \left\{ \int_{-h}^0 \left[\overline{\left(\frac{\partial\tilde{u}}{\partial x}\right)^2} + \overline{\left(\frac{\partial\tilde{u}}{\partial y}\right)^2} + \overline{\left(\frac{\partial\tilde{u}}{\partial z}\right)^2} \right] dz \right\} dx \\ &= \frac{\rho\nu g k \eta_0^2}{4}\left[\frac{2\left(1 - \Omega\cos\beta\right)^2 + \Omega^2\sin^2\beta}{\left(\cos\beta - \Omega\right)\left(1 - \Omega\cos\beta\right)^2}\right] \exp\left(-2\alpha y\right). \end{aligned} \tag{27}$$

Here ν is the bulk eddy viscosity in the fluid. For time damped waves we must have $dE/dt = -D$ (Phillips 1977). From Gaster (1962) we know that the transition from temporal damping to spatial damping is obtain through $d/dt \longrightarrow c_g d/dy$, were $c_g = d\omega/dk$ is the group velocity. Hence, for the present problem

$$c_g dE/dy = -D. \tag{28}$$

From (A15) we obtain that

$$c_g = \frac{g\sin\beta}{\omega\left(2 - \Omega\cos\beta\right)}. \tag{29}$$

Then, from (26)–(29), we find that the spatial attenuation coefficient is related to the eddy viscosity through

$$\alpha = \left(\frac{\nu k^3}{\omega}\right)\frac{\left(2\left(1 - \Omega\cos\beta\right)^2 + \Omega^2\sin^2\beta\right)}{\left(1 - \Omega\cos\beta\right)^3}. \tag{30}$$

Utilizing (A16), we find

$$\alpha = \frac{2\nu k^2 \omega}{g\sin\beta}\left[1 + \frac{1}{2}\left(\frac{f\omega}{gk}\right)^2\right]. \tag{31}$$

For the non-rotating case ($f = 0$), we recover the result $\alpha = 2\nu k^3/\omega$ from Weber and Ghaffari (2009). The friction coefficient for the linear problem is obtained from (31) and (A21):

$$r = 2\nu k^2\left[1 + \frac{1}{2}\left(\frac{f\omega}{gk}\right)^2\right]. \tag{32}$$

We note that in this case the friction coefficient is directly proportional to the eddy viscosity.

5. The mean flow

Utilizing (21)–(25), it is trivial to calculate the right-hand side of (3). In this problem we note that $\overline{\tilde{u}\tilde{v}} = 0$. Hence we can write the radiation stress components S_1 and S_2 in the x and y-directions, respectively by

$$S_1 = \int_{-h}^0 \frac{\bar{p}_d}{\rho} dz + \frac{g}{2}\overline{\tilde{\eta}^2} + \int_{-h}^0 \overline{\tilde{u}\tilde{u}} dz. \tag{33}$$

$$S_2 = \int_{-h}^{0} \frac{\bar{p}_d}{\rho} dz + \frac{g}{2}\overline{\tilde{\eta}^2} + \int_{-h}^{0} \overline{\tilde{v}\tilde{v}} dz. \tag{34}$$

Utilizing that here $\overline{\tilde{u}\tilde{u}} = \overline{\tilde{v}\tilde{v}}\cos^2\beta$, we can write S_1 as

$$S_1 = S_2 - \sin^2\beta \int_{-h}^{0} \overline{\tilde{v}\tilde{v}} dz. \tag{35}$$

Defining $\partial\bar{P}/\partial x = (\bar{p}_d(-h)\tan\beta)/\rho$, the total wave-forcing stress component S in the x-direction in (4) becomes

$$S = S_1 - \bar{P} = S_2 - \sin^2\beta \int_{-h}^{0} \overline{\tilde{v}\tilde{v}} dz - \bar{P}, \tag{36}$$

see e.g., Mei (1973). Utilizing (21)–(25), we find that the last two terms cancel exactly. Accordingly, we can write $S = S_2$, where

$$S = \frac{1}{4k\omega^2 \sin\beta}\left[\frac{gk\eta_0}{1-\Omega\cos\beta}\right]^2 \left[2kx\left(\cos\beta - \Omega\right)\sin^2\beta + \left(\sin^2\beta + \Omega\cos\beta\right)\left(1 - \Omega\cos\beta\right) - \left\{\Omega\left(1-\Omega\cos\beta\right)\cos\beta\right\} \exp\left(-2b_r x\tan\beta\right)\right] \exp\left(-2\alpha y - 2a_r x\right). \tag{37}$$

Hence, we find that the radiation stress component in the y-direction also forces the flow in the x-direction. In (37), a_r, b_r are given by (A10) and (A19), respectively. In these calculations we have neglected all terms proportional to $(\alpha/k)^2$, and higher orders. We note that for $\Omega = 0$, (37) reduces to

$$S = \left(\frac{g^2 k\eta_0^2 \sin\beta}{4\omega^2}\right)\left[2kx\cos\beta + 1\right]\exp\left(-2\alpha y - 2kx\cos\beta\right)$$

which is obtained from eqns. (12) and (13) of Weber and Ghaffari (2009).

The x-and y-components of the Lagrangian fluxes to second order in wave steepness then become

$$\begin{aligned} \frac{\partial\bar{U}}{\partial t} - f\bar{V} + gh\frac{\partial\bar{\eta}}{\partial x} &= -\frac{\partial S}{\partial x} - \tau_1, \\ \frac{\partial\bar{V}}{\partial t} + f\bar{U} + gh\frac{\partial\bar{\eta}}{\partial y} &= -\frac{\partial S}{\partial y} - \tau_2. \end{aligned} \tag{38}$$

It was demonstrated by Longuet-Higgins and Stewart (1960) that the radiation stress forcing would be $\frac{1}{2}\left(-\partial E/\partial y\right)$ for deep water waves and $\frac{3}{2}\left(-\partial E/\partial y\right)$ for shallow water waves in a non-rotating ocean of constant depth. As pointed out by Weber and Stöylen (2011), the relation between the radiation stress components and the total wave energy depends on the wave type. For example, for Poincaré waves in a shallow rotating ocean there is a velocity component in the cross-wave direction that contributes to the wave energy, but not to the radiation stress. Then, in this case $S_2 = \frac{1}{2}\left(3 - f^2/\omega^2\right)E/\rho$. Since $|\omega| > |f|$ for Poincaré waves, we have that $S_2 < 3E/\left(2\rho\right)$ for this particular shallow water problem. For the Stokes edge wave we also have a cross-wave velocity component, since the particles move in planes parallel to the sloping bottom. We therefore would expect a relation that differs from that of Longuet-Higgins and Stewart. In addition, the wave amplitude here decays exponentially in the cross-shore direction. It is therefore natural to consider the wave energy in the entire trapped region, i.e. (26). From (26) and (37) it is easy to see that

$$\langle S\rangle = E/\rho, \tag{39}$$

where $\langle S\rangle = \int_0^\infty S dx$. This is exactly the same result as obtained by Weber and Ghaffari (2009) for the non-rotating Stokes edge wave, demonstrating that it is not the rotation, but the sloping bottom that yields a value which is in between the deep and shallow water values of Longuet-Higgins and Stewart (1960).

Following Longuet-Higgins (1953), the Stokes drift to second order in wave steepness for this problem is easily obtained from the linear wave solutions (23)–(25).

By definition

$$\begin{aligned} \bar{v}_S &= \overline{\left(\int \tilde{u}dt\right)\tilde{v}_x} + \overline{\left(\int \tilde{v}dt\right)\tilde{v}_y} + \overline{\left(\int \tilde{w}dt\right)\tilde{v}_z} \\ &= \frac{\omega k\eta_0^2}{\sin^2\beta}\exp\left(-2a_r x + 2b_r z - 2\alpha y\right). \end{aligned} \tag{40}$$

We note that the Stokes drift has a maximum at the shoreline. Here

$$\bar{v}_S(x=0,\, z=0) = \frac{\omega k\eta_0^2}{\sin^2\beta}\exp(-2\alpha y). \tag{41}$$

The alongshore Stokes flux for this problem becomes:

$$\begin{aligned} \bar{V}_S &= \int_{-h}^{0}\left[\overline{\left(\int \tilde{u}dt\right)\tilde{v}_x} + \overline{\left(\int \tilde{v}dt\right)\tilde{v}_y} + \overline{\left(\int \tilde{w}dt\right)\tilde{v}_z}\right]dz \\ &= \frac{1}{2\omega\left(1-\Omega\cos\beta\right)\sin\beta}\left[\frac{gk\eta_0}{\omega}\right]^2\left[1 - \exp\left(-2b_r x\tan\beta\right)\right]\exp\left(-2a_r x - 2\alpha y\right). \end{aligned} \tag{42}$$

In the vertical wall limit ($\beta = \pi/2$) we must treat this problem with some care. Now, from (A15), (A10) and (A19) we find $\omega^2 = gk$, $a_r = -fk/\omega$, $b_r = k$. The Stokes drift (40) then becomes

$$\bar{v}_S(\beta = \pi/2) = \omega k\eta_0^2 \exp\left(\frac{2fk}{\omega}x + 2kz - 2\alpha y\right). \tag{43}$$

We note that trapping now requires $\omega < 0$. The resulting wave motion is a coastal Kelvin wave propagating with the coast (the vertical wall) to the right in the northern

hemisphere. The trapping distance is the baroclinic Rossby radius ($|\omega|/k/f$). In this limit the Stokes flux must be obtained from (43) by integrating in the vertical from minus infinity to zero, yielding

$$\bar{V}_s(\beta = \pi/2) = \frac{1}{2}\omega\eta_0^2 \exp\left(\frac{2kf}{\omega}x - 2\alpha y\right). \qquad (44)$$

For slope angles in the interval $0 < \beta < \pi/2$ we can apply (42) and expand the exponential functions for small x. We then obtain

$$\bar{V}_S = \frac{k\omega\eta_0^2}{\sin\beta\cos\beta}x\exp(-2\alpha y). \qquad (45)$$

In this paper we shall work with depth-averaged drift velocities. We define the depth-averaged Stokes drift by

$$\hat{v}_S = \frac{\bar{V}_S}{h}, \qquad (46)$$

where $h = x\tan\beta$, and $\bar{V}_S$ is given by (42). By comparison with (41), we note from (45) and (46) that $\hat{v}_S$ yields the correct Stokes drift at the shoreline, i.e.

$$\hat{v}_S(x=0) = \bar{v}_S(x=0,\, z=0) = v_{S0}\exp(-2\alpha y), \qquad (47)$$

where

$$v_{S0} = \frac{k\omega\eta_0^2}{\sin^2\beta}. \qquad (48)$$

The Stokes drift is basically related to the net particle motion in inviscid waves, and there is no Stokes drift in the direction perpendicular to the wave propagation direction. In the presence of friction in the fluid, Longuet-Higgins formulation yields a small drift in the cross-wave direction, being proportional to the small friction coefficient. This part is inseparable from the frictional mean Eulerian current in the cross-wave direction, into which it can be included; see e.g., Weber and Drivdal (2012). Hence, we take that the Stokes flux in the x-direction, $\bar{U}_S$, is zero. Thus, the total wave momentum in the trapped region becomes from (42)

$$M_w = \rho\int_0^\infty \bar{V}_S dx = \frac{\rho g\eta_0^2}{4\omega\left(\cos\beta - \Omega\right)}\exp\left(-2\alpha y\right). \qquad (49)$$

We note that for $\beta = \pi/2$, the total wave momentum could equally well have been obtain by integrating (44) for the vertical wall limit. By comparing with the total energy density (26), we note that for this problem $E = M_w c^*$, where $c^* = (2 - \Omega\cos\beta)\,\omega/(2k)$. In a non-rotating ocean $f = 0$, c^* becomes equal to the phase speed $c = \omega/k$, so then $E = M_w c$; see e.g. Starr (1959).

When we express the solutions as expansions in power series after the wave steepness as a small parameter, which is the basis of the derivation of the flux equations (4), we must require that the second order Stokes velocity must be considerably smaller than the linear velocity field, which in turn must be smaller than the phase speed of the wave. From (24) and (48), utilizing (A16), the conditions $\mid \hat{v}_S \mid \ll \mid \tilde{v} \mid$ and $\mid \tilde{v} \mid \ll \mid \omega \mid /k$ both lead to

$$k\eta_0 \ll \sin\beta. \qquad (50)$$

This condition must be fulfilled for the Stokes edge wave when applying the non-linear theory for calculating wave-induced mean drift currents in practical cases.

6. The steady Eulerian mass transport

As first shown by Longuet-Higgins (1953), the mean wave-induced Lagrangian velocity could be written as a sum of the Stokes drift and a mean Eulerian current, where the latter depended on friction. Hence, the mean Eulerian volume fluxes in this problem can be written

$$\begin{aligned} \bar{U}_E &= \bar{U}_L, \\ \bar{V}_E &= \bar{V}_L - \bar{V}_S. \end{aligned} \qquad (51)$$

where the Lagrangian fluxes $\left(\bar{U}_L,\, \bar{V}_L\right)$ are equal to $\left(\bar{U},\, \bar{V}\right)$ in (38), and $\left(\bar{V}_S\right)$ is given by (40).

For a given wave field (and Stokes drift) at $t = 0$, as assumed in this paper, the solutions for $\bar{U}_E$ and $\bar{V}_E$ will contain a transient part. For a complete solution we must state the appropriate initial conditions for this flow, which we really do not know. But as time moves on, the solution will equilibrate towards a steady state, independent of the initial conditions. We here focus on this asymptotic solution for large t. The steady state governing momentum equations (38) then reduce to

$$\begin{aligned} -f\bar{V}_E + gh\frac{\partial\bar{\eta}}{\partial x} &= f\bar{V}_S - \frac{\partial S}{\partial x} - \tau_1, \\ f\bar{U}_E + gh\frac{\partial\bar{\eta}}{\partial y} &= -\frac{\partial S}{\partial y} - \tau_2. \end{aligned} \qquad (52)$$

In the steady case, utilizing (51), the integrated continuity equation in (4) becomes

$$\frac{\partial\bar{U}_E}{\partial x} + \frac{\partial\bar{V}_E}{\partial y} = -\frac{\partial\bar{V}_S}{\partial y}. \qquad (53)$$

At the coast we must have

$$\bar{U}_E\big|_{x=0} = 0. \qquad (54)$$

We consider mean flow trapped over the slope. Then, we must require

$$\bar{V}_E \to 0, \qquad x \to \infty. \qquad (55)$$

The mean motion in the cross-shore direction is small, and we neglect the effect of friction in this direction. Then, from the curl of (52)

$$g\bar{\eta}_y\tan\beta = -\tau_{2x}. \qquad (56)$$

Assuming that $\bar{\eta} \propto \exp(-2\alpha y)$, we find that

$$gh\bar{\eta}_x = \frac{1}{2\alpha} x\tau_{2xx}. \tag{57}$$

Then by inserting into the cross-shore component of (52):

$$x\tau_{2xx} - 2\alpha f\bar{V}_E = 2\alpha\left(f\bar{V}_S - S_x\right). \tag{58}$$

In a vertically integrated approach the friction term in (58) must be modelled. Often one uses a formulation where the bottom stress is proportional to the square of the mean velocity in the problem. A similar effect is obtained by defining a friction coefficient that is proportional to the bottom drag coefficient times a characteristic velocity; see e.g. Nöst (1994). Then the bottom friction becomes linear in the mean velocity, which simplifies the analysis. We use this approach here, and take

$$\tau_2 = K\hat{v}_E. \tag{59}$$

where $\hat{v}_E = \bar{V}_E/h$ is the vertically averaged Eulerian velocity, and K is a constant friction coefficient (dimension velocity). The present approach separates the decay of wave momentum from the frictional influence on the mean flow as suggested in the literature (Jenkins 1989; Weber and Melsom 1993; Ardhuin and Jenkins 2006). Using (59), and introducing the vertically averaged velocities, we find from (58) when $x \neq 0$:

$$\hat{v}_{Exx} - \frac{2\alpha\tan\beta}{K}\hat{v}_E = \frac{2\alpha}{K}\left[(f\tan\beta)\,\hat{v}_S - \frac{1}{x}S_x\right]. \tag{60}$$

Applying (54), the y-component of (52) at the coast reduces to

$$\tau_2 = 2\alpha S, \qquad x = 0. \tag{61}$$

Then, utilizing (37) and (59), (61) yields the boundary condition

$$\hat{v}_E = v_{E0}\exp(-2\alpha y), \qquad x = 0, \tag{62}$$

where

$$v_{E0} = \frac{\alpha g\eta_0^2}{2K}. \tag{63}$$

Using (31), we find

$$v_{E0} = \frac{\nu k}{K}\left(\frac{k\omega\eta_0^2}{\sin\beta}\right)\left[1 + \frac{1}{2}\left(\frac{f\omega}{gk}\right)^2\right]. \tag{64}$$

Furthermore, for trapped mean motion, we must require

$$\hat{v}_E \to 0, \qquad x \to \infty. \tag{65}$$

In (64) the ratio $\nu k/K$ expresses the balance between the forcing from the wave field (through the radiation stress) and the bottom stress on the mean flow. This ratio may vary numerically for various wave conditions, but from a physical balance point of view, its magnitude should be of order unity.

We now introduce a non-dimensional alongshore Eulerian drift velocity $Q_E(x)$ by

$$Q_E = \frac{\hat{v}_E}{v_{E0}\exp(-2\alpha y)}. \tag{66}$$

We also define a non-dimensional cross-shore coordinate $X = 2a_r x$. The governing equation (60) then becomes

$$Q_E'' - \gamma^2 Q_E = \exp(-X) + \frac{1}{X}\left[F_1\exp(-X) + F_2(-\sigma X)\right], \tag{67}$$

where the primes denote differentiation with respect to X. The boundary conditions are

$$\begin{aligned} Q_E &= 1, \qquad X = 0, \\ Q_E &\to 0, \qquad X \to \infty. \end{aligned} \tag{68}$$

In (67) we have defined

$$\gamma^2 = \frac{\alpha f\tan\beta}{2Kk^2}\left[\frac{1-\Omega\cos\beta}{\cos\beta-\Omega}\right]^2 \tag{69}$$

and

$$\sigma = \frac{1-\Omega\cos\beta}{(\cos\beta-\Omega)\cos\beta}. \tag{70}$$

Utilizing (37) and (40), we find that the coefficients in (67) can be written

$$\begin{aligned} F_1 &= \frac{\Omega\left(1-2\Omega\cos\beta+\cos^2\beta\right)}{(\cos\beta-\Omega)\sin^2\beta}, \\ F_2 &= -\frac{2\Omega\left(1-\Omega\cos\beta\right)}{(\cos\beta-\Omega)\sin^2\beta}. \end{aligned} \tag{71}$$

Before attempting to solve (67), we observe the following: To have solutions that are trapped over the slope in a rotating ocean ($f > 0$), we must require that the complementary part of the solution has an exponential behaviour, i.e. that $\gamma^2 > 0$. For $\omega > 0$, $\alpha > 0$, and β in the range $0 < \beta < \beta^*$, i.e. waves propagating with the coast to the left in the northern hemisphere, this is fine. But for waves propagating with the coast to the right, we have $\omega < 0$, $\alpha < 0$, and hence $\gamma^2 < 0$. This yields a sinusoidal complementary part with no seaward limitation. Hence, for the damped Stokes edge wave that propagates with the coast to the right, the induced Stokes drift is trapped over the slope (since the primary wave field is trapped), but the frictionally induced mean Eulerian current is not. Accordingly, there is no steady trapped solution to the Eulerian drift problem induced by such waves. Any transient behaviour will not be pursued here. When the effect of the earth's rotation can be neglected ($f = 0$), then $\gamma = 0$, and we have trapping of the Eulerian flow also when $\omega < 0$. The details

concerning the solution of (67) have been deferred to the Appendix B.

We introduce the non-dimensional average Stokes drift velocity Q_S from (46) and (63) by

$$Q_S = \frac{\hat{v}_S}{v_{E0}\exp(-2\alpha y)} = \frac{2Kk^2(\cos\beta-\Omega)\cos\beta}{\alpha\omega(1-\Omega\cos\beta)\sin^3\beta}\frac{1}{X}\left[\exp(-X)-\exp(-\sigma X)\right]. \quad (72)$$

The expression for Q_E is given by (B10). The vertically-averaged non-dimensional Lagrangian drift velocity Q_L thus becomes

$$Q_L = Q_E + Q_S. \quad (73)$$

7. Results

a. General discussion

In order to quantify the derived wave-induced mean currents, we must assess the values of the physical parameters in this problem. For the modelling of tidal currents in the Barents Sea a typical value of the eddy viscosity is $\nu = 10^{-3}\mathrm{m}^2\,\mathrm{s}^{-1}$ (Nöst 1994). At a sloping beach, eddy viscosity estimates are higher by a factor of 10 to 50 (Apotsos et al. 2007), mainly due to turbulence induced by breaking waves. Without specifying the source of turbulence, which is outside the scope of this paper, it seems reasonable to take $\nu = 1-5\times10^{-2}\,\mathrm{m}^2\mathrm{s}^{-1}$ in quantifying the drift induced by trapped waves, see Mei et al. (1998). By specifying the eddy-viscosity ν that acts to dampen the linear wave field, we obtain the friction coefficient r and the spatial wave attenuation coefficient α from (32) and (A21) for prescribed wavelength and bottom slope. As explained in the previous section, the relation between the linear friction coefficient K and the bottom drag coefficient c_B for the mean flow can be approximated as $K = c_B v_B$, where v_B is a typical near-bottom mean velocity (Gjevik et al. 1994; Nöst 1994).

The bottom drag coefficient depends on the seabed conditions, e.g. the presence of ripples (Longuet-Higgins 2005). Very close to the bottom in shallow waters the mean horizontal stresses are partly used to accelerate sediment particles that are kept in suspension by the oscillating wave motion. This part of the stress is not felt by the water column just above the rippled bed. The effect of the sediment transport must be reflected in the value of the bottom drag coefficient. For a corrugated bed $c_B = 0.1$ appears to be an appropriate value for short waves (Longuet-Higgins 2005). For longer waves and deeper waters, c_B will be considerably smaller, typically $c_B \sim 10^{-3}$; see Gjevik et al. (1994); Nöst (1994). Taking $v_B \sim 10^{-2}\,\mathrm{ms}^{-1}$, we obtain that $K \sim 10^{-3}\,\mathrm{ms}^{-1}$ and $K \sim 10^{-5}\,\mathrm{ms}^{-1}$ in the short and long wave limit, respectively.

In discussing the general properties of the solutions, we take that the wavelength $\lambda = 2\pi/k$ is 1 km,and use

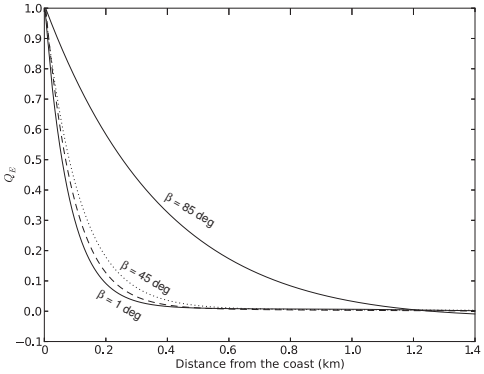

FIG. 2. Non-dimensional mean Eulerian current for $\lambda = 1\,\mathrm{km}$ and $\beta = 1°$ (thin solid line), $\beta = 30°$ (dashed line), $\beta = 45°$ (dotted line), $\beta = 85°$ (thick solid line) as a function of the seaward coordinate.

$f = 1.2\times10^{-4}\,\mathrm{s}^{-1}$. For waves travelling with the coast to the left ($\omega > 0$), the critical slope angle (A18) becomes $\beta^* \approx 89.9°$, which is very close to the vertical wall limit. Hence, in practice, the admissible slopes in this example belong to the interval $0 < \beta < \pi/2$. In this case $\Omega = f/\omega = 3.7\times10^{-3}$, so the effect of the earth's rotation can be neglected. Then in the solution (72) for the Stokes drift $\sigma = 1/\cos^2\beta > 1$. Furthermore, in this example we have taken $\nu = 1\times10^{-2}\,\mathrm{m}^{-2}\mathrm{s}^{-1}$ and $K = 10^{-5}\,\mathrm{ms}^{-1}$ according to the discussion above.

In Fig. (2) we have displayed Q_E from (B10) for various values of the bottom slope ($\beta = 1°, 30°, 45°, 85°$). We note from the figure that larger slope angles means wider trapping region. If we compare with the Stokes drift in (72), which varies over the shelf as $(\exp(-X)-\exp(-\sigma X))/(\sigma-1)$, where X is non-dimensional, we find that this is very close to the variation of Q_E in Fig. (2) for small and moderate angles.

Although the spatial variation over the shelf for Q_E and Q_S is not very different for small and moderate slopes, this is not so for the maximum current values at the shoreline, which depends very much on the slope angle. In fact, by forming the ratio between the mean Eulerian current and the Stokes drift at the shore, we find from (48) and (64):

$$d = \frac{v_{E0}}{v_{S0}} = \frac{\nu k}{K}\sin\beta\left[1+\frac{1}{2}\left(\frac{f\omega}{gk}\right)^2\right]. \quad (74)$$

We note immediately that increasing values of f act to favour v_{E0}. However, for the wavelengths considered here, the last term in the parenthesis is negligible. Then the relative strength between v_{E0} and v_{S0} depends on friction and wave slope. We have argued before that for the frictional influence, there should be a balance so $\nu k/K$ should

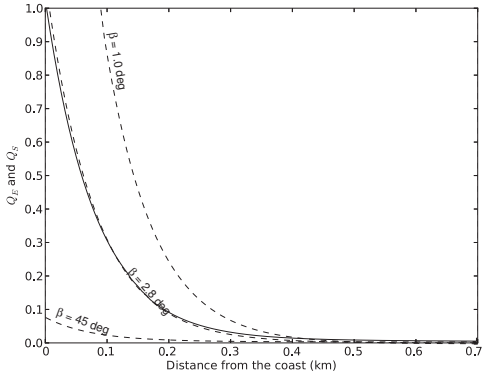

FIG. 3. Non-dimensional Eulerian mean current Q_E for $\beta = 2.8°$ (solid line) and non-dimensional Stokes drift current Q_S (broken line) as a functions of the seaward coordinate. Here $\lambda = 1\,\mathrm{km}$, and β varies from 1° to 45°.

be of order unity. In the present example this ratio is 6.3. Hence, in (74), the slope angle is the crucial parameter. In Fig. (3) we have plotted the non-dimensional currents Q_E and Q_S for various values of the slope angle. As noted from Fig. (2), the spatial variation of Q_S is nearly the same for small and moderate slopes. In the figure we have chosen $Q_E\,(\beta = 2.8°)$. We see from Fig. (3) that for small angles, the Stokes drift dominates in this example. The currents are comparable in magnitude for $\beta = 2.8°$. We have considered $\beta = 1°$ as the lower limit. This is the slope used by Kenyon (1969) in his calculations of the Stokes drift.

In reality, bottom slopes are not very steep. In fact, in the practical examples we consider at the end of this section, they are less than 10 degrees. However, our calculations for $\omega > 0$ are valid for all $\beta < \beta^*$, see (A18). Such solutions may be convenient for comparison with experiments in wave tanks, where for laboratory model purposes, a steep slope may be advantageous.

In practice, there is a limitation to the wave number in this problem. The theory of the Stokes edge wave requires a constant bottom slope, but in real cases the (approximately linear) bottom profile may change quite abruptly at a distance L from the shore line. To have trapped waves within the constant slope region, we then must require

$$a_r L > 1 \tag{75}$$

where a_r is given by (A10). For not too long waves, and normal small slope angles, we can use the non-rotating limit. Then (75) reduces to

$$k > L^{-1} \tag{76}$$

b. Specific case studies

The existence of edge waves on natural shorelines has been inferred from the periodic spacing of rip currents (Bowen and Inman 1969) and forming of beach cusps and crescentic bars (Bowen and Inman 1971). The theory developed here is valid for slope angles in the interval $0 < \beta \leq \pi/2$. However, in natural environments most beach slopes are quite gentle. In order to relate our theoretical results to the natural environment, we consider two different locations where we find short and long waves, respectively. First, Slapton Beach (Huntley 1973), and second Lake Michigan (Donn and Ewing 1956). In both cases the depth increases slowly from the coast. As noted before, in such cases the Stokes drift is comparable to or exceeds the mean Eulerian current.

For short waves we used the field observation at Slapton Beach by Huntley (1973). They demonstrated that the observed wave field at 0.1 Hz did represent a Stokes standing edge wave. For such high frequency waves the effect of the earth's rotation can safely be neglected. The field survey yielded a wavelength λ of about 30 m. The beach profile in the inter-tidal zone could be approximated by the expression $h = h_0(1 - \exp(-ax))$, where $h_0 = 7.05\,\mathrm{m}$, and $a = 0.03\,\mathrm{m}^{-1}$. Since the trapping distance in this case is about 30 m from the shore line, we take the equivalent linear slope angle to be $\beta = 10°$. Based on the observed alongshore and cross-shore velocities, we estimate a wave amplitude of 0.2 m for the standing edge wave. It seems reasonable to use half the standing wave amplitude for our progressive wave, i.e., we take $\eta_0 = 0.1\,\mathrm{m}$ in our calculations. With these parameters the Stokes drift at coast becomes $v_{S0} = 4.4\,\mathrm{cm\,s}^{-1}$. We use the eddy viscosity and bottom drag coefficient values for short waves ($\nu = 3 \times 10^{-2}\,\mathrm{m^2\,s^{-1}}$, $K = 10^{-3}\,\mathrm{ms^{-1}}$). From (63), we find $v_{E0} = 4.8\,\mathrm{cm\,s}^{-1}$, which is comparable to the Stokes drift. Here $\nu k/K = 6.3$. In this example $k\eta_0 = 0.02$ and $\sin\beta = 0.17$, which fulfils (50) quite well.

Our second example is from Lake Michigan. The disastrous surge in 1954 and the resulting gravity waves, were explained by Ewing et al. (1954) as a resonant coupling between a fast-moving atmospheric squall line and the Stokes edge wave. They utilized the theory of edge waves (Stokes 1846; Ursell 1951, 1952), in order to explain the long-period high waves (periods of order 100 min) which were correlated with atmospheric pressure-jumps (Donn and Ewing 1956). In Lake Michigan the Stokes edge wave propagated with the coast to the right ($\omega < 0$), so formally the wave-induced Eulerian current is not trapped to the coast in the presence of rotation. However, the effect of rotation is negligible for edge waves with periods of order 100 min in this body of water ($f\omega/gk = 2.7 \times 10^{-3} \ll 1$). In the Lake Michigan, storm surge data from Waukegan yields a typical wave period of 109 min, and a wave amplitude of about

3 m. A typical slope angle for Lake Michigan is $\beta = 0.17°$, and $f = 1.01 \times 10^{-4}$ s. Then, with $\omega = -9.61 \times 10^{-4}\,\mathrm{s}^{-1}$, we find that $v_{S0} = -3.4\,\mathrm{cm\,s}^{-1}$. Using $\nu = 3 \times 10^{-2}\,\mathrm{m^2 s}^{-1}$ and $K = 10^{-5}\,\mathrm{ms}^{-1}$, we obtain $v_{E0} \sim 10^{-3}\,\mathrm{cm\,s}^{-1}$, so the Stokes drift dominates completely in this example. Despite the large amplitude, the Stokes drift is quite moderate. This is because the waves are quite long. With a period 109 min, we find for the wave number in this problem that $k = 3.5 \times 10^{-5}\,\mathrm{m}^{-1}$, then $\lambda \sim 180$ km. Finally, in this example $\eta_0 k = 1.1 \times 10^{-4}$, and $\sin\beta = 3.0 \times 10^{-3}$ which fulfils (50) very well.

8. Discussion and concluding remarks

In a previous paper (Weber and Ghaffari 2009), we investigated the nonlinear mass transport in the Stokes surface edge wave in an unbounded non-rotating ocean. This was done by applying an Eulerian description of motion, and expanding the solution in series after wave steepness as a small parameter. Utilizing almost same approach, we have derived an analytical expression for the vertically-averaged Lagrangian drift velocity induced by the Stokes edge wave in a rotating ocean. This drift is composed of a Stokes drift component plus an Eulerian mean velocity, where the former is inherent in the wave motion and latter arises from the effect of friction. Similar to the non-rotating case, the time rate of change of the total Lagrangian momentum flux in the wave direction (y-direction) is forced by the divergence of the total energy density $-\partial E/\partial y$, which is mid-way between the deep and shallow water values for non-rotating surface waves in an ocean of constant depth (Longuet-Higgins and Stewart 1960). The main aim of this paper has been to quantify the contributions of the Stokes and Eulerian mean currents to the vertically-averaged mean Lagrangian drift velocity.

The calculations show that the Stokes drift and the Eulerian current attain their maximum values at the shore line. For wave motion in which the earth's rotation become important, we find that this effect tends to enhance the mean Eulerian current for given bottom slope. When we can neglect the effect of the earth's rotation, the relative importance of the mean Eulerian current to the Stokes drift can be expressed as $v_{E0}/v_{S0} = \nu k \sin\beta/K$, demonstrating that, for given wavelength, the Stokes drift tends to dominate for small bottom slopes. This is a novel result, and shows that for most natural beach or coastal situations it is sufficient to calculate the Stokes drift in the Stokes edge wave in order to obtain the main part of the Lagrangian alongshore drift velocity.

The transfer of mean momentum from damped waves to mean Eulerian currents follows from the fundamental concept of conservation of total momentum. To balance the Eulerian flow, friction is needed. In the present paper we use a simple linear model for the bottom friction that does this task. Since ocean flows are turbulent, we have to use eddy values for the friction coefficients. Although these coefficients are assessed from physical reasoning, their values can never be established with absolute certainty. Despite those objections, it is of fundamental importance to include the wave-induced mean Eulerian current as a part of the total drift current. However, natural beach or coastal slopes are rather gentle. As demonstrated in the present paper for the Stokes edge wave, this tends to enhance the Stokes drift relative to the mean Eulerian current in their contribution to the mean Lagrangian drift velocity. The Stokes drift follows basically from inviscid wave theory, and easy to calculate. For steeper slopes, the importance of the Eulerian current increases, as noted from our example from Slapton Beach. Since steep slopes are easily made in the laboratory, our analytical results for large bottom slope may be of importance for comparisons with (future) laboratory experiments in rotating tanks. In conclusion, we find that the Stokes edge wave induces a mean drift velocity that may be of importance for the alongshore transport of pollutants, biological materials and suspended loads.

Acknowledgments.

This paper was written as part of the BIOWAVE project funded by The Research Council of Norway, Project No. 196438/S40. Financial support is gratefully acknowledged.

APPENDIX A

Determination of Parameters

Inserting from (10) and (11) into the boundary condition (16), we obtain

$$\omega^2 + i\omega r - gb = 0. \tag{A1}$$

To lowest order in the small quantities, we obtain from the real and imaginary parts

$$\omega^2 = gb_r, \tag{A2}$$

$$b_i = \frac{\omega r}{g} = Rb_r. \tag{A3}$$

By inserting (12) into (9), utilizing (A3), we obtain from the real and imaginary parts, respectively,

$$\left(1 - \Omega^2\right) b_r^2 + a_r^2 - k^2 = 0, \tag{A4}$$

$$-k\alpha + a_r a_i + Rb_r^2 = 0. \tag{A5}$$

Inserting (13) and (15) into the boundary condition (17), again utilizing (A3), we obtain

$$\left(1 - \Omega^2\right) b_r - (\Omega k + a_r)\tan\beta = 0, \tag{A6}$$

$$\left(1-\Omega^2\right)(\Omega\alpha + a_i + Ra_r) - 2R\,(\Omega k + a_r) = 0. \quad \text{(A7)}$$

From (A4) and (A6) we find expressions for a_r and b_r. In particular

$$a_r = \frac{k}{1-\Omega^2\cos^2\beta}\left(-\Omega + \Omega\cos^2\beta \pm \left(1-\Omega^2\right)\cos\beta\right), \quad \text{(A8)}$$

For two signs in (A8), we apply the identities

$$\begin{aligned} -\Omega + \Omega\cos^2\beta + \cos\beta - \Omega^2\cos\beta = \\ (\cos\beta - \Omega)\,(\Omega\cos\beta + 1)\,, \\ -\Omega + \Omega\cos^2\beta - \cos\beta + \Omega^2\cos\beta = \\ -(\cos\beta + \Omega)\,(\Omega\cos\beta - 1)\,. \end{aligned} \quad \text{(A9)}$$

Hence, for the plus and minus signs, respectively

$$a_{r+} = \frac{k\,(\cos\beta - \Omega)}{1-\Omega\cos\beta}, \quad \text{(A10)}$$

$$a_{r-} = -\frac{k\,(\Omega + \cos\beta)}{1+\Omega\cos\beta}. \quad \text{(A11)}$$

In this study we take that $f > 0$ (Northern hemisphere), so the sign of $\Omega = f/\omega$ depends solely on ω. As noted in connection with (10), trapping at the coast requires $a_r > 0$. To have trapped waves that travel in both directions along the coast ($\Omega > 0,\ \Omega < 0$), we must exclude the a_{r-} solution. This is shown as follows: From (A2) and (A6) we have a general expression for a_r:

$$a_r = \frac{(1-\Omega^2)\omega^2}{g\tan\beta} - k\Omega. \quad \text{(A12)}$$

By taking $a_{r-} = a_r$ we readily obtain

$$\omega^2 + (f\cos\beta)\,\omega + gk\sin\beta = 0. \quad \text{(A13)}$$

Hence

$$1 + \Omega\cos\beta = -\frac{gk\sin\beta}{\omega^2} < 0. \quad \text{(A14)}$$

Obviously, this can not be true for $\Omega > 0$. For $\Omega < 0$, (A14) requires $\Omega < -1/\cos\beta$. But in this case we note from (A11) that $a_{r-} < 0$. Hence a_{r-} must be discarded for $\Omega > 0$ as well as for $\Omega < 0$. For $a_{r+} = a_r$ in (A12), we obtain

$$\omega^2 - (f\cos\beta)\omega - gk\sin\beta = 0. \quad \text{(A15)}$$

Now

$$1 - \Omega\cos\beta = \frac{gk\sin\beta}{\omega^2} > 0. \quad \text{(A16)}$$

In this case we note that $a_{r+} > 0$ for all $\omega < 0$ (waves with the coast to the right). For waves with the coast to the left ($\omega > 0$), we see from (A10) that trapping requires $\cos\beta > \Omega$ (Johns 1965). The correct dispersion relation for this problem is (A15), leading to the two roots (Weber 2012)

$$\begin{aligned} \omega_1 &= \frac{1}{2}f\cos\beta + \frac{1}{2}\left(f^2\cos^2\beta + 4gk\sin\beta\right)^{1/2} > 0, \\ \omega_2 &= \frac{1}{2}f\cos\beta - \frac{1}{2}\left(f^2\cos^2\beta + 4gk\sin\beta\right)^{1/2} < 0. \end{aligned} \quad \text{(A17)}$$

Here ω_1 is the frequency of a trapped wave that travels with the coast to the left, while ω_2 represents a wave travelling with the coast to the right in the northern hemisphere. The limiting trapping angle β^* for ω_1 is given in Weber (2012). Inserting $\cos\beta^* = f/\omega_1\,(\beta^*)$ into (A15), yields

$$\beta^* = \arcsin\left(\left(\delta^2+1\right)^{1/2} - \delta\right), \quad \text{(A18)}$$

where $\delta = f^2/(2gk)$. For $\beta > \beta^*$, there exists no trapped wave traveling with the coast to the left. With $a_r = a_{r+}$, we obtain from (A6):

$$b_r = \frac{k\sin\beta}{1-\Omega\cos\beta}. \quad \text{(A19)}$$

Then, from (A3):

$$b_i = \frac{Rk\sin\beta}{1-\Omega\cos\beta}. \quad \text{(A20)}$$

By combining (A5) and (A7), we obtain for the damping rate

$$\alpha = \frac{Rk}{1-\Omega\cos\beta}. \quad \text{(A21)}$$

Since $1 - \Omega_{1,2}\cos\beta > 0$, see (A16), we note that $\alpha > 0$ for $\omega = \omega_1 > 0$, and $\alpha < 0$ for $\omega = \omega_2 < 0$. In the latter case the propagation is in the negative y-direction, and we consider damped trapped waves in the interval $-\infty < y \leq 0$, i.e. $\exp(-\alpha y) \leq 1$ in (21)–(25). Finally, by inserting into (A5), we obtain

$$a_i = \frac{Rk\cos\beta}{1-\Omega\cos\beta}. \quad \text{(A22)}$$

APPENDIX B

Analytical solution for the mean Eulerian flow

An analytical solution of (67) can be found in terms of exponential integrals; see e.g. Weber and Stöylen (2011). Assuming that γ^2 is a positive constant, the complementary part $Q_E^{(c)}$ of the solution becomes

$$Q_E^{(c)} = C_1\exp(\gamma X) + C_2\exp(-\gamma X)\,, \quad \text{(B1)}$$

where C_1, C_2 are constants. Applying the variation of parameters method, we write the particular solution $Q_E^{(p)}$ as

$$Q_E^{(p)} = m_1(X)\exp(\gamma X) + m_2(X)\exp(-\gamma X)\,. \quad \text{(B2)}$$

The functions m_1, m_2 are then determined by

$$\begin{aligned} m_1^{'} \exp(\gamma X) + m_2^{'} \exp(-\gamma X) &= 0, \\ \gamma m_1^{'} \exp(\gamma X) - \gamma m_2^{'} \exp(-\gamma X) &= G(X), \end{aligned} \tag{B3}$$

where

$$G(X) = \exp(-X) + \frac{1}{X}\left[F_1 \exp(-X) + F_2 \exp(-\sigma X)\right]. \tag{B4}$$

The Wronskian in this problem is -2γ . Hence we find

$$\begin{aligned} m_1 &= \frac{1}{2\gamma} \int \exp(-\gamma X)\, G(X)\, dX, \\ m_2 &= -\frac{1}{2\gamma} \int \exp(\gamma X)\, G(X)\, dX. \end{aligned} \tag{B5}$$

We can express the terms with a singularity at $X = 0$ as exponential integrals Ei, e.g. Abramowitz and Stegun (1972). By definition

$$E_i(X) = \int_{-\infty}^{X} \frac{\exp(t)}{t} dt. \tag{B6}$$

Hence (B2) can be written

$$\begin{aligned} Q_E^{(p)} = &-\frac{1}{\gamma^2 - 1} \exp(-X) \\ &+ \frac{F_1}{2\gamma}\left[\exp(\gamma X)\, E_i(-(\gamma+1)X) - \exp(-\gamma X)\, E_i((\gamma-1)X)\right] \\ &+ \frac{F_2}{2\gamma}\left[\exp(\gamma X)\, E_i(-(\gamma+\sigma)X) - \exp(-\gamma X)\, E_i((\gamma-\sigma)X)\right]. \end{aligned} \tag{B7}$$

For the special case $\gamma = 1$, m_1 in (B5) becomes unaltered, while

$$m_2 = -\frac{1}{2}\left[X + F_1 \ln X + F_2 E_i((1-\sigma)X)\right]. \tag{B8}$$

To satisfy the boundary conditions (68), we must require for the complementary solution (B1) that

$$\begin{aligned} C_1 &= 0, \\ C_2 &= 1 - Q_E^{(p)}\Big|_{x \to 0^+} \end{aligned} \tag{B9}$$

Inserting from (B7) and (B9), the complete solution for the non-dimensional mean Eulerian drift velocity becomes

$$Q_E = C_2 \exp(-\gamma X) + Q_E^{(p)} \tag{B10}$$

REFERENCES

Abramowitz, M. and I. Stegun, (Eds.) , 1972: *Handbook of mathematical functions with formulas, graphs, and Mathematical tables.* National Bureau of Standards Applied Mathematics Series. 55.

Apotsos, A., B. Raubenheimer, S. Elgar, R. T. Guza, and J. A. Smith, 2007: Effects of wave rollers and bottom stress on wave setup. *J. Geophys. Res.*, **112 (C2)**, C02 003.

Ardhuin, F. and A. D. Jenkins, 2006: On the interaction of surface waves and upper ocean turbulence. *J. Phys. Oceanogr.*, **36 (3)**, 551–557.

Bowen, A. J. and D. L. Inman, 1969: Rip currents: 2. laboratory and field observations. *J. Geophys. Res.*, **74 (23)**, 5479–5490.

Bowen, A. J. and D. L. Inman, 1971: Edge waves and crescentic bars. *J. Geophys. Res.*, **76 (36)**, 8662–8671.

Donn, W. L. and M. Ewing, 1956: Stokes' edge waves in lake michigan. *Science*, **124 (3234)**, 1238–1242.

Ewing, M., F. Press, and W. L. Donn, 1954: An explanation of the lake michigan wave of 26 june 1954. *Science*, **120 (3122)**, 684–686.

Gaster, M., 1962: A note on the relation between temporally-increasing and spatially-increasing disturbances in hydrodynamic stability. *Journal of Fluid Mechanics*, **14 (02)**, 222–224.

Gjevik, B., E. Nøst, and T. Straume, 1994: Model simulations of the tides in the barents sea. *J. Geophys. Res.*, **99 (C2)**, 3337–3350.

Greenspan, H. P., 1970: A note on edge waves in a stratified fluid. *Stud. Appl. Maths.*, **49**, 381–388.

Huntley, A. J., D. A. & Bowen, 1973: Field observations of edge waves. *Nature*, **243**, 160–162.

Jenkins, A. D., 1989: The use of a wave prediction model for driving a near-surface current model. *Deutsch. Hydrogr. Z.*, **42 (3-6)**, 133–149.

Johns, B., 1965: Fundamental mode edge waves over a steeply sloping shelf. *J. Mar. Res.*, **23**, 200–206.

Kenyon, K. E., 1969: Note on stokes' drift velocity for edge waves. *J. Geophys. Res.*, **74 (23)**, 5533–5535.

Lamb, S. H., 1932: *Hydrodynamics.* Sixth edition ed., Cambridge at the University Press, 738 pp.

LeBlond, P. H. and L. A. Mysak, 1978: *Waves in the ocean.* Elsevier Oceanography Series, 20. Elsevier, Amsterdam, 602 pp.

Llewellyn Smith, S. G., 2004: Stratified rotating edge waves. *Journal of Fluid Mechanics*, **498**, 161–170.

Longuet-Higgins, M. S., 1953: Mass transport in water waves. *Phil. Trans. R. Soc. London*, **A245**, 535–581.

Longuet-Higgins, M. S., 2005: On wave set-up in shoaling water with a rough sea bed. *Journal of Fluid Mechanics*, **527**, 217–234.

Longuet-Higgins, M. S. and R. W. Stewart, 1960: Changes in the form of short gravity waves on long waves and tidal currents. *Journal of Fluid Mechanics*, **8 (04)**, 565–583.

Mei, C. C., 1973: A note on the averaged momentum balance in two-dimensional water waves. *J. Mar. Res.*, **31 (2)**, 97–104.

Mei, C. C., C. Chian, and F. Ye, 1998: Transport and resuspension of fine particles in a tidal boundary layer near a small peninsula. *J. Phys. Oceanogr.*, **28 (11)**, 2313–2331.

Nöst, E., 1994: Calculating tidal current profiles from vertically integrated models near the critical latitude in the barents sea. *J. Geophys. Res.*, **99 (C4)**, 7885–7901.

Phillips, O. M., 1977: *The Dynamics of the Upper Ocean*. 2d ed., Cambridge University Press, 336 pp.

Starr, V. P., 1959: Hydrodynamical analogy to e = m c2. *Tellus*, **11 (1)**, 135–138.

Stokes, G. G., 1846: Report on recent researches in hydrodynamics. *Rep. 16th Brit. Assoc. Adv. Sci.*, 1–20. (See also Papers, vol. 1, pp. 157–187. Cambridge University Press, 1880).

Stokes, G. G., 1847: On the theory of oscillatory waves. *Trans. Cam. Phil. Soc.*, **8**, 441–455.

Sverdrup, H. U., 1927: *Dynamic of Tides on the North Siberian Shelf. Results from the Maud expedition.* Oslo, – pp.

Ursell, F., 1951: Trapping modes in the theory of surface waves. *Mathematical Proceedings of the Cambridge Philosophical Society*, **47 (02)**, 347–358.

Ursell, F., 1952: Edge waves on a sloping beach. *Proceedings of the Royal Society of London*, **A214 (02)**, 79.

Weber, J. E. H., 2012: A note on trapped gerstner waves. *J. Geophys. Res.*, **117 (C3)**, 30–48.

Weber, J. E. H., G. Broström, and Ø. Saetra, 2006: Eulerian versus lagrangian approaches to the wave-induced transport in the upper ocean. *J. Phys. Oceanogr.*, **36**, 2106–2117.

Weber, J. E. H., K. H. Christensen, and C. Denamiel, 2009: Wave-induced setup of the mean surface over a sloping beach. *Continental Shelf Research*, **29 (11-12)**, 1448–1453.

Weber, J. E. H. and M. Drivdal, 2012: Radiation stress and mean drift in continental shelf waves. *Cont. Shelf Res.*, **35**, 108–116.

Weber, J. E. H. and P. Ghaffari, 2009: Mass transport in the stokes edge wave. *J. Mar. Res.*, **67**, 213–224.

Weber, J. E. H. and A. Melsom, 1993: Transient ocean currents induced by wind and growing waves. *J. Phys. Oceanogr.*, **23 (2)**, 193–206.

Weber, J. E. H. and E. Stöylen, 2011: Mean drift velocity in the stokes interfacial edge wave. *J. Geophys. Res.*, **116 (C4)**, C04002, URL `http://dx.doi.org/10.1029/2010JC006619`.

IV

ARTICLE IN PRESS

European Journal of Mechanics B/Fluids ▮ (▮▮▮▮) ▮▮–▮▮

Contents lists available at ScienceDirect

European Journal of Mechanics B/Fluids

journal homepage: www.elsevier.com/locate/ejmflu

Mass transport in internal coastal Kelvin waves

Jan Erik H. Weber*, Peygham Ghaffari

Department of Geosciences, University of Oslo, Norway

HIGHLIGHTS

- The Stokes and mean Eulerian drifts are trapped to the coast.
- The non-linear transports yield a jet-like flow along the southern Caspian coast.
- While the Stokes flux is zero, the Eulerian flux is not.
- The wave-induced drift may contribute to the mean circulation in the Caspian Sea.

ARTICLE INFO

Article history:
Available online xxxx

Keywords:
Internal coastal Kelvin waves
Lagrangian mass transport
Eulerian mean current
Stokes drift
The Caspian Sea

ABSTRACT

We investigate theoretically the mass transport in internal coastal Kelvin waves by integrating the horizontal momentum equations in the vertical. Applying a perturbation method, the time-averaged Lagrangian horizontal fluxes are determined to second order in wave steepness. The linear wave field is expanded in the vertical using orthogonal functions. Due to the orthogonality property of these functions, formulae for the non-linear Stokes drift and the mean vertically-averaged Eulerian transport driven by the radiation stress can be derived for arbitrary vertical variation of the Brunt–Väisälä frequency N. For values of N typical of the thermocline in the Caspian Sea, the calculation of the non-linear transports yields a jet-like mean flow along the coast, limited in the off-shore direction by the internal Rossby radius. It is suggested that this wave-induced mean drift may contribute to the mean circulation in the Caspian Sea.

1. Introduction

Most bodies of water at mid and lower latitudes have a pronounced vertical stratification. Together with the presence of a relatively straight coastline, this stratification may support internal Kelvin waves, being trapped in the region between the coast and the internal Rossby radius. For a small sea, like the Caspian Sea, with negligible tidal forcing, and a typical length scale of less than 1000 km, internal waves appear to be generated by temporal/spatial variations of the meso-scale wind field. In the south-western part of the Caspian Sea, we find a strong thermocline around 60 m depth [1], which is much less than the total depth of the basin. To discuss the dynamics of such regions, a reduced-gravity model is often applied [2,3]. In this approach there are two layers of constant density, where the upper is thin and active, and the lower is very deep and passive with negligible velocity. Then, by replacing the acceleration due to gravity by the reduced gravity, the interfacial Kelvin wave can be obtained directly by analogy with the barotropic wave. However, the reduced-gravity model filters out higher baroclinic modes, and will not be used here. In addition, it yields an erroneous result for the Stokes drift, as shown in [4].

The main focus of the present study is the mean drift induced by internal coastal Kelvin waves. Such waves possess mean momentum, and hence induce a Stokes drift. In addition, since the waves are damped due to friction, they will generate a mean Eulerian flow. For spatially damped waves, this baroclinic flow is driven by the radiation stress in the waves. This theme has been thoroughly discussed for barotropic flows by Longuet-Higgins and Stewart [5]. It has also been studied for interfacial coastal Kelvin waves in a reduced gravity context [6]. We here consider this effect in the continuously stratified case. This application appears to be novel.

The rest of this paper is organized as follows: in the Section 2 we state the basic assumptions and the governing equations, while in the Appendix we consider linear internal coastal Kelvin waves. In Section 3 we derive the Stokes drift in internal Kelvin waves, and in Section 4 we apply the results to the Caspian Sea. The mean vertically-averaged Eulerian velocity is derived in Section 5, while Section 6 contains a discussion and some concluding remarks.

* Corresponding author. Tel.: +47 22855826.
E-mail address: j.e.weber@geo.uio.no (J.E.H. Weber).

http://dx.doi.org/10.1016/j.euromechflu.2014.02.006
0997-7546/

Please cite this article in press as: J.E.H. Weber, P. Ghaffari, Mass transport in internal coastal Kelvin waves, European Journal of Mechanics B/Fluids (2014), http://dx.doi.org/10.1016/j.euromechflu.2014.02.006

2. Basic assumptions and governing equations

We consider a viscous ocean of constant depth H, and we chose a Cartesian coordinate system (x, y, z) such that the origin is situated at the undisturbed sea surface, the x-axis is directed along the coast, the y-axis is positive towards the sea, and the z-axis is directed vertically upwards. The respective unit vectors are $(\vec{i}, \vec{j}, \vec{k})$. The reference system rotates about the vertical axis with angular velocity $(f/2)$, where f is the constant Coriolis parameter. Furthermore, we use an Eulerian description of motion, which means that all dependent variables are functions of x, y, z and time t. We take that the horizontal scale of the motion is so large compared to the depth that we can make the hydrostatic approximation in the vertical. Furthermore, we apply the Boussinesq approximation for the density ρ. We also take that the density of an individual fluid particle is conserved. The governing equations for this problem then become

$$\frac{\partial \vec{v}_h}{\partial t} + \vec{v} \cdot \nabla \vec{v}_h = -f\vec{k} \times \vec{v}_h - \frac{1}{\rho_r}\nabla_h p + \frac{\partial}{\partial z}\left[\frac{\vec{\tau}_h}{\rho_r}\right], \tag{1}$$

$$\frac{\partial p}{\partial z} = -\rho g, \tag{2}$$

$$\frac{\partial \rho}{\partial t} + \vec{v} \cdot \nabla \rho = 0, \tag{3}$$

$$\nabla \cdot \vec{v} = 0. \tag{4}$$

Here $\vec{v} = (u, v, w)$ is the velocity vector, p is the pressure, subscript h means horizontal values, and $\vec{\tau}_h = (\tau^{(x)}, \tau^{(y)})$ is the turbulent stress in the horizontal direction. Furthermore, ρ_r is a constant reference density, and g the acceleration due to gravity. We take that there is no forcing from the atmosphere in this problem, i.e. at the surface: $\tau_s^{(x)} = \tau_s^{(y)} = p_s = 0$. The surface is material and given by $z = \eta(x, y, t)$. Integrating our governing equations from the horizontal bottom to the moving surface, we obtain equations for the horizontal Lagrangian volume transport (U_L, V_L) in the fluid:

$$\frac{\partial U_L}{\partial t} - fV_L = -\frac{1}{\rho_r}\frac{\partial}{\partial x}\int_{-H}^{\eta} p\,dz - \frac{\partial}{\partial x}\int_{-H}^{\eta} u^2 dz - \frac{\partial}{\partial y}\int_{-H}^{\eta} uv\,dz - \frac{\tau_B^{(x)}}{\rho_r}, \tag{5}$$

$$\frac{\partial V_L}{\partial t} + fU_L = -\frac{1}{\rho_r}\frac{\partial}{\partial y}\int_{-H}^{\eta} p\,dz - \frac{\partial}{\partial x}\int_{-H}^{\eta} uv\,dz - \frac{\partial}{\partial y}\int_{-H}^{\eta} v^2 dz - \frac{\tau_B^{(y)}}{\rho_r}, \tag{6}$$

where we have defined

$$U_L = \int_{-H}^{\eta} u\,dz, \qquad V_L = \int_{-H}^{\eta} v\,dz. \tag{7}$$

Furthermore, $(\tau_B^{(x)}, \tau_B^{(y)})$ are the turbulent bottom stresses.

In principle we expand our solutions in series after the wave steepness as a small parameter (although we retain our dimensional variables). The first order (linear) wave solution will be marked by a tilde, while to second order we consider averages over the wave period. Such (non-linear) quantities will be marked by an over-bar.

We consider trapped internal waves propagating along the x-axis. The waves result from small perturbations from a state of rest characterized by a horizontally-uniform stable stratification $\rho_0(z)$. We take that the velocity in the y-direction vanishes identically, characterizing the Kelvin wave. Introducing the vertical displacement $\xi(x, y, z, t)$ of the isopycnals from their original horizontal position, linear theory yields $\partial\tilde{\xi}/\partial t = \tilde{w}$, where the tilde is used to mark linear perturbation quantities. The linearized system of equations for internal coastal Kelvin waves can then be written from (1) to (4):

$$\begin{aligned}
&\frac{\partial \tilde{u}}{\partial t} = -\frac{1}{\rho_r}\frac{\partial \tilde{p}}{\partial x} + \frac{\partial}{\partial z}\left[\frac{\tilde{\tau}^{(x)}}{\rho_r}\right],\\
&f\tilde{u} = -\frac{1}{\rho_r}\frac{\partial \tilde{p}}{\partial y},\\
&\frac{\partial \tilde{p}}{\partial z} = -\rho_r N^2 \tilde{\xi},\\
&\frac{\partial \tilde{u}}{\partial x} = -\frac{\partial^2 \tilde{\xi}}{\partial z \partial t}.
\end{aligned} \tag{8}$$

Here N is the Brunt–Väisälä frequency defined by

$$N^2 = -\frac{g}{\rho_r}\frac{d\rho_0(z)}{dz}. \tag{9}$$

The variables may be separated into normal modes [7], and we refer to [8] for details. For didactic reasons we give a short account of the wave solutions in the Appendix.

In summary, letting real parts represent the physical solution, we have from the Appendix:

$$\tilde{\xi} = \sum_{n=1}^{\infty} \xi_n(x, y, t)\phi_n(z), \qquad \tilde{u} = \sum_{n=1}^{\infty} u_n(x, y, t)\phi_n'(z), \tag{10}$$

where ϕ_n is given by (A.2), and

$$\xi_n = A_n \exp\left(-\alpha_n x - a_n^{-1} y\right)\cos\left(k_n x + l_n y - \omega t\right), \tag{11}$$

$$u_n = c_n A_n \exp\left(-\alpha_n x - a_n^{-1} y\right)\left[\cos\left(k_n x + l_n y - \omega t\right) + \frac{\alpha_n}{k_n}\sin\left(k_n x + l_n y - \omega t\right)\right].$$

As for temporally damped waves [9], we note that the lines of constant phase for spatially damped coastal Kelvin waves are straight lines slanting backwards. In principle, the displacement amplitudes $A_1, A_2, A_3 \ldots$ must be determined from field observations, or from analytical/numerical model runs with appropriate forcing.

3. The Stokes drift

As first shown by Stokes [10], periodic waves possess non-zero mean wave momentum, leading to a net drift of particles in the fluid. This mean drift is referred to as the Stokes drift, and is basically related to the inviscid part of the wave field, eventually modified by a slow temporal or spatial viscous decay of wave amplitude. To second order in wave steepness the Stokes drift in the x-direction can be expressed by the Eulerian wave field [11]:

$$\bar{u}_s = \overline{\left(\int \tilde{u}dt\right)\frac{\partial \tilde{u}}{\partial x}} + \overline{\left(\int \tilde{v}dt\right)\frac{\partial \tilde{u}}{\partial y}} + \overline{\left(\int \tilde{w}dt\right)\frac{\partial \tilde{u}}{\partial z}}, \tag{12}$$

where the over-bar denotes average over one wave period $T = 2\pi/\omega$. In the present problem $\tilde{v} = 0$, and $\tilde{w} = \tilde{\xi}_t$. Hence, from (10) and (11) for internal Kelvin waves:

$$\bar{u}_s = \frac{1}{2}\sum_{n=1}^{\infty} c_n A_n^2 \left(\left(\phi_n'\right)^2 + \phi_n \phi_n''\right)\exp\left(-2\alpha_n x - 2a_n^{-1} y\right). \tag{13}$$

The expression (13) is valid for arbitrary $N(z)$. Inserting from (A.2), we obtain that

$$\bar{u}_s = \frac{1}{2}\sum_{n=1}^{\infty} c_n A_n^2 \left(\left(\phi_n'\right)^2 - \frac{N^2}{c_n^2}\phi_n^2\right)\exp\left(-2\alpha_n x - 2a_n^{-1} y\right). \tag{14}$$

Please cite this article in press as: J.E.H. Weber, P. Ghaffari, Mass transport in internal coastal Kelvin waves, European Journal of Mechanics B/Fluids (2014), http://dx.doi.org/10.1016/j.euromechflu.2014.02.006

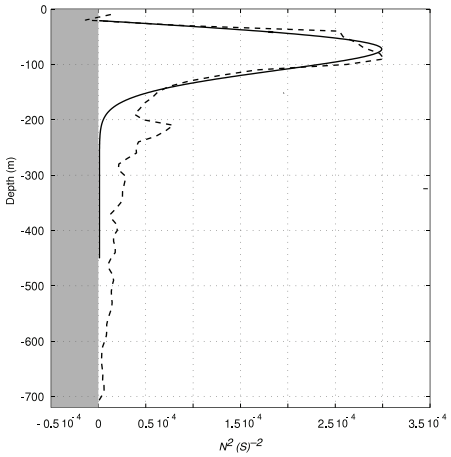

Fig. 1. N^2 versus depth. Solid line from (16), and dashed line from observations.

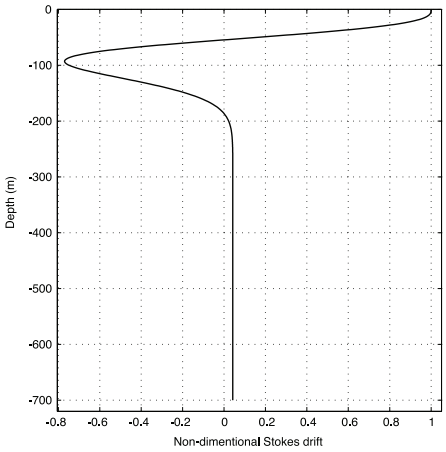

Fig. 2. Non-dimensional Stokes drift ($\bar{u}_{s1}/u_0$) at the coast for the first baroclinic mode in the Caspian Sea as function of depth.

Since the second term in (14) is always negative, we realize that the Stokes drift component for the mode in question must be negative at the z-level where the horizontal wave velocity is zero. In fact, by integration in the vertical, and application of the boundary conditions (A.3), we find for the associated Stokes volume flux for internal Kelvin waves; see e.g. [4] that

$$\bar{U}_s = \int_{-H}^{0} \bar{u}_s dz = 0. \tag{15}$$

This is an important result that will be used later on when we consider the total Lagrangian transport induced by these waves.

4. Application to the Caspian Sea

As an example, we consider the Caspian Sea. In order to obtain the eigenvalues c_1, c_2, c_3 etc., we must prescribe $N(z)$ in this body of water. The measurements by Ghaffari et al. [1] suggest that we can take

$$N^2 = N_0^2 \left[-\frac{az}{H_0}\right] \exp\left[-\frac{b^2 z^2}{2H_0^2}\right], \tag{16}$$

where a and b are dimensionless constants, and where $a = b\exp(1/2)$. For the maximum value of N^2 at $z = -H_0/b$, we take $N_0^2 = 3\times 10^{-4}\ \mathrm{s}^{-2}$. Using $H_0 = 120$ m and $b = 2$ in (16), we obtain a spatial distribution of N^2 much like that reported in [1]; see Fig. 1.

Introducing $z = H_0\hat{z}$, (A.2) and (A.3) become

$$\frac{d^2\phi_n}{d\hat{z}^2} + R_n^2 F(\hat{z})\,\phi_n = 0, \tag{17}$$

$$\phi_n = 0, \qquad \hat{z} = -h, 0 \tag{18}$$

where $h = H/H_0$, and

$$R_n^2 = \frac{H_0^2 N_0^2}{c_n^2}, \tag{19}$$

$$F(z) = -a\hat{z}\exp\left(-\frac{b^2\hat{z}^2}{2}\right).$$

This eigenvalue problem is easily solved by a simple shooting procedure. Using $H = 700$ m we find for the lowest eigenvalue that $R_1 = 1.71$. From (19) we then obtain $c_1 = 1.21\ \mathrm{m\ s}^{-1}$. The next eigenvalues become $R_2 = 4.61$ and $R_3 = 7.46$, yielding $c_2 = 0.45\ \mathrm{m\ s}^{-1}$ and $c_3 = 0.28\ \mathrm{m\ s}^{-1}$ for the second and third baroclinic mode, respectively.

According to [12], for a fairly sharp thermocline, a substantial fraction of the total energy resides in the first mode. It is therefore particularly interesting to calculate the Stokes drift for this mode. The numerically obtained eigenfunction $\phi_1(z)$ is then inserted into (14). In Fig. 2 we have plotted the non-dimensional Stokes drift $\bar{u}_{s1}/u_0$ at the coast as a function of the depth, where

$$u_0 = \frac{c_1 A_1^2}{2H_0^2}. \tag{20}$$

We note that the Stokes drift has its largest positive value at the surface, while it attains its largest negative value $z = -90$ m; close to where N^2 has its maximum. This is a typical behavior for the first mode internal wave, and is discussed more thoroughly in [4]. The depth profile fulfills the no-flux condition (15).

In dimensional terms, the value of the depicted Stokes drift (1. mode) for variable N in Fig. 2 should be multiplied by (20). In order to assess the vertical displacement amplitude A_1, we consider some temperature measurements over the shelf break at the location in the south-western part of the Caspian Sea described in [1]. The depicted temperature variations in Fig. 3 are from November–December, 2004, at a fixed position off the coast when the summer thermocline still prevails. We note a period between 4 and 5 days for the depicted oscillations. From the power spectrum in Fig. 4 we note a marked peak at 4.7 days, which fits well with the observations in Fig. 3.

In addition, we note from Fig. 4 that the along-shore velocity is much larger than the cross-shore velocity, indicating the presence of internal Kelvin waves. However, it is difficult to decide whether this is internal wave mode 1 or 2. At this station the sensors were basically positioned within the thermocline. Hence, the isotherm displacements could be detected, while the resolution of the vertical structure of the currents was not sufficient for determining the modal structure. We therefore use these observations only as an indication of the typical isotherm displacement amplitude we may expect in this region associated with internal Kelvin waves. In this case we find amplitudes of about 30 m. As pointed out by Phillips [12], a substantial fraction of the total energy

Please cite this article in press as: J.E.H. Weber, P. Ghaffari, Mass transport in internal coastal Kelvin waves, European Journal of Mechanics B/Fluids (2014), http://dx.doi.org/10.1016/j.euromechflu.2014.02.006

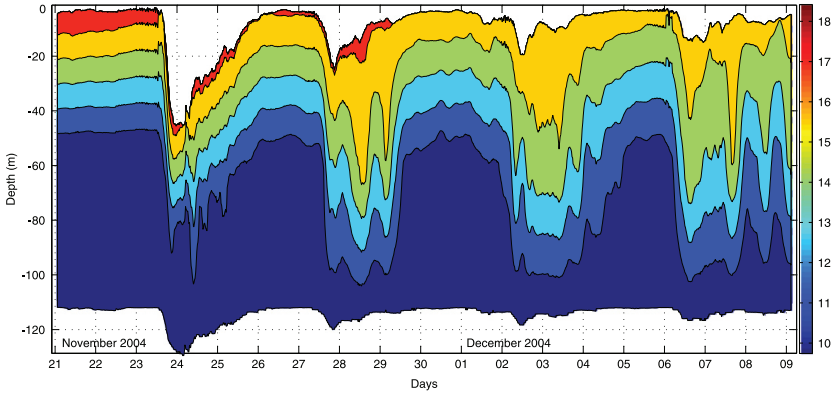

Fig. 3. Time series of isotherm fluctuations in the south-western part of the Caspian Sea.

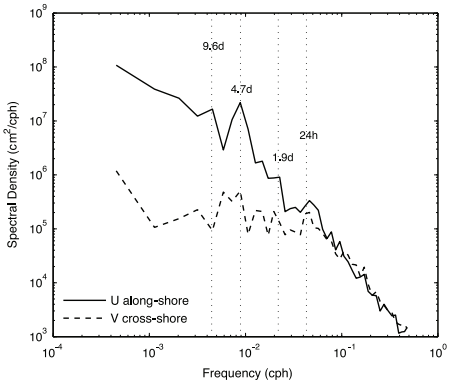

Fig. 4. Spectral density versus frequency in the thermocline depicted in Fig. 3.

usually resides in the first mode when the thermocline is sharp (for a discontinuous density distribution all the internal energy resides in the 1. mode, i.e. in the interfacial wave). In the southern Caspian Sea the summer/autumn thermocline is quite sharp, and we therefore choose to attribute the observations in Fig. 3 to the 1. baroclinic mode. If $T_1 = 4.7$ days, and typically $c_1 \sim 1\,\mathrm{m\,s^{-1}}$, the corresponding wavelength would be 406 km, which is within the lateral geometry of the Caspian Sea. Since this measurement site is positioned about 3 km off the shelf break (corresponding to our coast), and the typical 1. mode Rossby radius is 10 km, we find from (11) for the maximum amplitude $A_1 \sim 30 \times \exp(3/10)\,\mathrm{m} = 40\,\mathrm{m}$.

Taking $A_1 = 40\,\mathrm{m}$, $H_0 = 120\,\mathrm{m}$ and $c_1 = 1.21\,\mathrm{m\,s^{-1}}$, we find for the scaling factor (20): $u_0 = 0.07\,\mathrm{m\,s^{-1}}$. This implies that the dimensional drift current varies from $0.07\,\mathrm{m\,s^{-1}}$ at the surface to $-0.05\,\mathrm{m\,s^{-1}}$ at 90 m depth, which is quite a remarkable result.

The derivation of the Stokes drift presupposes that the linear wave field velocity is much larger than the Stokes drift velocity, i.e. $|\bar{u}_s| \ll |\tilde{u}|$. This means from (11) and (14) that

$$A_n \ll 2H_0. \tag{21}$$

For the first mode considered here ($A_1 = 40$ m), (21) is reasonably well fulfilled.

5. The mean vertically-averaged Eulerian current

Since the mean Lagrangian (particle) velocity generally can be written as a sum of the Stokes drift velocity $(\bar{u}_s, \bar{v}_s)$ and a mean Eulerian current $(\bar{u}_E, \bar{v}_E)$ [11], we have for the volume fluxes, defined by integration from the bottom to the undisturbed surface:

$$\begin{aligned} \bar{U}_L &= \bar{U}_E + \bar{U}_S \\ \bar{V}_L &= \bar{V}_E + \bar{V}_S. \end{aligned} \tag{22}$$

Since the Stokes flux components are identically zero for the present problem, e.g. (15), we have

$$\bar{U}_L = \bar{U}_E, \qquad \bar{V}_L = \bar{V}_E. \tag{23}$$

Hence, $(\bar{U}_E, \bar{V}_E)$ can be determined to second order in wave steepness from (5) and (6). Utilizing (23), and the fact that $\tilde{v} = 0$ for this problem, we find from (5) and (6) for the mean horizontal Eulerian fluxes (valid to second order in wave steepness):

$$\begin{aligned} \frac{\partial \bar{U}_E}{\partial t} - f\bar{V}_E &= -\frac{\partial \bar{P}}{\partial x} - \frac{\partial \bar{Q}}{\partial x} - \bar{\tau}^{(x)}, \\ \frac{\partial \bar{V}_E}{\partial t} + f\bar{U}_E &= -\frac{\partial \bar{P}}{\partial y} - \bar{\tau}^{(y)}, \end{aligned} \tag{24}$$

where $\bar{\tau}^{(x,y)} = \bar{\tau}_B^{(x,y)}/\rho_r$. Here we have defined the averaged integrated pressure $\bar{P}$ as

$$\bar{P} = \frac{1}{\rho_r}\overline{\int_{-H}^{\eta} p\,dz}. \tag{25}$$

Furthermore, we have a wave-forcing term $\bar{Q}$ defined by

$$\bar{Q} = \int_{-H}^{0} \overline{\tilde{u}^2}\,dz. \tag{26}$$

Inserting from (10), we obtain to the lowest order, using (A.4)

$$\bar{Q} = \frac{1}{4H}\sum_{n=1}^{\infty} c_n^2 A_n^2 \exp\left(-2\alpha_n x - 2\alpha_n^{-1} y\right). \tag{27}$$

By integrating the continuity equation $\nabla \cdot \vec{v} = 0$ in the vertical, we obtain the exact expression

$$\frac{\partial \eta}{\partial t} = -\frac{\partial}{\partial x}\int_{-H}^{\eta} u\,dz - \frac{\partial}{\partial y}\int_{-H}^{\eta} v\,dz = -\frac{\partial U_L}{\partial x} - \frac{\partial V_L}{\partial y}. \tag{28}$$

Please cite this article in press as: J.E.H. Weber, P. Ghaffari, Mass transport in internal coastal Kelvin waves, European Journal of Mechanics B/Fluids (2014), http://dx.doi.org/10.1016/j.euromechflu.2014.02.006

We seek steady solutions to the mean drift problem. Utilizing (23), (28) then reduces to

$$\frac{\partial \bar{U}_E}{\partial x} + \frac{\partial \bar{V}_E}{\partial y} = 0. \tag{29}$$

Since the mean motion in the direction normal to the wave propagation (the y-direction) is very small (to be verified *a posteriori*), we neglect the effect of friction $\left(\bar{\tau}^{(y)}\right)$ in this direction. Hence, in the y-direction, the integrated pressure gradient is in geostrophic balance with the Coriolis force. From the vorticity of the steady version of (24), we obtain by utilizing (29)

$$\frac{df}{dy}\bar{V}_E = \frac{\partial^2 \bar{Q}}{\partial x \partial y} + \frac{\partial \bar{\tau}^{(x)}}{\partial y}. \tag{30}$$

On an f-plane, we then obtain directly, when we take that the bottom stress vanishes as $y \to \infty$:

$$\bar{\tau}^{(x)} = -\frac{\partial \bar{Q}}{\partial x}. \tag{31}$$

Since $\partial \bar{Q}/\partial x$ is proportional to the spatial damping of the wave field, it constitutes a radiation stress [5]. Then (31) simply expresses a balance between the radiation stress from the wave field and the bottom stress on the mean Eulerian flow.

The mean bottom stress is generally a function of the mean Eulerian flow in the fluid. Since the motion near the bottom is turbulent, a quadric function of the vertically-averaged mean velocity is often assumed, i.e. $\bar{\tau}^{(x)} = c_D \bar{U}_E |\bar{U}_E|/H^2$, where c_D is a non-dimensional drag coefficient of order 10^{-3}. However, for small velocities, we can simplify and introduce a linear friction coefficient $R = c_D U_0/H^2$, where U_0/H is a typical bottom velocity [13]. With this simplification, we have that

$$\bar{\tau}^{(x)} = R\bar{U}_E. \tag{32}$$

Then, from (31):

$$\bar{U}_E = -\frac{1}{R}\frac{\partial \bar{Q}}{\partial x}. \tag{33}$$

Defining the vertically-averaged alongshore mean velocity

$$\bar{u}_E = \frac{\bar{U}_E}{H} = \sum_{n=1}^{\infty} u_{En}(y) \exp\left(-2\alpha_n x\right), \tag{34}$$

we find from (27) and (33) that

$$u_{En}(y) = \frac{1}{4H^2}\left(\frac{K_n}{R}\right) c_n A_n^2 \exp\left(-2a_n^{-1} y\right). \tag{35}$$

We note that the wave-induced mean Eulerian current for each mode is trapped to the coast within the internal Rossby radius, and that the current is always positive (directed along the waves). This is similar to the findings in [6] for interfacial coastal Kelvin waves. However, as shown in [4] and in this paper, the Stokes drift for the first baroclinic mode is different for the internal Kelvin waves with continuously varying N, and interfacial Kelvin waves where N is infinite at the transition between layers. For the two-layer case with a jump in density across the interface, the Stokes drift is positive in both layers, while for a continuous density variation it attains a negative value near the depth where the buoyancy frequency peaks. We note the important factor K_n/R, where K_n is given by (A.9). It expresses the relative importance between forcing from the wave field (through the radiation stress) versus the restraint of bottom friction on the mean flow. In balanced flow, K_n/R should be of order unity.

Defining the vertically-averaged off-shore mean velocity by

$$\bar{v}_E = \frac{\bar{V}_E}{H} = \sum_{n=1}^{\infty} v_{En}(y) \exp\left(-2\alpha_n x\right), \tag{36}$$

we now obtain from (29), using the boundary condition $\bar{V}_E = 0$, $y = 0$:

$$v_{En}(y) = \frac{1}{8H^2}\left[\frac{K_n^2}{fR}\right] c_n A_n^2 \left(1 - \exp\left(-2a_n^{-1} y\right)\right). \tag{37}$$

Since K_n is a small quantity, we note that $v_n \ll u_n$. This justifies our neglect of the turbulent bottom friction in the y-direction in (30).

6. Discussion and concluding remarks

The mean Lagrangian velocity is composed of a Stokes drift plus a mean Eulerian current. While the Stokes drift is inherent in the waves, and determined basically from the inviscid fluid motion, the mean wave-induced Eulerian flow is strongly dependent on the effect of friction. We note from (35) that it is directly proportional to K_n/R, where K_n is related to the spatial decay of the wave field, while R represents the effect of friction on the mean flow. In this way we see that it is the wave decay that drives the mean Eulerian flow (through the radiation stresses), while friction on the mean flow is needed to maintain balance.

In the present paper we have studied the drift due to internal coastal Kelvin waves. Both the Stokes drift and the mean Eulerian current are trapped to the coast within the Rossby radius of deformation. The present approach yields the Stokes drift as a function of depth, while the mean Eulerian current is determined as a depth average by integration from the bottom to the surface. This procedure masks the vertical variation of the Eulerian drift current, and makes comparisons with the Stokes drift at a certain depth difficult. For the first baroclinic Kelvin mode at the coast, we find from (20) and (35) that the ratio between the depth-averaged Eulerian current and the surface value of the Stokes drift becomes

$$\frac{u_{E1}}{u_{S1}} = \frac{H_0^2}{2H^2}\left[\frac{K_1}{R}\right]. \tag{38}$$

This shows that pycnocline position, total basin depth and friction all contribute to the relative strength of these currents.

We have applied our general results to the Caspian Sea, using a Brunt–Väisälä frequency distribution with depth which is typical for autumn/early winter conditions in the south-western part. Estimating the amplitude of the vertical thermocline displacement from observational data, we find Stokes drift velocities at the coast of order $0.07\,\mathrm{m\,s^{-1}}$ at the surface, and $-0.05\,\mathrm{m\,s^{-1}}$ just below the Brunt–Väisälä frequency maximum at 60 m. Obviously, from (38), the vertically-averaged Eulerian current are smaller than $0.07\,\mathrm{m\,s^{-1}}$. However, one interesting point here is that while the integrated Stokes drift (the Stokes flux) is zero; see (15), the Eulerian flux is not. For the first mode we find from (35) for the total volume flux q_1 in the trapped region

$$q_1 = \int_0^{\infty} \bar{U}_{E1} dy = \frac{c_1^2 A_1^2}{4Hf}\left[\frac{K_1}{R}\right]. \tag{39}$$

For the Caspian Sea with $f = 8.83 \times 10^{-5}\,\mathrm{s^{-1}}$, the Rossby radius for the first mode is $a_1 = c_1/f = 13.7\,\mathrm{km}$, so the transport in (39) occurs within a narrow region of width $a_1/2 = 6.9\,\mathrm{km}$. Since internal coastal Kelvin waves always propagate with the coast to the right in the northern hemisphere, we conclude that there is a systematic contribution from such waves to the mean circulation in the Caspian Sea.

Acknowledgments

We gratefully acknowledge financial support from the Research Council of Norway through the grants 196438 (BioWave) and 207541 (Oil Wave).

Please cite this article in press as: J.E.H. Weber, P. Ghaffari, Mass transport in internal coastal Kelvin waves, European Journal of Mechanics B/Fluids (2014), http://dx.doi.org/10.1016/j.euromechflu.2014.02.006

Appendix A. Linear internal coastal Kelvin waves

According to the adopted approach, we assume that

$$\tilde{u} = \sum_{n=1}^{\infty} u_n(x,y,z)\phi_n'(z),$$
$$\tilde{v} = 0,$$
$$\tilde{p} = \rho_r \sum_{n=1}^{\infty} p_n(x,y,z)\phi_n'(z), \tag{A.1}$$
$$\tilde{\xi} = \sum_{n=1}^{\infty} \xi_n(x,y,t)\phi_n(z),$$

where the primes denote differentiation with respect to z. Separation of variables requires that $p_n = c_n^2 \xi_n$, where c_n is the constant eigenvalue. The eigenfunctions ϕ_n are solutions of

$$\phi_n'' + \frac{N^2}{c_n^2}\phi_n = 0. \tag{A.2}$$

For the baroclinic modes we assume a rigid lid at the surface. Hence the boundary conditions become

$$\phi_n = 0, \qquad z = -H, 0. \tag{A.3}$$

It is easily shown that the eigenfunctions ϕ_n' constitute an orthogonal set for arbitrary $N = N(z)$. Assuming that ϕ_n is dimensionless, we can normalize ϕ_n' by assuming

$$\int_{-H}^{0} \left(\phi_n'\right)^2 dz = \frac{1}{2H}. \tag{A.4}$$

For $N = N(z)$ the eigenvalues and the eigenfunctions must be obtained numerically.

Utilizing the orthogonality property, the governing equations may be written

$$\frac{\partial u_n}{\partial t} = -c_n^2 \frac{\partial \xi_n}{\partial x} + \tau_n^{(x)},$$
$$fu_n = -c_n^2 \frac{\partial \xi_n}{\partial y}, \tag{A.5}$$
$$\frac{\partial \xi_n}{\partial t} = -\frac{\partial u_n}{\partial x},$$

where the baroclinic modes are given by $n = 1, 2, 3$, etc. Furthermore, we have defined

$$\tau_n^{(x)} = \frac{2H}{\rho_r}\int_{-H}^{0} \frac{\partial \tilde{\tau}^{(x)}}{\partial z}\phi_n' dz, \tag{A.6}$$

where $\tilde{\tau}^{(x)}$ is the turbulent stress on the wave motion in the x-direction. Since $\tilde{v} = 0$, we have taken $\tilde{\tau}^{(y)} = 0$. In the present problem we model the friction on internal Kelvin waves by a turbulent diffusion coefficient of momentum ν_T such that $\tilde{\tau}^{(x)} = \rho_r \nu_T \partial\tilde{u}/\partial z$. With $\tilde{u}$ given by the series expansions (8), this formulation cannot capture the effect of bottom stress, but works well for the viscous dissipation in the bulk of the fluid for the baroclinic modes. In this analysis we assume that $\nu_T N^2$ is independent of z; see e.g., [14]. More specifically, from Williams and Gibson [15], $\nu_T N^2 = C\varepsilon$, where C is a constant and ε the rate of dissipation of turbulent kinetic energy. Utilizing (A.1) and (A.4), (A.6) reduces to

$$\tau_n^{(x)} = -\frac{\nu_T N^2}{c_n^2} u_n. \tag{A.7}$$

The governing equations for mode n then become

$$\frac{\partial u_n}{\partial t} = -c_n^2 \frac{\partial \xi_n}{\partial x} - K_n u_n,$$
$$fu_n = -c_n^2 \frac{\partial \xi_n}{\partial y}, \tag{A.8}$$
$$\frac{\partial \xi_n}{\partial t} = -\frac{\partial u_n}{\partial x},$$

where

$$K_n = \frac{\nu_T N^2}{c_n^2}. \tag{A.9}$$

The trapping condition becomes

$$u_n, \xi_n \to 0, \qquad y \to \infty. \tag{A.10}$$

We consider spatially damped waves and take that

$$u_n, \xi_n = \left\{\hat{u}_n(y), \hat{\xi}_n(y)\right\} \exp(i(\kappa_n x - \omega t)), \tag{A.11}$$

where ω is a real positive frequency and κ_n the complex wave number for mode n. We define $\kappa_n = k_n + i\alpha_n$, where k_n is a real wave number and α_n the spatial decay rate. By eliminating u_n from (A.8), we obtain

$$\frac{\partial^2 \xi_n}{\partial t^2} - c_n^2 \frac{\partial^2 \xi_n}{\partial x^2} + K_n \frac{\partial \xi_n}{\partial t} = 0. \tag{A.12}$$

We assume solutions of the form

$$\xi_n = A_n G_n(y) \exp(i(\kappa_n x - \omega t)). \tag{A.13}$$

Inserting into (A.12), we obtain the dispersion relation

$$\omega^2 + iK_n\omega - c_n^2\kappa_n^2 = 0. \tag{A.14}$$

Assuming that $|\alpha_n|/k_n \ll 1$, the real and imaginary parts of (A.14) yield that

$$k_n = \pm\frac{\omega}{c_n}, \tag{A.15}$$
$$\alpha_n = \frac{k_n K_n}{2\omega}. \tag{A.16}$$

Finally, from the geostrophic balance in (A.8) we obtain

$$\frac{\partial \xi_n}{\partial y} + \frac{f}{\omega}(k_n - i\alpha_n)\,\xi_n = 0. \tag{A.17}$$

Inserting from (A.13), we find for the coastal Kelvin wave:

$$G_n(y) = \exp\left(-a_n^{-1} + il_n\right) y, \tag{A.18}$$

where

$$a_n = \frac{\omega}{k_n f}, \tag{A.19}$$
$$l_n = \frac{f\alpha_n}{\omega}. \tag{A.20}$$

Here a_n is the internal Rossby radius, and l_n the friction-induced wave number in the y-direction. We note that trapping requires that $k_n > 0$, i.e. we must choose the positive sign in (A.15), implying wave propagation with the coast to the right. Hence, $c_n = \omega/k_n > 0$.

References

[1] P. Ghaffari, H.A. Lahijani, J. Azizpour, Snapshot observation of the physical structure and stratification in deep-water of the south Caspian Sea (western part), Ocean Sci. 6 (2010) 877–885.

Please cite this article in press as: J.E.H. Weber, P. Ghaffari, Mass transport in internal coastal Kelvin waves, European Journal of Mechanics B/Fluids (2014), http://dx.doi.org/10.1016/j.euromechflu.2014.02.006

[2] J. McCreary, Eastern tropical ocean response to changing wind systems: with application to El Niño, J. Phys. Oceanogr. 6 (1976) 632–645.
[3] A.J. Busalacchi, J.J. O'Brien, The seasonal variability in a model of the tropical Pacific, J. Phys. Oceanogr. 10 (1980) 1929–1951.
[4] J.E.H. Weber, G. Broström, K.H. Christensen, Stokes drift in internal equatorial Kelvin waves; continuous stratification versus two-layer models, J. Phys. Oceanogr. 44 (2014) 591–599.
[5] M.S. Longuet-Higgins, R.W. Stewart, Changes in the form of short gravity waves on long waves and tidal currents, J. Fluid Mech. 8 (1960) 565–583.
[6] E. Stöylen, J.E.H. Weber, Mass transport induced by internal Kelvin waves beneath shore-fast ice, J. Geophys. Res. 115 (2010) C03022.
[7] M.J. Lighthill, Dynamic response of the Indian Ocean to onset of the southwest monsoon, Phil. Trans. R. Soc. Lond. A265 (1969) 45–92.
[8] A.E. Gill, A.J. Clarke, Wind-induced upwelling, coastal currents, and sea-level changes, Deep-Sea Res. 21 (1974) 325–345.
[9] E.A. Martinsen, J.E.H. Weber, Frictional influence on internal Kelvin waves, Tellus 33 (1981) 402–410.
[10] G.G. Stokes, On the theory of oscillatory waves, Trans. Camb. Phil. Soc. 8 (1847) 441–455.
[11] M.S. Longuet-Higgins, Mass transport in water waves, Phil. Trans. R. Soc. Lond. A245 (1953) 535–581.
[12] O.M. Phillips, The Dynamics of the Upper Ocean, Cambridge University Press, New York, 1966.
[13] E. Nöst, Calculating tidal current profiles from vertically integrated models near the critical latitude in the Barents Sea, J. Geophys. Res. 99 (1994) 7885–7901.
[14] J.E. Fjeldstad, Internal waves of tidal origin, in: Part I. Theory and analysis of observations, in: Geophysica Norwegica, No. 5, 1964, pp. 1–73. XXV.
[15] R.B. Williams, C.H. Gibson, Direct measurements of turbulence in the Pacific Equatorial Undercurrent, J. Phys. Oceanogr. 4 (1974) 104–108.

Please cite this article in press as: J.E.H. Weber, P. Ghaffari, Mass transport in internal coastal Kelvin waves, European Journal of Mechanics B/Fluids (2014), http://dx.doi.org/10.1016/j.euromechflu.2014.02.006